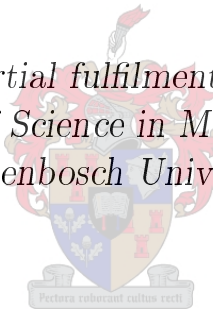


Investigation of the Heave, Sway and Roll Motions of Typical Ship Like Hull Sections Using RANS Numerical Methods

by

H.L. Henning

*Thesis presented in partial fulfilment of the requirements for
the degree of Master of Science in Mechanical Engineering at
Stellenbosch University*



Department of Mechanical and Mechatronic Engineering,
University of Stellenbosch,
Private Bag X1, Matieland 7602, South Africa.

Supervisors:

Prof. G.D. Thiart Prof. T.M. Harms

December 2011

Declaration

By submitting this thesis electronically, I declare that the entirety of the work contained therein is my own, original work, that I am the owner of the copyright thereof (unless to the extent explicitly otherwise stated) and that I have not previously in its entirety or in part submitted it for obtaining any qualification.

Signature:
H.L. Henning

Date: 2011/08/28

Copyright © 2011 Stellenbosch University
All rights reserved.

Abstract

Investigation of the Heave, Sway and Roll Motions of Typical Ship Like Hull Sections Using RANS Numerical Methods

H.L. Henning

*Department of Mechanical and Mechatronic Engineering,
University of Stellenbosch,
Private Bag X1, Matieland 7602, South Africa.*

Thesis: MScEng (Mech)

December 2011

The hydrodynamic characteristics of three typical ship-like hull sections, in different motions, are numerically investigated using FLUENT, 2009. These simple shapes, namely a v-bottom (triangle) hull, a flat-bottom (square) hull and a round-bottom (semi-circle) hull, are investigated in uncoupled heave, sway and roll. The problem is described in two dimensions. A combination of numerical methods and models, found in literature, are used to conduct this investigation. Hull characterisation is achieved through the use of hull mass and damping coefficients. These numerically determined coefficients are compared to experimental work conducted by Vugts (1968). A good correlation between the numerical and experimental results exists for the heave and sway cases. By normalising the coefficients, different hulls are comparable to one another. The numerical models used are validated and verified. Roll motion remains largely unsolved for very large angles of roll (in excess of 11°). Different fluid flow phenomena occurring around the hull sections have varying degrees of influence on the motions of a hull. It is found that not one of the turbulence models investigated can be employed to globally solve each type of hull-motion case. Also, forced oscillations in computational simulations require considerably more computational time than free-decay oscillating hull simulations.

Uittreksel

Onderzoek in die Opwieg, Dwarswieg en Rol Bewegings van Tipiese Skeepsromp Vorms deur die Gebruik van RGNS Numeriese Metodes

H.L. Henning

*Departement Meganiese en Megatroniese Ingenieurswese,
Universiteit van Stellenbosch,
Privaatsak X1, Matieland 7602, Suid Afrika.*

Tesis: MScIng (Meg)

Desember 2011

Die hidrodinamiese karakteristieke van verskillende skeepsrompvorms, in verskeie bewegingswies, is numeries ondersoek met behulp van FLUENT, 2009. Drie eenvoudige vorms ('n v-bodem (driehoek), plat-bodem (reghoek) en rondobodem (semi-sirkel) romp) is onderskeidelik ondersoek in opwieg, dwarswieg en rol. Die probleem is twee-dimensioneel. Daar is gebruik gemaak van 'n kombinasie van numeriese metodes en modelle, uit die literatuur, om die ondersoek uit te voer. Die rompe is gekarakteriseer met behulp van massa- en dempingskoëffisiënte. Hierdie numeries bepaalde koëffisiënte is vergelyk met die eksperimentele werk van Vugts (1968). Daar bestaan 'n goeie korrelasie tussen die numeriese en eksperimentele resultate vir die opwieg en dwarswieg gevalle. Die koëffisiënte is genormaliseer om die verskeie rompvorms te vergelyk. Die numeriese modelle is geverifieer en valideer. Rolbewegings is onopgelos vir groot rolhoeke (groter as 11°). Die mate waartoe die romp se beweging beïnvloed word deur die verskillende vloeïverskynsels wat om die rompe ontstaan, verskil. Daar is bevind dat geen van die turbulensie modelle gebruik kan word om alle skeepsbeweging-gevalle op te los nie. Gedwonge-ossilasie numeriese simulaties benodig meer berekeningstyd as vrye-verval ossilasie gevalle.

Acknowledgements

I would like to acknowledge and express my sincere gratitude to my Lord and Saviour (and strength) Jesus Christ (Romans 8:31).

To my dear parents (Jan and Estelle Henning) for their amazing continuous physical and emotional support, for all their love, and for laying a solid foundation for my life.

To Professor Gerrie Thiart for his guidance and for affording me the opportunity to peruse my dreams through further studying. I will miss him dearly.

To Professor Thomas Harms for his excellent guidance, for making so much of his precious time available, and for the relationship we have developed. I will be ever grateful for the wonderful opportunities that he gave me and for many very insightful conversations (also often on the humorous side).

To Professor Volker Bertram for the very helpful correspondence.

To Project Fluxion and the CSIR for the funding of this project.

To Qfinsoft and ANSYS for the provision of academic software licences and support.

To all my friends and family (special mention to my brother Jan-Herndrik Henning and to Kendra Smith) for all their love and support in my mission. God bless you.

Dedications

Aan my liewe familie en vriende.

Contents

Declaration	i
Abstract	ii
Uittreksel	iii
Acknowledgements	iv
Dedications	v
Contents	vi
List of Figures	x
List of Tables	xiv
Nomenclature	xvi
1 Introduction	1
1.1 Background	1
1.2 Basic Ship Theory	2
1.2.1 Definitions of motions	3
1.2.2 Mass forces	3
1.2.3 Damping forces	5
1.2.4 Restoring forces	6
1.2.5 External forces	6
1.3 Literature Review	6
1.4 Fundamental Equations of Motion	10
1.5 Broad Objectives	11
1.6 Specific Objectives	11
1.6.1 Numerical characterisation and model evaluation	12
1.6.2 Presence and effects of fluid phenomena	12
1.6.3 Prescribed displacement	12
1.7 Project Scope	12

2	Computational Approach	14
2.1	Computational and Fluid Theory	14
2.2	Turbulence Models in Literature	15
2.3	Turbulence Models Theory	17
2.4	Turbulence Model Employed	20
2.5	Numerical Methods and Models	20
2.6	Discretization Schemes	24
3	Numerical Solver Settings	26
3.1	Model and Material Settings	26
3.2	Boundary Conditions	27
3.2.1	Boundary conditions in literature	27
3.2.2	Boundary conditions implemented	28
3.3	Dynamic Mesh	35
3.4	Solution Settings	35
3.4.1	Reference values	35
3.4.2	Pressure velocity coupling	35
3.4.3	Spatial and temporal discretization	36
3.4.4	Solution controls	36
3.4.5	Solution initialisation	37
3.4.6	Monitors and calculations	37
3.4.7	Time step	39
4	Computational Mesh	42
4.1	Meshes Used in Literature	43
4.2	Mesh Requirements	45
4.2.1	Introduction	45
4.2.2	Close wall grid fineness	46
4.2.3	Close wall grid thickness	49
4.2.4	Fluid interface	50
4.2.5	Boundary	51
4.2.6	Dynamic mesh region	51
4.2.7	Inner mesh region	52
4.2.8	Far field	53
4.3	Mesh Specifications	53
5	Verification And Validation	56
5.1	Validation: Grid Independence Study	56
5.1.1	Introduction	56
5.1.2	Discussion	57
5.1.3	Conclusion	58
5.2	Validation: y^+ Values	59
5.3	Verification: Turbulence Models	61

6	Results	64
6.1	Computational Simulation Results	64
6.1.1	y^+ values	68
6.2	Data Analysis	70
6.2.1	MATLAB (2005)	70
6.3	Results and Discussion	72
6.3.1	Introduction	72
6.3.2	V-bottom hull heave	73
6.3.3	Flat-bottom hull heave	75
6.3.4	Round-bottom hull heave	76
6.3.5	V-bottom hull sway	78
6.3.6	Flat-bottom hull sway	78
6.3.7	Round-bottom hull sway	80
6.3.8	V-bottom hull roll	82
6.3.9	Flat-bottom hull roll	84
6.3.10	Round-bottom hull roll	85
6.4	Conclusion	88
7	Conclusion And Recommendations	89
7.1	Summary	89
7.2	Numerical Characterisation and Model Evaluation	89
7.3	Presence and Effects of Fluid Phenomena	90
7.4	Prescribed Displacement	90
7.5	Future Work	91
	Appendices	92
A	Additional Numerical Set-Up Calculations	93
A.1	Numerical Model Calculations	93
A.1.1	Boundary Condition Constants and Calculations	93
A.1.2	Time Step Calculations	93
A.2	y^+ Calculations	94
A.2.1	Falkner-Skan Calculations	95
B	Additional Results	97
B.1	Additional y^+ Value Verification	97
B.2	Additional Amplitude Plots	102
C	Additional Tables	108
C.1	Transition SST constants	108
C.2	y^+ Monitor Values for Hull Surfaces	108
C.3	Amplitude and Phase Angle Errors	113
D	Additional Grid Seeding Figures and Tables	116
D.1	Seeding of Domain Edges	116

<i>CONTENTS</i>	ix
D.2 Domain Edge Seeding Details	120
E FLUENT (2009) Dynamic Mesh Definitions	125
E.1 Dynamic Mesh Definitions	125
References	128

List of Figures

1.1	Schematic of a body representing a hull with the conventional ordinate system used	4
1.2	Schematic of the cross-sections numerically and experimentally tested	5
3.1	Diagram (not to scale) of the computational domain and wall boundary conditions	30
3.2	Diagram (not to scale) of the computational domain and porous boundary conditions	32
3.3	Schematic (not to scale) of the computational domain and open channel pressure outlet boundary conditions	33
3.4	Total vertical force measured on a heaving v-bottom hull for various different domain sizes with open channel pressure outlet boundary conditions	34
3.5	Percentage change of the amplitudes and phase angles from one computational domain to the next	35
3.6	Last 60 iterations for a rolling flat-bottom hull, with the SST transition turbulence model	38
4.1	Schematic (scale: 1:66.67) of the computational domain	42
4.2	Schematic (scale: 1:64.22) of the computational domain block zones	44
4.3	Schematic (not to scale) of the expected flow near the boundary wall (hull)	45
4.4	Schematic (scale: 1:8.89) of the boundary layer grid	47
4.5	Schematic (scale: 1:67.96) of the fluid interface grid zone (and close-up of grid details)	52
4.6	Contours of density (kg/m^3) of the fluid interface grid zone (same close-up as in figure 4.5) (scale: 1:7.5)	53
4.7	Close up of the grid regions around the hull (scale: 1:13.16)	54
4.8	Close up of the boundary grid zone (scale: 1:74.47)	55
5.1	Amplitude errors for each hull shape in heave for the highest oscillation frequency	58
5.2	Amplitude errors for each hull shape in sway for the highest oscillation frequency	59

5.3	Amplitude errors for each hull shape in roll for the highest oscillation frequency	60
5.4	Schematic (not to scale) of the flat-bottom hull and eight y^+ measuring points	61
5.5	Schematic (not to scale) of the flat-bottom hull and eight y^+ measuring points	62
5.6	Hydrodynamic mass coefficient for a flat-bottom hull oscillating at 4.917 rad/s in roll	63
5.7	Damping coefficient for a flat-bottom hull oscillating at 4.917 rad/s in roll	63
6.1	Total vertical force experienced by v-bottom hull oscillating at 6.811 rad/s in heave	65
6.2	Total horizontal force experienced by v-bottom hull oscillating at 6.811 rad/s in sway	66
6.3	Total moment experienced by v-bottom hull oscillating at 6.811 rad/s in roll	67
6.4	Number of oscillations required for a periodic force and moment curves, along with computational time required with normalised y-axis values	68
6.5	Hull surfaces divided into sub-surfaces for monitoring purposes (not to scale)	69
6.6	Mass and damping coefficients of a v-bottom hull in heave versus oscillation frequency presented by Vugts (1968) and the numerical coefficients obtained with CFD (FLUENT, 2009)	74
6.7	Mass and damping coefficients of a flat-bottom hull in heave versus oscillation frequency presented by Vugts (1968) and the numerical coefficients obtained with CFD (FLUENT, 2009)	75
6.8	Mass and damping coefficients of a round-bottom hull in heave versus oscillation frequency presented by Vugts (1968) and the numerical coefficients obtained with CFD (FLUENT, 2009)	77
6.9	Mass and damping coefficients of a v-bottom hull in sway versus oscillation frequency presented by Vugts (1968) and the numerical coefficients obtained with CFD (FLUENT, 2009)	79
6.10	Mass and damping coefficients of a flat-bottom hull in sway versus oscillation frequency presented by Vugts (1968) and the numerical coefficients obtained with CFD (FLUENT, 2009)	80
6.11	Mass and damping coefficients of a round-bottom hull in sway versus oscillation frequency presented by Vugts (1968) and the numerical coefficients obtained with CFD (FLUENT, 2009)	81
6.12	Mass moment and damping coefficients of a v-bottom hull in roll versus oscillation frequency presented by Vugts (1968) and the numerical coefficients obtained with CFD (FLUENT, 2009)	83

6.13	Mass moment and damping coefficients of a flat-bottom hull in roll versus oscillation frequency presented by Vugts (1968) and the numerical coefficients obtained with CFD (FLUENT, 2009)	86
6.14	Mass moment and damping coefficients of a round-bottom hull in roll versus oscillation frequency presented by Vugts (1968) and the numerical coefficients obtained with CFD (FLUENT, 2009)	87
B.1	y^+ values of the hull at time step $t = 25.411378$ s along A: the starboard side surface B: the bottom side surface	97
B.2	y^+ values of the hull at time step $t = 25.571199$ s along A: the starboard side surface B: the bottom side surface. $-y^+$ values of the hull at time step $t = 25.73102$ s along C: the starboard side surface D: the bottom side surface	98
B.3	y^+ values of the hull at time step $t = 25.890841$ s along C: the starboard side surface D: the bottom side surface. $-y^+$ values of the hull at time step $t = 26.050659$ s along A: the starboard side surface B: the bottom side surface	99
B.4	y^+ values of the hull at time step $t = 26.21048$ s along C: the starboard side surface D: the bottom side surface. $-y^+$ values of the hull at time step $t = 26.3703$ s along A: the starboard side surface B: the bottom side surface	100
B.5	y^+ values of the hull at time step $t = 26.530121$ s along C: the starboard side surface D: the bottom side surface. $-y^+$ values of the hull at time step $t = 26.689939$ s along A: the starboard side surface B: the bottom side surface	101
B.6	Force amplitude of a v-bottom hull in heave versus oscillation frequency presented by Vugts (1968) and force amplitude obtained with CFD (FLUENT, 2009)	102
B.7	Force amplitude of a flat-bottom hull in heave versus oscillation frequency presented by Vugts (1968) and force amplitude obtained with CFD (FLUENT, 2009)	103
B.8	Force amplitude of a round-bottom hull in heave versus oscillation frequency presented by Vugts (1968) and force amplitude obtained with CFD (FLUENT, 2009)	103
B.9	Force amplitude of a v-bottom hull in sway versus oscillation frequency presented by Vugts (1968) and force amplitude obtained with CFD (FLUENT, 2009)	104
B.10	Force amplitude of a flat-bottom hull in sway versus oscillation frequency presented by Vugts (1968) and force amplitude obtained with CFD (FLUENT, 2009)	104
B.11	Force amplitude of a round-bottom hull in sway versus oscillation frequency presented by Vugts (1968) and force amplitude obtained with CFD (FLUENT, 2009)	105

B.12	Moment amplitude of a v-bottom hull in roll versus oscillation frequency presented by Vugts (1968) and moment amplitude obtained with CFD (FLUENT, 2009)	105
B.13	Moment amplitude of a flat-bottom hull in roll versus oscillation frequency presented by Vugts (1968) and moment amplitude obtained with CFD (FLUENT, 2009)	106
B.14	Moment amplitude of a round-bottom hull in roll versus oscillation frequency presented by Vugts (1968) and moment amplitude obtained with CFD (FLUENT, 2009)	106
B.15	y^+ values at 8 different points 0.03 mm from the hull surface	107
D.1	Schematic (not to scale) of the computational domain v-bottom heave case numbered edges used for grid seeding (table D.1)	116
D.2	Schematic(not to scale) of the computational domain flat- and round-bottom heave case regions adapted from figure D.1, with numbered edges used for grid seeding (tables D.2 and D.3)	117
D.3	Schematic (not to scale) of the computational domain v-bottom sway case numbered edges used for grid seeding (table D.4)	117
D.4	Schematic (not to scale) of the computational domain flat- and round-bottom sway case regions adapted from figure D.3, with numbered edges used for grid seeding (tables D.5 and D.6)	118
D.5	Schematic (not to scale) of the computational domain v-bottom roll case numbered edges used for grid seeding (table D.7)	118
D.6	Schematic (not to scale) of the computational domain flat- and round-bottom roll case regions adapted from figure D.5, with numbered edges used for grid seeding (tables D.8 and D.9)	119
E.1	Schematic of the concept of interconnecting springs between cell nodes	126

List of Tables

3.1	Properties of the fluids considered	27
3.2	Prescribed motions of the hulls	30
3.3	Distances of the open channel pressure outlet boundary conditions from the oscillating hull	33
3.4	Simulation oscillation frequencies and time steps	41
4.1	Instability and separation conditions	46
4.2	$Re_{\delta^{**}}$ numbers for transition	48
4.3	$Re_{v, max}$ numbers for instability and transition	48
4.4	Distance y of the first grid node from the hull surface, required to capture instability and transition	49
4.5	Momentum thickness Reynolds number ($Re_{\delta^{**}}$) and corresponding boundary layer thickness (δ) for instability and transition	50
4.6	Properties of the boundary layer grid at the surface of the hulls	50
4.7	Boundary layer grids assigned to different simulated cases	51
4.8	Mesh specifications	54
6.1	Data extraction of uncoupled motions	70
7.1	Numerical models recommended for hull characterisation	91
C.1	Transition SST model constants	108
C.2	y^+ monitor values for hull sides in heave	109
C.3	y^+ monitor values for hull sides in sway	110
C.4	y^+ monitor values for hull sides in roll	111
C.5	y^+ monitor values for hull sides with medium displacement in sway	112
C.6	Errors determined for each computational mesh fineness for the heave cases	113
C.7	Errors determined for each computational mesh fineness for the sway cases	114
C.8	Errors determined for each computational mesh fineness for the roll cases	115
D.1	V-bottom heave mesh seeding summary	120
D.2	Flat-bottom heave mesh seeding summary	121

D.3	Round-bottom heave mesh seeding summary	122
D.4	V-bottom sway mesh seeding summary	122
D.5	Flat-bottom sway mesh seeding summary	123
D.6	Round-bottom sway mesh seeding summary	123
D.7	V-bottom roll mesh seeding summary	123
D.8	Flat-bottom roll mesh seeding summary	123
D.9	Round-bottom roll mesh seeding summary	124

Nomenclature

Constants

C_μ	Empirical constant for turbulent viscosity calculations [0.09] []
g	Gravitational acceleration [-9.81] [m/s ²]
μ	Water dynamic viscosity [1.002×10^{-3}] [N.s/m ²]
ν	Water kinematic viscosity [1.004×10^{-6}] [m ² /s]
π	Archimedes' Constant [3.141 592 654] []
ρ	Water density [998.207] [kg/m ³]

Variables

A	Area [m ²]
A	Force amplitude [N]
A	Moment amplitude [N.m]
a_i	Cell centre coefficient []
a_{ii}^*	Normalised hydrodynamic mass coefficient of a hull in heave or sway [m/kg]
a_k	Fourier series coefficient []
a_{nb}	Influence coefficients for neighbouring cells []
$a_{zz,yy,\phi\phi}$	Hydrodynamic mass or mass moment of inertia coefficient of a hull in heave, sway and roll, respectively []
$a_{\phi\phi}^*$	Normalised mass moment of inertia coefficient of a hull in roll [kg/m]
\vec{a}	Position vector of any point on the free-surface [m]
\vec{a}	Direction vector [m]
B	Breadth of a section at the waterline [m]
b	Constant part of term source []
b_{ii}^*	Normalised damping coefficient of a hull in heave or sway [m.s/kg]
b_k	Fourier series coefficient []
$b_{zz,yy,\phi\phi}$	Damping coefficient against motion of a hull in heave, sway and roll, respectively []
$b_{\phi\phi}^*$	Normalised damping coefficient of a hull in roll [s/(kg.m ²)]

\vec{b}	Position vector of the centroid of a face of a cell	[m]
C	Variable reserved for constant values	[]
$c_{zz,\phi\phi}$	restoring coefficient of a hull in heave and roll, respectively []	[]
$E_{U,i}$	Error value of the force amplitude for mesh number i . . .	[N]
$E_{U,i}$	Error value of the moment amplitude for mesh number i [N.m]	[N.m]
F	A function	[]
F	Force	[N]
F_r	Froude number	[]
f_i	Value of data point at i	[]
f_{lin}	Value of the linearised data point at i	[]
$f(t)$	Fourier series of a function	[]
$H(\lambda)$	Shape factor	[]
I	Turbulence intensity (as a fraction)	[]
K	Moment experienced by the hull	[N.m]
K_{osc}	Moment amplitude experienced by the hull	[N.m]
k	Turbulence kinetic energy per unit mass	[m ² /s ²]
k	Spring stiffness	[N/m]
k	Order of Fourier series	[]
L	Hydraulic diameter of an open channel	[L]
l	A length scale	[m]
M	Moment	[N.m]
m	Mass	[kg]
m	Iteration number	[]
\dot{m}_{pq}	Mass transfer rate from phase q to p per unit volume . . .	[kg/(m ³ .s)]
\dot{m}_{qp}	Mass transfer rate from phase p to q per unit volume . . .	[kg/(m ³ .s)]
N	Total number of the considered subjects	[]
n	Current number of considered subject	[]
n	Number of cells	[]
n	Number of nodes	[]
n	Number of iterations	[]
\tilde{P}	Favré-averaged pressure	[Pa]
p	Pressure	[Pa]
p	Order of discretization equations	[]
\tilde{p}	Accurate prediction of order of discretization equations . .	[]
p^*	Guessed pressure value	[Pa]
p'	Correction pressure value	[Pa]

p_0	Total pressure	[Pa]
R^ϕ	Scaled residual	[]
Re	Reynolds number	[]
Re_v	Vorticity Reynolds number	[]
Re_x	Reynolds number a distance x from the leading edge	[]
Re_{θ_r}	Momentum thickness Reynolds number	[]
r	Translational displacement	[m]
r	Mesh refinement ratio	[]
\vec{r}	Moment lever-arm vector	[m]
S	Source term	[kg/(m ² s ²)]
T	Period	[s]
T_u	Free-stream turbulence	[%]
t	Time	[s]
U	Velocity scale	[m/s]
U	Free-stream velocity	[m/s]
U	Measured physical quantity	[]
U_e	Free-stream fluid velocity for plate flows	[m/s]
\tilde{U}	Farve-averaged velocity in the direction of the x-axis	[m/s]
u	Velocity in the direction of the x-axis	[m/s]
u'	Fluctuating velocity in the direction of the x-axis	[m/s]
u_τ	Friction velocity	[m/s]
V	Volume	[m ³]
$V_{cell,min}$	Minimum cell volume	[m ³]
\tilde{V}	Farve-averaged velocity in the direction of the y-axis	[m/s]
v	Velocity in the direction of the y-axis	[m/s]
v	Velocity magnitude	[m/s]
v'	Fluctuating velocity in the direction of the y-axis	[m/s]
\mathbf{v}	Volume	[m ³]
\tilde{W}	Farve-averaged velocity in the direction of the z-axis	[m/s]
w	Velocity in the direction of the z-axis	[m/s]
w'	Fluctuating velocity in the direction of the z-axis	[m/s]
x	A length in the direction of the x-axis	[m]
x	Coordinate	[m]
Y	Horizontal force experienced by the hull	[N]
Y_{osc}	Horizontal force amplitude experienced by the hull	[N]
y	A length in the direction of the y-axis	[m]

y	Depth of water	[m]
y	Perpendicular distance from a wall boundary	[m]
y_a	Hull displacement amplitude	[m]
Z	Vertical force experienced by the hull	[N]
Z_{osc}	Vertical force amplitude experienced by the hull	[N]
z	A length in the direction of the z-axis	[m]
z_a	Hull displacement amplitude	[m]
α_p	Pressure under-relaxation factor	[]
α_q	Volume fraction of fluid q	[]
α_u	Velocity u under-relaxation factor	[]
α_v	Velocity v under-relaxation factor	[]
β	Boundary node relaxation	[]
γ	Intermittency	[]
δ	Boundary layer displacement	[m]
δx	Displacement in the direction of x	[m]
δ^{**}	Boundary layer momentum thickness	[m]
ε	Turbulence viscosity dissipation rate	[m ² /s ³]
$\varepsilon_{Z,Y,K}$	Phase angles for heave, sway and roll respectively	[rad]
λ	Thwaites' momentum integral relation	[]
μ_t	Turbulence viscosity	[N.s/m ²]
$\tilde{\nu}$	Modified turbulence kinematic viscosity	[m ² /s]
ρ_q	Density of substance q	[kg/m ³]
ρ_{mix}	Density of the mixture of two fluids in a cell	[kg/m ³]
σ	Standard deviation	[]
τ	Shear stress	[N/m ²]
τ	Wall shear stress	[N/m ²]
ϕ	A fluid flow property variable	[]
ϕ_a	Hull angular displacement amplitude	[rad]
ω	Hull oscillation frequency	[rad/s]
ω	Turbulence specific dissipation rate	[s ⁻¹]

Chapter 1

Introduction

1.1 Background

The accurate prediction of the motion of a ship is desirable both when designing a new hull and when evaluating existing hulls. For displacement monohulls, it is possible to predict pitch, heave, sway and yaw remarkably accurately without the need to carry out experiments (Himento, 1981). In most large vessels, these motions are not sensitive to the effects of fluid viscosity. Out of the six motions of a ship (pitch, yaw, roll, sway, heave and surge), roll is the most difficult to determine but is also the most important, with regard to the prevention of events that may lead to capsizing (such as large masses of cargo shifting, green water, structural damage, etc.). The reason for its complexity is because of the non-linear nature of roll, and also because of the difficulty in determining the roll damping characteristics. It is known that large-amplitude ship motions result in highly non-linear or even chaotic behaviour (Mulk and Falzarano, 1994). The following consequences may occur as a result of unfavourable ship roll motions:

- Passenger and crew discomfort, including seasickness
- Shifting of non-cohesive or poorly fastened cargo and equipment
- Green water (water on the deck of a ship)
- Impairment of platform function (in the case of equipment support, or in naval applications, gunnery accuracy and aircraft operations may be jeopardised)
- Ship support to other vessels may be ineffective
- Disturbance to the ship's plant as a result of dynamic loading
- Decrease in forward speed and manoeuvrability
- Capsizing from excessive rolling

There are effectively three types of forces affecting the roll of a ship: inertial forces, restoring forces and damping forces. It is well known that inertial

forces are directly proportional to the moment of inertia of the hull under consideration, as well as an added inertia term due to the fluid surrounding the hull.

Unique hull-form vessels in commercial and military applications have broadened the need for robust mathematical approaches to studying the dynamics of these innovative ships (Ibrahim and Grace, 2009). The prediction of ship stability during the early stages of design is very important from the point of view of a vessel's safety. When the characteristics of a hull are to be determined, scaled models are constructed and numerous and various experiments are carried out on these replica hulls. Successful as this may be, it is generally a time-consuming and costly exercise.

In the past 20 years a larger emphasis has been placed on numerical models and simulations, especially computational fluid dynamics (CFD). Eulerian equations of motion were considered by Mulk and Falzarano (1994) and others before the advent of greater computing power. The initial use of Reynolds-averaged Navier-Stokes (RANS) methods to evaluate the properties of an oscillating body, incorporated potential flow methods (Korpus and Falzarano, 1997). Pure RANS numerical modelling of ship motions, along with free-surface effects, seems only to have been considered in the last decade. Wilson *et al.* (2006), Chen *et al.* (2000) and Sarkar and Vassalos (2000) carried out numerical investigations of specific hulls based on RANS methods with free-surface effects. Ibrahim and Grace (2009) considered the derivation of the equations of motion based on physical grounds; numerous methods of damping prediction are presented by them.

The main dilemma in characterising a specific hull section is the time and effort required to model the hull both numerically and experimentally. New hulls are rarely designed entirely from scratch, but are usually modifications or adaptations of existing hulls. Even though RANS methods applied in previous studies proved to be successful, no standardised comparisons have been made with regard to differences between typical smooth hull sections. Studies were generally carried out on single hull forms.

This project is proposed in order to produce results that facilitate the comparison between different typical hull sections. Numerical modelling may over time become the preferred method of carrying out ship motion analyses on current and future vessels. As these numerical models become more reliable and applicable, the need for implementation of experiments may be reduced in terms of both cost and frequency.

1.2 Basic Ship Theory

Ship hydrodynamics is a branch of naval architecture that includes the study of ship motions. This topic combines fluid dynamics and dynamics of a body to determine the hydrodynamic characteristics of hull sections. The state of

the fluid in which the hull is also plays a role in how a hull will behave, for example calm water versus a rough sea.

1.2.1 Definitions of motions

A hull in a body of water has six degrees of freedom, as defined in a conventional orthogonal axis system (figure 1.1) used in naval architecture (Brian, 2003). Translations are defined as surge, sway and heave along the x, y and z axes respectively. Rotations are defined as roll, pitch and yaw about the x, y, and z axes respectively (for convenience, the axis origin may be defined as the intersection of the longitudinal centre of flotation, water line and centre line).

This study is concerned with the heave, sway and roll motions of vessels. Motions accompanying roll of ships (such as pitch and heave) are negligibly small Korvin-Kroukovsky (1961). By convention, the initial still free water surface or water line (WL) is used to fix the roll axis for a hull in pure roll. It is often very convenient to define the roll axis as an axis that intersects the centre of gravity (CoG) of a hull. In this study the roll axis, CoG and WL coincide as shown in figure 1.2.

The roll motion of a ship in calm water (calm free-surface) occurs when a vessel is released from an initial angular displacement. Mono-hull displacement craft motions in quiet water are rare in practice, however, the characteristics of a vessel in quite water may provide insight into the motions of a vessel in rough sea ways.

1.2.2 Mass forces

The fundamental equation of motion of a rigid body is employed to describe the motion of a rolling vessel (see section 1.4). The mass term consists of the mass of the vessel plus a hydrodynamic (added) mass (mass moment of inertia in roll) of the vessel. The sum of these two is the virtual mass or virtual moment of inertia of the vessel. Added mass originates from a rigid body of arbitrary shape, rotating with variable angular velocity through an ideal, incompressible fluid of infinite extent. The physical reason for this phenomenon is still unclear and debated, it is often described as fluid entrained by the hull.

Numerous individual methods of calculating hydrodynamic mass exist. Ignoring viscous, frictional and wave forces (because an absence of a free-surface is assumed), reactive forces still arise within the fluid as a result of the variable velocity of the motion (Blagoveshchensky, 1962). The theoretical determination of the added mass of inertia is complicated. Coefficients of added mass are implemented to simplify calculations. Derivations of the moments of added mass were described by Blagoveshchensky (1962).

Practical methods for the approximate calculation of the added masses for a vessel do exist. The added mass is often obtained through experiments with

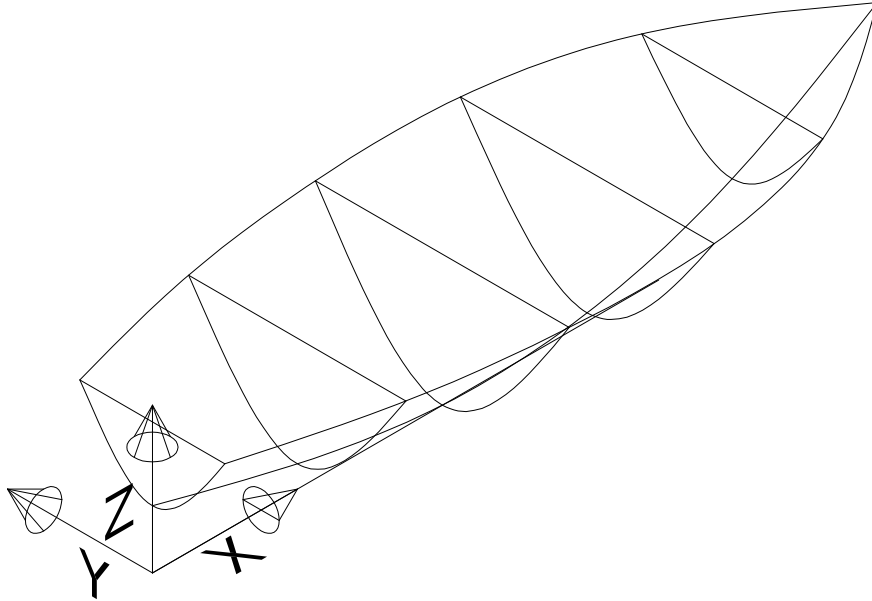


Figure 1.1: Schematic of a body representing a hull with the conventional ordinate system used

ship models. The added mass can often comprise of between 10 % to 30 % of the total mass of a vessel (Blagoveshchensky, 1962).

An oscillating vessel will experience resistance because of the surrounding fluid. Three major factors of the fluid resisting the motion of a hull are:

- The presence of viscous frictional forces between the wetted surface and the surrounding fluid
- The generation of waves
- The formation of vortices

These factors or flow phenomena (except for waves) arise because of the existence of fluid viscosity. Frictional forces are tangential to the hull surface. Waves and vortices are manifested as pressure forces (i.e. normal to the hull surface, often simply known as form drag). Vortices also increase hull friction because of the increase in fluid velocities. Each component has a different influence under different conditions and is not directly related to each other. Frictional forces are often found to be negligible in most cases for displacement hulls. Frictional forces do, however, need to be taken into consideration for scaled model experiments of rolling vessels. In the case of a body of revolution the rolling resistance is purely frictional (vortices and waves generated are negligible). In reality, the instantaneous roll axis moves about in space, therefore wave resistance is always present. Wave influence increases the further a hull deviates from a body of revolution. Resistance is also influenced by the shape of the bilge geometry of a hull.

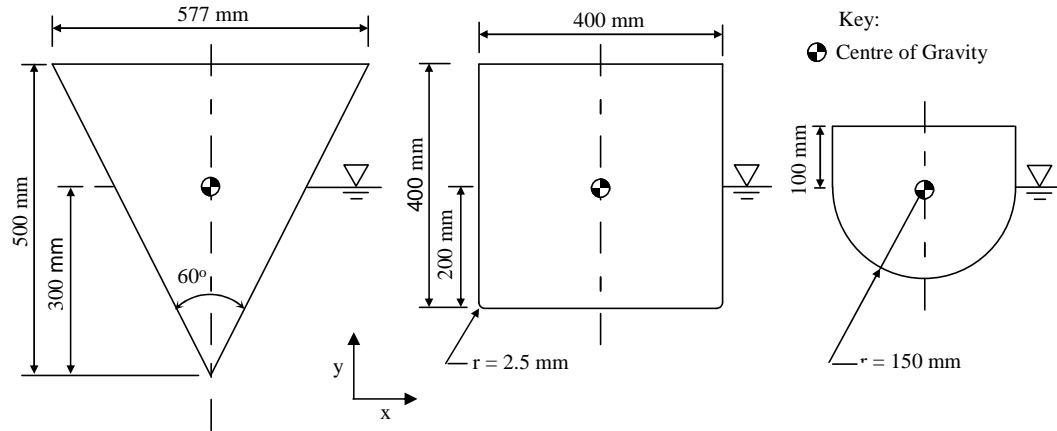


Figure 1.2: Schematic of the cross-sections numerically and experimentally tested

1.2.3 Damping forces

Resistance influencing factors may be represented as functions of velocity (angular velocity of the hull for roll and translational velocity for heave and sway) of the motions. For small motions, frictional forces and wave resistance are linear functions of velocity. Wave generation depends on (and is thus also a function of) the dimensions, shape and frequency of the oscillations of a vessel. Vortical resistance appears to be proportional to the second power of the velocity of the motions. It has been experimentally shown that the decaying of ship motions (damping) in still water, may be considered to be a linear function of the angular velocity, for small displacements. As motion displacement amplitude increases, the relationship between fluid resistance and displacement velocity may change continually.

Approximate methods of determining resistance coefficients are available, but each method has its limits. Complex analytical methods for determining roll motions under special conditions also exist. These methods and derivations may be found in most hydrodynamic text books. Practical methods based on empirical formulas are usually employed when determining the motion properties of hulls (Blagoveshchensky, 1962).

Ultimately, experiments still remain the most accurate method of determining ship motions in still water and in waves. These methods, however, serve only as a guide.

The condition of linearity is violated once large displacements occur. These non-linearities manifest themselves as quadratic or more complex functions of velocity and displacement. For roll and some heave cases, a second case of non-linearity occurs in the restoring term. The static stability curve of a hull illustrates the non-linearity of the restoring moment. Non-linearities in the added moment of inertia of a vessel also occur at large amplitudes of roll. The added moment of inertia is then considered to be a function of the angle of inclination.

1.2.4 Restoring forces

These forces are determined with ship hydrostatics. They are often not linearly related to displacement, especially in the roll case for large angles of roll. The degree of non-linearity of the restoring moment is dependent on the geometry of a hull. This may be evident in the non-linear character of the righting arm diagram of that hull. The period and amplitude of the rolling of a vessel are the predominant characteristics of a hull that are of interest in hull motion studies.

1.2.5 External forces

Forces (or moments) which lead to the displacement of a hull, include waves, collisions, projectile impact or explosions and loading or load shifting of cargo. The energy driven into the system (the system being a hull floating in a body of water) is transferred and dissipated predominantly through wave making, vortex shedding and skin friction. Loadings are non-linear and beyond the control of the designer (Ibrahim, 2009).

1.3 Literature Review

Ship hydrodynamics is an essential and ongoing research field. A substantial amount of work has been carried out to determine the hydrodynamic characteristics of hulls. Hull displacements under complex loading conditions are difficult and often impossible to predict. Understanding how a hull will behave under limited and controlled conditions renders insight into how a hull may displace in more complex situations.

Lewis (1929) proposed a method for determining the added mass moment of inertia for various hull shapes. The added mass was described as a function of the shape of the hull under consideration. Conformal transformation based on a circle was employed to approximate actual ship sections.

Vugts (1968) theoretically and experimentally determined the hydrodynamic coefficients of two-dimensional cylinders, by forced oscillations, heaving, swaying and rolling in a free-surface. The influence of section shapes on the coefficients were observed. Differences between the theoretical and experimentally obtained coefficients for sway and roll were evident. Viscous effects were distinctly present in these motions. A complete set of hydrodynamic quantities for motions of cylinders in forced motion and in beam waves were presented.

The implementation of numerical methods originated from potential flow theory. Bishop *et al.* (1980) presented a potential flow solution using conformal mapping and a multipole potential flow method expansion. With this method two-dimensional hydrodynamic properties were computed for cylinders swaying and rolling in the free-surface of an infinite ideal fluid.

Ikeda (2004) described a simplified method to predict the roll damping of ships by considering contributions from friction, wave, eddy, lift and bilge keel components.

Floquet theory (solving ordinary differential equations with linear differential equations) was implemented by Mulk and Falzarano (1994) to solve six degrees of freedom non-linear ship rolling motion. Bifurcation and stability behaviour of the coupled roll were studied. Linear three degrees of freedom and the six degree of freedom results were compared to each other. The non-linear coupling of roll to heave and pitch affected the roll of his three-dimensional hull. Concluding the article, the authors pointed out that all six degrees of freedom must simultaneously be studied.

Heave and sway motions are well predicted with potential flow and other theoretical methods. Roll behaviour is difficult to predict because of nonlinearities. RANS based turbulence modelling methods describe most time-averaged properties of flow very well. A vast majority of turbulent flow (for engineering applications) computations have been carried out with procedures based on the RANS equations (Versteeg and Malalasekera, 2007). RANS based turbulence models include mixing length (Rodi, 1980), Spalart-Allmaras, $k-\varepsilon$ (Launder *et al.*, 1975), renormalization group (RNG) $k-\omega$ (Yakhot *et al.*, 1992), Reynolds stress (Launder *et al.*, 1975), Wilcox $k-\omega$ (Wilcox, 1988) and Menter SST $k-\omega$ (Menter, 1992a) models to name a few. These models are discussed in section 2.3.

A theoretical method of determining the hydrodynamic forces on an oscillating rectangular cylinder was proposed by Yeung *et al.* (1998). Vortical flow in the presence of a free-surface was modelled with a free-surface random-vortex method (FSRVM). The vortical part was solved with the RVM and the irrotational part with a complex-variable boundary element method (BEM). In the RVM, the vorticity field was approximated by a collection of regions of concentrated vorticity in the flow field. The FSRVM was validated by modelling a plate rolling in water and comparing it to experimental data (Yeung and Ananthakrishnan, 1992). This method was also applied to a horizontal circular cylinder translated through a fluid and with a rectangular cylinder heaving in a free-surface (Yeung and Vaidhyanathan, 1994). Yeung *et al.* (1998) carried out an experiment geometrically similar (but not to the same scale) to Vugts' (1968) experiments. Yeung *et al.* (1998) considered 0.3 x 0.3 m flat-bottom hulls, whereas Vugts (1968) considered 0.4 x 0.4 m flat-bottom hulls, this scale discrepancy would have an effect on compared results. Both the FSRVM and experimental results did not fully agree with those presented by Vugts. Reasons for this are unclear. The FSRVM's predictions appear to be lacking in lower frequency oscillations (it is not stated what may be defined as a "low" frequency). In conclusion the FSRVM model required a turbulence model to be included in the method.

Korpus and Falzarano (1997) produced data by applying RANS methods to rolling ship sections. They only considered a rectangular ship section (flat-

bottom-hull) under forced oscillations for heave, sway and roll without the presence of a free-surface. Various roll amplitudes, oscillating frequencies and scales were investigated. Their panel code could not predict damping components satisfactorily.

Finally, a rolling rectangular section in a free-surface, modelled with a RANS-based technique, was carried out by Sarkar and Vassalos (2000). Results were compared to available numerical and experimental results. This technique predicted damping and added moment of inertia coefficients more accurately than potential flow calculations could. The RANS-technique resolved the main characteristics of the rolling motion. Further investigations into turbulence models and grid dependence was recommended.

Rectangular sections (flat-bottom hulls) are investigated more often than other ship sections because of their frequent commercial use. Flow around floating production storage and offloading (FPSO) hulls in roll were investigated by Kinnas *et al.* (2006). A two-dimensional unsteady Navier-Stokes solver was used. The results were compared to that of a BEM based potential flow solver. The effect of turbulence for a submerged hull subject to alternating flow was investigated, using the commercial CFD code FLUENT (version unknown). The Reynolds stress model (RSM) (Launder *et al.*, 1975) with standard wall functions was applied. The difference between the results from turbulent flow and laminar flow in FLUENT (version unknown) were found to be negligible. Roll moment behaved in a very non-linear manner with respect to angle of roll. There was a significant increase in moment as the roll angle increased.

Chen and Liu (2002) implemented non-dimensional RANS equations for this incompressible flow problem. The authors extended their work to investigating the flow characteristics around a three-dimensional hull for initial roll angles of 5° , 10° and 20° . The hull was also sub-divided and the flow characteristics for the different hull cross sections (two-dimensional) were investigated. These cross sections resemble typical hull-like sections. Using orthogonal curvilinear coordinates, a moving mesh was constructed around the hull under consideration. Forced and freely oscillating conditions were considered. The results obtained illustrated the flow phenomenon occurring around the different hull geometries and also the hull characteristics. The results were not directly compared to experimental results.

Investigations into general hull forms are rare compared to the available data for specific hull forms. Kim (2003) and Wilson *et al.* (2006) for example investigated the rolling of existing surface combatants (in three dimensions). An unsteady RANS code (CFDSHIP-IOWA, Paterson *et al.*, 2003) was implemented by both authors. Good qualitative predictions for surface pressure and free-surface elevation were obtained by Kim (2003). Experimental results for this specific hull were not available. Work carried out by Wilson *et al.* (2006) was validated with an uncertainty analysis. The method used accurately predicted seakeeping characteristics for this hull.

Different numerical methods and models are developed and tested for specific application to the non-linear rolling of ship hull sections. A non-linear rolling hull with forward velocity was numerically investigated by Pesman *et al.* (2007). A mid-size twin-screw fishing vessel was considered. Non-linear equations of motion were derived and solved using a fourth order Runge-Kutta solver (Ferziger and Peric', 2002, pg. 141). The effect that damping had on roll amplitude was the main focus of the article. Even though a single hull was employed, no appendages were considered. Pesman *et al.* (2007) found that increasing the metacentric height of a hull (GM) did not reduce peak resonant amplitudes, but shifted the resonant frequency. Bilge-keels were found to damp motion by about 35 % at the ship's resonant frequency.

A strongly non-linear ship model was applied by Lin and Kuang (2008) to the rolling problem. The program DiSSEL (digital self-consistent ship experimental laboratory) was a non-linear ship motion model developed by the authors and used to model a hull numerically. Bilge-keel effects on the roll damping were investigated. The results obtained with this numerical method were in agreement with experimental results. Ship hull forms and geometry above the calm water line were also found to play a role in damping. Different definitions for the roll damping were presented. The sensitivity of the numerical model was not investigated.

One of the later investigations into the hydrodynamic coefficients of ship sections was carried out by Quérard *et al.* (2009). A commercial RANS solver (ANSYS-CFX 10.0, Quérard *et al.*, 2009) was used to model two-dimensional cylindrical sections in heave, sway and roll. The shear stress transport (SST) turbulence model developed by Menter (1994) was used. Circular and rectangular sections were oscillated at frequencies of 1-12 rad/s in an initially undisturbed free-surface. Small displacement amplitudes were considered to compare the hydrodynamic coefficients to potential flow theory. Grid independence was achieved for all cases. A good correspondence between the numerical and experimental hydrodynamic coefficients (Vugts, 1968) was achieved. Quérard *et al.* (2009), however, only considered small displacement oscillations. For the rolling rectangle, grid size, grid structure and time step size strongly influenced the damping coefficient. Vortex shedding was suspected to be the cause of the discrepancies between the numerical results for the roll case.

A direct method for solving the Navier-Stokes equations using the finite volume method was presented by Bangun *et al.* (2010). This method accounted for non-linear free-surface conditions. The model's effectiveness in resolving the effects of vortices on rolling barges with bilge-keels were tested. Vorticity contours and roll hydrodynamic coefficients were calculated from velocity and pressure fields. For this investigation, small roll angles (smaller than 0.14 rad) were tested as the draft of the sections were relatively shallow compared to the half width of the barge. Vortex separation was found to contribute substantially to the damping force. Potential flow theory over-predicted the

roll motion.

A paper by Ibrahim and Grace (2009) presented work carried out by numerous researchers in the field of ship hydrodynamics. The hydrostatic and hydrodynamic forces and moments acting on a ship may be derived using two approaches. The first approach involves a Taylor series expansion of the force function. The second method employs the integration of hydrodynamic pressures acting on a ship's wetted surface. The article was well researched and presents fundamental ship theory. Memory effect was discussed. Ship roll dynamic stability methods mentioned included stochastic roll stability and probabilistic roll dynamics.

From the literature it is clear that unsteady ship hydrodynamics is a field that has a long research history and is still being researched. With the advent of numerical methods and computing power, research methods in this field (and especially for large displacement ship motions) are following a numerical approach. CFD has become a somewhat useful and helpful tool in this field. Of course scaled ship models will always be required to verify numerical results.

1.4 Fundamental Equations of Motion

Equations of motion are used to describe the motion of the hulls in this project. These equations are presented, as by Vugts (1968), to determine the added mass moment of inertia and damping coefficients.

Neglecting coupled motions for heave,

$$(m + a_{zz})\ddot{z} + b_{zz}\dot{z} + c_{zz}z = Z \quad (1.4.1)$$

where: z is a predefined forced vertical displacement and is defined by:

$$z = z_a \sin(\omega t) \quad (1.4.2)$$

For sway,

$$(m + a_{yy})\ddot{y} + b_{yy}\dot{y} = Y \quad (1.4.3)$$

where: y is a predefined forced horizontal displacement and is defined by:

$$y = y_a \sin(\omega t) \quad (1.4.4)$$

and for roll with the roll axis and centre of gravity coinciding and fixed,

$$(I + a_{\phi\phi})\ddot{\phi} + b_{\phi\phi}\dot{\phi} + c_{\phi\phi}\phi = K \quad (1.4.5)$$

where: ϕ is a predefined forced rotation about the x-axis and is defined by:

$$\phi = z_a \sin(\omega t) \quad (1.4.6)$$

The total forces Z , Y and moment K are measured with FLUENT (2009) (as discussed in chapters 3 and 6). Oscillation force and moment amplitudes ($Z_{osc}, Y_{osc}, K_{osc}$) and phase angles ($\varepsilon_Z, \varepsilon_Y, \varepsilon_K$) are determined from Z , Y and K . $m\ddot{z}$, $m\ddot{y}$ and $I\ddot{\phi}$ are not included in the FLUENT (2009) measurements. The equations can be rearranged and the coefficients determined using:

$$a_{zz} = -\frac{Z_{osc} \cos \varepsilon_Z - c_{zz} z_a}{\omega^2 z_a} \quad (1.4.7)$$

$$b_{zz} = +\frac{Z_{osc} \sin \varepsilon_Z}{\omega z_a} \quad (1.4.8)$$

for heave,

$$a_{yy} = -\frac{Y_{osc} \cos \varepsilon_Y}{\omega^2 y_a} \quad (1.4.9)$$

$$b_{yy} = +\frac{Y_{osc} \sin \varepsilon_Y}{\omega y_a} \quad (1.4.10)$$

for sway, and

$$a_{\phi\phi} = -\frac{K_{osc} \cos \varepsilon_K - c_{\phi\phi} \phi_a}{\omega^2 \phi_a} \quad (1.4.11)$$

$$b_{\phi\phi} = +\frac{K_{osc} \sin \varepsilon_K}{\omega \phi_a} \quad (1.4.12)$$

for roll.

1.5 Broad Objectives

The aim of this project is to determine the characteristics of various typical ship-like hull sections through the use of numerical analyses, in order to verify the implementation and application of CFD code on ship motion problems. This project will render some insight into how a hull may be expected to behave in reality through numerical simulation. Rough initial estimates of the roll motion of complete three-dimensional hulls with varying cross-section from bow to stern may be supported by this project. It is also intended that this study will extend the concept of looking at a range of typical hull sections used on numerous ships, and to splice these hull sections to form a complete hull.

1.6 Specific Objectives

The use of numerical methods to determine the hydrodynamic characteristics of different ship-like hull sections in calm water is investigated. Numerical characterisation, of the hydrodynamic properties of a hull, is achieved through calculating damping and hydrodynamic (or added mass) coefficients for equations describing the motions of hulls.

1.6.1 Numerical characterisation and model evaluation

If damping coefficients can be numerically determined and related to specific sections, typical hull sections can be compared quantitatively. This will better the understanding of the typical motion characteristics that may be expected from a specific hull section. A model capable of capturing transition from laminar to turbulent flow is evaluated to investigate the influence of this on hull characterisation. This numerical study is validated through comparison with a set of widely used experimental results.

1.6.2 Presence and effects of fluid phenomena

Different hull geometries and motions produce different fluid flow phenomena (such as wave an and vortex generation and wall friction) around the hull. The effects of these phenomena on hull motions are examined through this study. The applicability of laminar flow and turbulence models may vary between cases, and will be investigated.

1.6.3 Prescribed displacement

Forced motion is often used to conduct numerical and experimental tests on hulls as opposed to free-roll decay. This so-called forced motion is exerted on a hull by prescribing a displacement to a hull. This method is used to expose characteristics which may not be observed with free-roll decay tests.

1.7 Project Scope

This study serves as a tool to determine the behaviour of typical two-dimensional hull sections. The accurate prediction of the behaviour of actual, three-dimensional hulls under various loading conditions, is beyond the scope of this project.

A numerical model is created in a commercially available CFD package, FLUENT (2009). The numerical results obtained are compared to that of available published numerical, theoretical and experimental results found in literature.

Two translational motions and one rotational motion, namely, heave, sway and roll, are investigated. Each motion is described by a sinusoidal displacement. Six different oscillation frequencies between 1 and 12 rad/s are considered. Coupling of motions is neglected.

The hull geometries considered represent typical cross-sections found in hulls at various stations throughout a ship. Three different ship-like hull sections were evaluated. Only one constant fundamental geometrical shape is investigated at a time. Experimental data from literature also regarded motions of single section hulls (cylindrical sections). The hulls investigated are

listed below (see figure 1.2):

Hull 1: V-shaped hull

This type of hull is expected to behave similarly to a keeled hull and the main damping is expected to be produced by waves generated by the hull and also by vortex generation.

Hull 2: Flat-bottom

Because of this hull's flat bottom and small bilge radius, the predominant damping terms were expected to originate from vortices generated by the bilge.

Hull 3: Round-bottom

This shape is analogous to a round cylinder. The predominant damping is expected to result from skin friction from the viscous effects of water interacting with the hull surface.

The damping coefficients of the hulls are expected to vary greatly as each hull has its own special characteristic. With regard to the correlation of the experimental and numerical results, the scale, boundary conditions, hull geometry, and flow domain of the models are identical.

Chapter 2

Computational Approach

2.1 Computational and Fluid Theory

The finite volume method was employed for this numerical investigation. Consider the Navier-Stokes equations for unsteady laminar incompressible flow.

Flow the x-direction

$$\rho \frac{Du}{Dt} = -\frac{\partial p}{\partial x} + \text{div}(\mu \text{ grad } u) + S_{Mx} \quad (2.1.1)$$

Flow the y-direction

$$\rho \frac{Dv}{Dt} = -\frac{\partial p}{\partial y} + \text{div}(\mu \text{ grad } v) + S_{My} \quad (2.1.2)$$

Flow the z-direction

$$\rho \frac{Dw}{Dt} = -\frac{\partial p}{\partial z} + \text{div}(\mu \text{ grad } w) + S_{Mz} \quad (2.1.3)$$

When a body moves (wall boundary) through a viscous fluid (such as water) the fluid velocity near the body tends to zero, with respect to the boundary wall, as the perpendicular distance from the wall decreases. It is assumed that the no-slip wall boundary condition holds (velocity at the wall, with respect to the wall, is zero). The free-stream velocity and the near wall velocity often differ by orders of magnitude. The thin region where the fluid velocity is between near zero with respect to the wall and 99 % of the free-stream velocity is referred to as the boundary layer. High Reynolds numbers are generally indicative of turbulent flow. Viscous effects may become complicated as they provide damping at low and high Reynolds numbers but contribute to destabilisation of the flows at intermediate Reynolds numbers.

The flow around oscillating ship-like sections results in hydrodynamic instabilities affecting the boundary layer. In general, when turbulence arises from flow instability, apparent additional fluid shear stresses are generated. Turbulence results in increased energy losses. Kinetic energy is passed down from larger to smaller eddies. The fluid layers experience additional apparent shear stresses as momentum exchange occurs (slower moving fluid being transported into faster moving fluid). These additional apparent shear stresses are known as Reynolds stresses. Reynold's decomposition is used to characterise turbulent flow properties in terms of time-averaged mean flow properties. Using the time averages of fluctuating properties Reynolds-averaged Navier-Stokes equations may be derived. The RANS equations are defined by:

Flow the x-direction

$$\rho \frac{D\tilde{U}}{Dt} = -\frac{\partial \tilde{P}}{\partial x} + \text{div}(\mu \text{ grad } \tilde{U}) + \left[-\frac{\partial(\overline{\rho u'^2})}{\partial x} - \frac{\partial(\overline{\rho u'v'})}{\partial y} - \frac{\partial(\overline{\rho u'w'})}{\partial z} \right] + S_{Mx} \quad (2.1.4)$$

Flow the y-direction

$$\rho \frac{D\tilde{V}}{Dt} = -\frac{\partial \tilde{P}}{\partial y} + \text{div}(\mu \text{ grad } \tilde{V}) + \left[-\frac{\partial(\overline{\rho u'v'})}{\partial x} - \frac{\partial(\overline{\rho v'^2})}{\partial y} - \frac{\partial(\overline{\rho v'w'})}{\partial z} \right] + S_{My} \quad (2.1.5)$$

Flow the z-direction

$$\rho \frac{D\tilde{W}}{Dt} = -\frac{\partial \tilde{P}}{\partial z} + \text{div}(\mu \text{ grad } \tilde{W}) + \left[-\frac{\partial(\overline{\rho u'w'})}{\partial x} - \frac{\partial(\overline{\rho v'w'})}{\partial y} - \frac{\partial(\overline{\rho w'^2})}{\partial z} \right] + S_{Mz} \quad (2.1.6)$$

Where \tilde{U} is the Favré-averaged velocity.

The second last term in each of the above equations is produced because of the existence of turbulence. Time-averaging operations on the momentum equations discard all details of the instantaneous fluctuations, thus a description of the affect of turbulence on the mean flow is required. According to Versteeg and Malalasekera (2007) the effects of turbulence on the mean flow can be determined by implementing eddy-viscosity turbulence models, large eddy simulation (LES) or direct numerical simulation (DNS). Differences between these turbulence models, namely the LES and DNS, are not discussed because they are beyond the scope of this project. The Navier-Stokes equations are time-averaged for steady state flows and the extra terms that appear in the equations are solved with turbulence models. These turbulence models use additional transport equations (for example for turbulence kinetic energy (k) and turbulence kinetic energy dissipation rate (ω) through which the Reynolds stresses are quantified.

2.2 Turbulence Models in Literature

RANS turbulence models are often employed to solve fluid flow problems for oscillating hulls. Popular turbulence models include the k- ϵ , k- ω and the

Spalart-Allmaras models.

The incompressible RANS equations were solved in conjunction with a $k-\varepsilon$ turbulence model by Korpus and Falzarano (1997). This was for a rectangular cylinder rolling without a free-surface. Even though the $k-\varepsilon$ model was used for most of the flow field, a switch was made to the one-equation $k-l$ model for the viscous sub-layer and buffer zones. The switch was made if Reynolds numbers near the wall were less than 300. This work identified important parameters of ship roll damping. A comparison between these numerical results and available experimental results was not made by Korpus and Falzarano (1997).

A rectangular rolling cylinder at the free-surface was investigated by Sarkar and Vassalos (2000). A RANS solver (COMET), which implements a $k-\varepsilon$ model, was employed. The authors acquired results that correspond well with the experimental data presented by Vugts (1968).

Chen and Liu (2002) used a RANS method in conjunction with a chimera domain decomposition approach (this is an overlapping grid method). A two-layer turbulence model developed by Chen and Patel (1988) was used to solve the Reynolds stresses, however, no experimental results were reported.

Wilson *et al.* (2006) implemented RANS with Menter's blended $k-\varepsilon$ two-equation model (Menter *et al.*, 2006). The near-wall performance of the $k-\varepsilon$ model is unsatisfactory for boundary layers with adverse pressure gradients (Versteeg and Malalasekera, 2007). Wilson *et al.* (2006) compared their work to experimental fluid dynamics (EFD) using particle image velocimetry (PIV). The CFD and EFD conducted by the authors correlated well for the case of free-rolling decay of approximately four oscillations.

Quérard *et al.* (2009) employed a RANS method on rectangular sections in heave sway and roll in a free-surface. Potential flow theory, $k-\varepsilon$ and SST models were compared to experimental data (of Vugts, 1968 and Bishop *et al.*, 1980). For a rectangular cylinder oscillating at a normalised oscillation frequency ($\omega\sqrt{B/2g}$) below and above 0.4 and 1.22 rad respectively, results for roll and heave were very sensitive to altering the turbulence models. It was not mentioned that swaying was found to be sensitive to the choice of turbulence model. Potential flow theory and the SST models over-predicted roll added mass of inertia and damping. The $k-\varepsilon$ model was stated to predict sway and roll fairly well. Medium displacement magnitudes were used (sway and heave = 0.02 m and roll = 0.2 rad/s). For these relatively small displacements, vortex shedding effects on the motion of the hull may not have been severe.

In a different case Korpus (2004) employed the RANS equations for flow around complicated geometries of yacht hulls and appendages. He implemented the $k-\varepsilon$ and Spalart-Allmaras turbulence models separately. It is unclear as to which model performed better. Because his paper focused on optimisation of hull features, Korpus (2004) did not compare his numerical data to experimental data.

Alternative numerical models include those of Kinnas *et al.* (2006). A rectangular rolling hull section in a free-surface was investigated with a potential

flow boundary element (BEM) method. A non-linear roll motion model was used by Pesman *et al.* (2007). Neither Kinnas *et al.* (2006) nor Pesman *et al.* (2007) compared their numerical results to experimental data.

Yeung and Vaidhyanathan (1994) expected highly separated flow for rolling rectangular sections. They implemented a Free-Surface Random Vortex Method (FSRVM) to model the flow around these sections. The heaving motion of the section with the numerical model clearly indicated that flow separation did occur. Yeung and Vaidhyanathan (1994) tested and verified their method by conducting physical and numerical experiments with a rolling plate. Yeung *et al.* (1998) again applied his model to rolling rectangular cylinders but found that their results produce added roll inertia that differ from those measured by Vugts (1968). The authors conducted their own experiments and used them for validation purposes. As mentioned in section 1.3, the experiments were geometrically similar but not identical to those of Vugts (1968).

Numerous numerical methods and techniques were used in research with emphasis on RANS models. Different eddy-viscosity models are available and a large number of these models have been tested. It is not clear which turbulence models are best suited to hull forms in different modes of motions.

2.3 Turbulence Models Theory

The k- ε model (two-equation model) is based on Boussinesq's (1877) proposed model for Reynolds stresses (Launder and Spalding, 1974). This is described by equation (2.3.1):

$$\tau_{ij} = -\overline{\rho u'_i u'_j} = \mu_t \left(\frac{\partial U_i}{\partial x_j} + \frac{\partial U_j}{\partial x_i} \right) - \frac{2}{3} \rho k \delta_{ij} \quad (2.3.1)$$

μ_t is used to describe the overall effect of the local velocity fluctuations and is described by:

$$\mu_t = C_\mu \rho \frac{k^2}{\varepsilon} \quad (2.3.2)$$

k and ε are solved with two additional transport equations in the flow domain. At the boundaries k and ε are either defined or calculated with wall functions (which may be Reynolds number dependent). This model is the most validated and most widely used according to Versteeg and Malalasekera (2007). Viscous stresses and Reynolds stresses have a close resemblance in this model. The normal stresses and turbulent viscosity (μ_t) are isotropic. The k- ε model is one of the simpler turbulence models, it performs well for many industrially relevant flows and it is well established. The major shortcomings of this model arises at low Reynolds numbers, rapidly changing flows, Reynolds stress anisotropy, strong adverse pressure gradients and recirculation regions. This is a high Reynolds number model, which makes use of the law-of-the-wall where a log relationship between y^+ and u^+ is assumed.

The Spalart-Allmaras (one-equation model) model (Spalart and Allmaras, 1992) defines the stresses by taking vorticity into consideration when determining the turbulent viscosity. Consider equation (2.3.3) which describes the Reynolds stresses.

$$\tau_{ij} = -\rho \overline{u'_i u'_j} = \mu_t \left(\frac{\partial U_i}{\partial x_j} + \frac{\partial U_j}{\partial x_i} \right) \quad (2.3.3)$$

In this case μ_t is defined by:

$$\mu_t = \rho \tilde{\nu} f_{v1} \quad (2.3.4)$$

Note, there is no Kronecker delta (δ_{ij}) in equation 2.3.3, which reduces the overall turbulent shear stress. $\tilde{\nu}$ is a kinematic eddy viscosity parameter determined with a transport equation (i.e. an additional equation). The rate of production of $\tilde{\nu}$ is related to the local mean vorticity. f_{v1} is a damping function. This model gives good performance in boundary layers with adverse pressure gradients.

The k- ω (two-equation model) model by Wilcox (1988) defines the Reynolds stresses with equation (2.3.1) and μ_t is defined by:

$$\mu_t = \rho k / \omega \quad (2.3.5)$$

Similar to the k- ε model, k and ω are acquired through solving two additional transport equations. This method is attractive as it does not require wall-damping functions for low Reynolds number type flows. k is zero at the wall. The results of the model are often dependent on the free-stream value of ω . This is a low Reynolds number turbulence model, which requires a very fine grid near a wall boundary in order to resolve boundary-layer scale flows.

The k- ω (two-equation model) Menter model (Menter, 1994) is a hybrid model. It combines the k- ε model for the free-stream flow and the k- ω model for the near-wall regions, thereby exploiting the strengths of these two models. The model employed depends on the proximity of the fluid to the body (or a wall). Because a switch is required between the k- ε and k- ω models, blending functions are used to achieve a smooth transition.

Complex strain fields and significant body forces cannot be predicted very well using the eddy viscosity (isotropic) models. The Reynolds stress equation model (RSM) (five equation model) can account for the directional effects of the Reynolds stress field (Launder *et al.*, 1975). The Reynolds stress is represented by:

$$R_{ij} = -\tau_{ij} / \rho = \overline{u'_i u'_j} \quad (2.3.6)$$

Anisotropy of the small dissipative eddies are now accounted for. The RSM is computationally expensive and is susceptible to convergence problems (numerical issues exist in the source terms coupling mean flow and turbulent stress fields). This is the most general of turbulence models according to Versteeg and Malalasekera (2007). Very accurate mean flow properties and Reynolds stresses are obtained for various flow cases.

The Transition k - k - ω (three equation) model includes transport equations for turbulent kinetic energy (k_T), laminar kinetic energy (k_L) and the inverse turbulent time scale (ω). The shear stresses are determined by equation (2.3.7), which is very similar in form to the Boussinesq equation (2.3.1).

$$-\overline{\rho u'_i u'_j} = \nu_{TOT} \rho \left(\frac{\partial U_i}{\partial x_j} + \frac{\partial U_j}{\partial x_i} \right) + \frac{2}{3} k_{TOT} \rho \delta_{ij} \quad (2.3.7)$$

ν_{TOT} is the sum of the turbulent and laminar viscosities and k_{TOT} is the sum of the turbulent and laminar energies.

This model is physics based rather than correlation based (i.e. incorporating experimental test coefficients or factors). According to Walters and Cokljat (2008) the dynamics of laminar kinetic energy production are not entirely understood. The model adopts a low-Re k - ω boundary layer approach where the increased viscous dissipation in the sub-layer is incorporated into the k_L and k_T terms. The model was evaluated for flat plate and airfoil cases. This model may require further tests and evaluation for validation purposes.

The Transition SST (four-equation) model switches according to the distance from the boundary wall (using a blending function) between the k - ω model for the laminar transition boundary layers and the k - ε model for the free-stream region. This model makes use of a transport equation for intermittency and one for the momentum thickness Reynolds number, for the onset criteria. Menter *et al.* (2006) states that the ability of a low-Re model to predict transition seems coincidental. The use of experimental correlations are favoured in industry over low-Re models. The physics of the transition process is contained entirely in the experimental correlations provided to the model. If appropriate correlations can be provided, this model can be used for all transition mechanisms. The current correlations cover standard bypass transition as well as flows with low free-stream turbulence. The increase in vorticity Reynolds number with increasing shape factor can be used to predict separation-induced transition. This is one of the main advantages to this approach because the standard definition of momentum thickness Reynolds number is not suitable in separated flows. If satisfactory results are obtained from this method in two-dimensions, good results may be expected for three-dimensional cases. The k - ω model must be active in the laminar and transition boundary layer. The Transition SST model was tested with flow over a flat plate by Menter *et al.* (2006). The model was able to predict separation-induced transition and the subsequent reattachment of the turbulent boundary layer. Turbine blade model tests were also conducted and correlated well with available experimental data. A flow separation bubble can also be predicted.

Two-equation, non-linear methods have also been developed to capture turbulence whilst retaining a low computational time. Large eddy simulations (LES) and detached eddy simulations (DES) models will not be discussed. The focus of this project was to investigate RANS turbulence models. LES and DES models can only be implemented for three-dimensional flow cases.

2.4 Turbulence Model Employed

A discussion of different turbulence models is presented in section 5.3. The transition SST model was selected and employed for each case of the oscillating hulls. Because the hulls oscillate in initially still water at the free-surface, there is an expected laminar flow stage followed by a transition to turbulent flow. The effect of transition from laminar to turbulent flow was also investigated. The only transition models currently available in FLUENT (2009) are the transition SST and the transition $k-k\ell-\omega$ models. The transition SST model was chosen over the $k-k\ell-\omega$ model because the first proved to be more applicable (see section 5.3). The transition SST model is a correlation based model, which is preferred because there is uncertainty in the actual physics of transition. Even though the $k-k\ell-\omega$ model makes use of the inverse turbulent time scale (ω), at the wall boundary a low Reynolds $k-\varepsilon$ approach is followed. It is desirable to use the $k-\omega$ approach as this is more accurate for near boundary flows than the $k-\varepsilon$ model. Transition models may be inappropriate for flows where vortex shedding has a much greater influence on the damping of hulls than flow separation. Once the flow switches from laminar to turbulent models (in reality the flow does not switch from laminar to turbulent flow at the same point) the $k-\omega$ model is implemented. Two-equation turbulence models (eg. $k-\varepsilon$ $k-\omega$) do not capture the relationship between turbulent energy production and turbulent stresses caused by anisotropy (i.e. when vortex shedding occurs) of the normal stresses.

2.5 Numerical Methods and Models

Cell-centred pressure-based solvers employ an algorithm wherein the mass conservation of the velocity field is constrained through solving a pressure (pressure correction) equation. This pressure equation is derived from continuity and momentum equations. Velocity is obtained from solving these momentum equations. For this project a segregated algorithm (pressure implicit with splitting of operators, PISO) is employed, the governing equations are solved sequentially. Segregated algorithms are memory-efficient but solution convergence is slow.

The pressure-based solver was initially developed for low speed incompressible flows (FLUENT, 2009b, pg. 652). Whereas the density-based solver was developed for high-speed compressible flows. The energy equation need not be solved when using the pressure-based solver.

The volume of fluid (VOF) model (discussed later) is only compatible with the pressure-based solver. The fluid flow problem of a hull oscillating at the free-surface may be regarded as an incompressible fluid problem (both the air and water are defined to be incompressible), heat transfer is not considered.

The incompressible air has a negligible effect on the damping of the water surface waves.

A pressure-based solver is chosen because of the presence of a free-surface which is a region where there is a rapid change in density. This rapid density change cannot be handled as well with the density-based solver as with the pressure-based solver. For the pressure-based solver, pressure between cells must be solved. The derivative of density with respect to pressure is required to solve the Navier-Stokes equations.

The interface between the two fluids (water and air) must be captured so that the forces of the fluids exerted on the hull can be determined. Quérard *et al.* (2009) used the VOF model to describe the free-surface in their numerical investigation. According to Korpus (2004) the VOF method is gaining popularity. Sarkar and Vassalos (2000) used the high resolution interface capturing (HRIC) technique (developed by Muzaferija and Peric (1998)). The HRIC technique is an extension of the VOF method. Chen and Liu (2002) and Korpus (2004) used a free-surface method described by Chen and Chen (1998) and Chen *et al.* (2000). Free-surface turbulence and surface tension were ignored. This free-surface approach is more complicated than the VOF method (Korpus, 2004). The VOF method interpolates the free-surface from solutions of a continuum variable. The variables representing the VOF free-surface diffuse because it is a discrete computational method. This diffusion results in the free-surface becoming 'thick'. An advantage of the VOF method is that it does not require regridding. If overset/chimera grids (Benek *et al.*, 1985) are employed, the VOF method loses its advantage.

Kim (2003) and Wilson *et al.* (2006) used a CFD software package CFD-SHIP-IOWA, which includes its own free-surface tracking technique. Two free-surface boundary conditions based on linear wave theory were applied by Kinnas *et al.* (2006). Bangun *et al.* (2010) employed an interface tracking method based on one developed by Muzaferija and Peric (1998)

The volume of fluid (VOF) model, with the explicit scheme for time discretization, was employed to capture the free-surface for this project. Obtaining a well defined free-surface in the computational domain for this case is not critical, when considering the additional complexity and computational time required for the other models. In addition, overset grids are not employed making the use of the VOF method more advantageous than other methods. For the purposes of this study, the fluids are assumed to be immiscible. The variables and properties of the fluid in a cell at the free-surface may be representative of a mixture of the two phases being considered. The volume of fraction of the fluids are tracked and a single set of momentum equations are solved for modelling the free-surface. Consider:

$$\frac{1}{\rho_q} \left[\frac{\partial}{\partial t} (\alpha_q \rho_q) + \nabla \cdot (\alpha_q \rho_q \vec{v}_q) = \sum_{p=1}^n (\dot{m}_{pq} - \dot{m}_{qp}) \right] \quad (2.5.1)$$

If the value of α_q assumes unity, the cell is full of fluid q , if its value is zero the cell is full of fluid p . Between zero and unity the cell contains the interface between the two phases.

FLUENT (2009) does not solve the VOF equation at every time step. Solving the equation at every time step is more accurate for dynamic meshes, however, the computational cost is high. FLUENT (2009) automatically uses its own time step for the VOF calculation; this is based on the Courant number entered. The Courant number compares the time step specified to the characteristic time of transit of a fluid element across a control volume. Consider the Courant number equation:

$$Courant\ number = \Delta t \left(\frac{\Delta x_{cell}}{v_{fluid}} \right) \quad (2.5.2)$$

The Courant number is set to 0.25 (by default), Δt used per calculation is based on equation (2.5.2)

The explicit time discretization allows the Geo-Reconstruct discretization scheme to be used which is a robust and accurate scheme. Poor convergence may occur in skewed meshes or if phases are compressible. The explicit scheme requires the volume fraction values at the previous time step as opposed to the current time step, as for the implicit scheme. The explicit time discretization scheme solves the following VOF equation:

$$\frac{(\rho_q \alpha_q)^{n+1} - (\rho_q \alpha_q)^n}{\partial t} + \sum_{nb} \nabla \cdot (\rho_q \alpha_q \mathbf{v})^n = \left[\sum_{p=1}^n (\dot{m}_{pq} - \dot{m}_{qp}) \right]^n \quad (2.5.3)$$

According to FLUENT (2009a) the VOF model has numerous limitations. This model can only be employed with a pressure-based solver. Only one phase may be defined as compressible. Second order implicit time-stepping formulation cannot be used with the VOF explicit scheme.

Interpolation near the free-surface was solved in FLUENT (2009) with a geometric reconstruction scheme (Geo-Reconstruct). The interface between the fluids are represented using a piecewise-linear approach. It is assumed that a linear slope for the interface exists within each cell. The advection (transport) of the fluid through the cell faces are calculated using this linear shape. From information of the volume of fraction and its derivatives, the position of the linear interface relative to the centre of each partially-filled cell is determined. The amount of fluid transported through each face using the computed interface representation is calculated. The normal and tangential velocity distribution on the face is obtained. Using the balance of fluxes, the volume of fraction in each cell is calculated. This scheme is applicable to unstructured meshes.

The oscillating hull flow case is a transient flow problem. Temporal discretization has to be considered.

Pressure and velocity for a flow field is usually unknown, but are coupled by the continuity and momentum equations. If the velocity field for the computational domain is obtained, all other flow variables can be determined. Pressure-velocity coupling algorithms are used to compute these flow field variables. Rewriting the Navier-Stokes momentum equations in two dimensional form illustrates this coupling:

$$\frac{\partial}{\partial x}(\rho uu) + \frac{\partial}{\partial y}(\rho vu) = \frac{\partial}{\partial x} \left(\mu \frac{\partial u}{\partial x} \right) + \frac{\partial}{\partial y} \left(\mu \frac{\partial u}{\partial y} \right) - \frac{\partial p}{\partial x} + S_u \quad (2.5.4)$$

$$\frac{\partial}{\partial x}(\rho uv) + \frac{\partial}{\partial y}(\rho vv) = \frac{\partial}{\partial x} \left(\mu \frac{\partial v}{\partial x} \right) + \frac{\partial}{\partial y} \left(\mu \frac{\partial v}{\partial y} \right) - \frac{\partial p}{\partial y} + S_v \quad (2.5.5)$$

Continuity equation:

$$\frac{\partial}{\partial x}(\rho u) + \frac{\partial}{\partial y}(\rho v) \quad (2.5.6)$$

Non-linearities exist in the convective terms of the momentum equations and all three equations are intricately coupled. Constraining pressure and velocity through coupling, allows the velocity of a flow field to satisfy continuity if the correct pressure field is applied in the momentum equations. These two issues are resolved with an iterative solution approach.

Popular algorithms found in literature include the semi-implicit method for pressure linked equations (SIMPLE), the SIMPLE revised (SIMPLER), for large grids. For unstructured grids and time dependant flows, the pressure implicit with splitting of operations (PISO) algorithms is often employed.

The SIMPLE algorithm was used for pressure correction in the numerical investigation conducted by Sarkar and Vassalos (2000), along with an unstructured collocated finite-volume technique. Chen and Liu (2002) implemented the hybrid PISO/SIMPLER pressure solver to ensure that the equation of continuity is satisfied at each time step. The program CFDSHIP-IOWA used by Kim (2003) and Wilson *et al.* (2006) makes use of the PISO algorithm for pressure-velocity coupling. Kinnas *et al.* (2006) and Bangun *et al.* (2010) employed a two-dimensional Navier-Stokes solver with the SIMPLE algorithm.

The PISO algorithm (Issa, 1986) is a segregated type of pressure-based solver and was employed because it has various advantages. This algorithm is very stable (i.e. converges easily) even with under-relaxation factors of 1.0 for momentum and pressure. The algorithm may require more computational time because of additional steps, but solutions converge quicker than with the SIMPLE and SIMPLER schemes. This quicker convergence leads to less iterations required resulting in less overall computational time, according to FLUENT (2009*a*, pg. 682) and Versteeg and Malalasekera (2007, pg. 196). This algorithm is recommended by FLUENT (2009*b*, pg. 1454) for transient flow cases and also for large cell skewness.

2.6 Discretization Schemes

Pressure discretization for the VOF method include the body-force-weighted scheme and the pressure staggering option (PRESTO!). The body-force-weighted scheme assumes that the normal gradient of the difference between pressure and body forces is constant. With this assumption the pressure is calculated. This method works well if the body forces in the flow case are known. This method is applied for cases where discontinuity of explicit body forces and pressure gradients are present (for rapidly changing densities). In the PRESTO! scheme, a discrete continuity balance for a control volume about its face is used to compute the pressure. According to FLUENT (2009b) the PRESTO! scheme should be used for flows with high-speed rotating flows, flows involving porous media and flows in strongly curved domains. The PRESTO! scheme was used in this project because porous zone boundary conditions were initially implemented.

The gradient of scalar fluid variable (ϕ) (for example pressure, and temperature) must be known to determine values of these scalars at cell faces. This scalar variable gradient is used in the discretized transport equations.

The gradient of ϕ may be determined using two techniques namely the Green-Gauss node-based (GGNB) and the Green-Gauss cell based (GGCB) schemes. The GGNB scheme utilises the values of ϕ at the nodes of a cell, and the GGCB scheme uses the values at the cell centres of surrounding cells, to determine the value of ϕ at the cell faces. The cell face values are then used to calculate the gradient of ϕ at the cell centre.

The GGNB scheme is used in various free-surface flow cases. For a box falling into water with an initially still free water surface (FLUENT, 2006), the GGNB scheme was used with the VOF model. It is, however, stated in FLUENT (2007) that only the GGCB scheme was tested with the VOF model. The GGNB and GGCB schemes were tested in a microchannel flow case by Gupta *et al.* (2009). The GGNB scheme produced results that captured the physical phenomenon of a bubble moving through the channel better than the GGCB scheme.

Even in unstructured grids the GGNB scheme preserves second-order spatial accuracy. According to FLUENT (2009a) the GGNB gradient scheme is known to be more accurate than the GGCB scheme, however it is more computationally expensive.

The gradient of a scalar ϕ is calculated at the centre ($c0$) of a cell. Consider the discrete form:

$$(\nabla\phi)_{c0} = \frac{1}{V} \sum_f \bar{\phi}_f \vec{A}_f \quad (2.6.1)$$

For the Green-Gauss Node-Based gradient scheme:

$$\bar{\phi}_f = \frac{1}{N_f} \sum_n^{N_f} \bar{\phi}_n \quad (2.6.2)$$

$\bar{\phi}_n$ is the weighted average of the cell values surrounding the nodes.

The GGNB gradient scheme was employed for this project for its accuracy and because of the potential of skewed cells, due to the presence of a moving (dynamic) mesh in the inner region of the computational domain surrounding the oscillating hull.

The second-order upwind differencing scheme was used for the discretization of momentum, turbulent kinetic energy (k), specific dissipation rate (ω), intermittency (γ) and momentum thickness Reynolds number ($Re_{\theta r}$). Some of these properties are specific to the transition SST model. The second-order upwind scheme is second-order accurate. With this scheme a multidimensional linear reconstruction approach is used to compute flow field variables at the cell faces (FLUENT, 2009a, pg. 662). A Taylor series expansion of the cell centred solution about the cell centroid is utilised. The face value ϕ_f is obtained with the following equation:

$$\phi_{f,SOU} = \phi + \nabla\phi \cdot \vec{r} \quad (2.6.3)$$

\vec{r} is the displacement vector from the upstream cell centroid to the face centroid. $\nabla\phi$ is determined with equation (2.6.4) (Anderson, J.D. (Jr.), 1995) written in one-dimensional form:

$$\nabla\phi = \frac{\phi - 4\phi_{i-1} + \phi_{i-2}}{2\Delta x} \quad (2.6.4)$$

This equation would be implemented for fluid flow from left to right into point i in the x-direction.

The first-order implicit temporal discretization scheme is the only option that is available in FLUENT (2009) with the VOF explicit scheme. Every term in the differential equation is integrated over a time step Δt . The spatial discretization remains the same for transient simulations. Consider the rate of change of a fluid property over time:

$$\frac{\partial\phi}{\partial t} = F(\phi) \quad (2.6.5)$$

F includes the spatial discretization. Using the backwards differencing scheme (for first order accuracy) the temporal discretization is:

$$\frac{\phi^{n+1} - \phi^n}{\Delta t} = F(\phi^{n+1}) \quad (2.6.6)$$

It is solved iteratively at each time level before continuing to the next time step. This method is unconditionally stable with respect to time step size.

Chapter 3

Numerical Solver Settings

Stellenbosch University's Rhasatcha computer cluster was used to carry out all numerical simulation. The cluster consists of 168 cores of 2.83 GHz each (21 nodes and a main head node). A total of 336 GB of memory is available. The head node has a E5420 (2.33 GHz) Harpertown 45 nm Quad-core processor and 4 GB of FBDIMM memory. Each of the 21 computer nodes has $2 \times$ E5440 (2.83 GHz) Harpertown 45 nm Quad-core processors and 16 GB of FBDIMM memory. Only 8 processors were used per simulation because of availability of the machine. Each simulation for a 72 204 cell grid (128 417 faces, 56 213 nodes) and for 83 800 time steps, using 8 cores, took approximately 48 hours to run.

For the first two time steps of each case laminar flow was modelled. After these two time steps the turbulence model was activated. This produced initial input velocities for the turbulent case, which greatly improved stability for starting up the simulation. It is known that the flow in the initial stages of the case is laminar, because the hull starts from rest in an initially still free water surface.

3.1 Model and Material Settings

The pressure-based solver was selected in FLUENT (2009). The flow simulation is transient. The two-dimensional space is planar. Gravity is enabled and set to -9.81 m/s^2 in the y -direction (in the mesh space x is positive to starboard and y is positive vertically upward)

The VOF model with the explicit time discretization scheme is set for interface capturing. The maximum Courant number allowed near the free-surface is set to 0.25 (the default value). This means that the time step used for calculations should be a quarter that of the minimum transit time for any cell at the free-surface. This condition is met throughout all simulations. Convergence was achieved without the use of a correction term for the body force equation. The energy equation is not solved because incompressible fluid with a

constant density is considered. Heat transfer also does not play any significant role in these fluid flow cases. The transition SST model (Menter, 1992a) was employed for all the flow cases that are compared to the experimental data. No model constant values are available at present for the transition SST model for this type of case. All model constants were kept at their default FLUENT (2009) values as shown in table C.1.

Water and air were set as the two interacting fluids. Both fluids are regarded as incompressible. The properties of both fluids were taken from the FLUENT (2009) data base (table 3.1). In FLUENT (2009) primary and sec-

Table 3.1: Properties of the fluids considered

	Water (liquid)	Air
Density [kg/m^3]	998.2	1.225
Kinematic viscosity [$kg/m.s$]	100.3×10^{-5}	1.7894×10^{-5}

ondary phase fluids must be stated. The fluid flowing out of the pressure boundaries is replaced by the primary fluid. For this reason, water is set as the secondary phase and air is set as the primary phase.

There are two cell zones, the moving fluid zone (labelled as 'Triangular Cell Zone' in figure 4.2) and the remaining main-domain. The moving fluid zone is fixed with respect to the hull that it surrounds. Both zones contain a mixture of water and air. The operating pressure is set to 101.325 kPa. Because pressure boundaries are assigned to the computational domain, a reference pressure location is not required (the location is ignored by FLUENT (2009)).

3.2 Boundary Conditions

The computational domain dimensions must be limited to feasibly solve this fluid dynamics problem. Boundary conditions are vital in achieving accurate and computationally limited solutions. A thorough investigation was conducted in determining and implementing appropriate boundary conditions to achieve maximum accuracy.

3.2.1 Boundary conditions in literature

In the numerical studies conducted by Bangun *et al.* (2010), Wilson *et al.* (2006) and Kinnas *et al.* (2006), the free-surface and hull sections were defined as kinematic boundaries. The computational domain ended at the free-surface (i.e. only one fluid, namely water, was considered). No mass flux passed through the their so-called 'kinematic boundaries' and the normal fluid velocities were equal to the normal boundary velocities. Further, force equilibrium was enforced at the free-surface. Free-surface tension was neglected. Dirichlet

pressure boundary and Neumann boundary conditions for the velocity (using linear wave theory, Chadwick *et al.* (2004)) were set at the free-surface.

The no-slip boundary condition was applied at the hull surface (zero tangential and normal velocity). The hull surface was also treated in the same manner by Sarkar and Vassalos (2000).

The above mentioned authors assumed that the fluid along the sea bed (bottom boundary) and at the so-called far field boundaries (boundaries of the the solution domain) to be at rest. A no-slip wall boundary condition was implemented. Bangun *et al.* (2010) and Sarkar and Vassalos (2000) claimed that their far field boundaries were placed far enough to avoid reflection of the body radiated waves during the periods of their simulations. This distance was three wave lengths of the outgoing waves (Bangun *et al.*, 2010). Kinnas *et al.* (2006) terminated their FPSO roll motions simulations before the hull-generated waves reached the far-boundaries.

To determine the position of the far wall boundaries, Sarkar and Vassalos (2000) used the inviscid-fluid dispersion relation of deep-water gravity waves at the boundaries. Homogeneous Neumann boundary conditions for velocities were also tested. The differences between the boundaries were found to be negligible as long as no reflection occurred from the far field. The simulation time was kept lower than the time required for the radiated waves to reach the outer boundaries.

Quérard *et al.* (2009) set the bottom and side far-boundaries to free-slip walls. The top boundary was set to a Neumann boundary condition with static pressure equal to 0 Pa.

3.2.2 Boundary conditions implemented

In this numerical simulation the boundaries were handled in a similar way to the methods found in literature except for the far-boundaries. All boundary condition tests were carried out for a v-bottom hull heave case.

The free-surface was not treated as a boundary but rather as a fluid interface. An upper horizontal boundary was set to limit the computational domain in the vertically upward direction. Initially a pressure outlet boundary condition was implemented. This led to solution divergence. Because the side boundaries are pressure outlet conditions, numerical instabilities occur at the meeting points of these boundaries. Either the computational domain geometry or the boundary condition may be changed. It was recommended Thiart (2010) to define the top boundary as a 'slip' wall boundary. This so-called slip wall is defined to have no wall roughness and no shear stress along the wall. No flow perpendicular to the wall is allowed. The boundary definition becomes more robust and convergence more stable. The distance of the upper boundary from the free-surface was determined by comparing different simulation results. The difference between the results obtained for a case where the upper boundary is 0.9 m from the free-surface, and one where it is 2.2 m

from the free-surface were tested. No differences in the total forces exerted on the hulls were measured.

The bottom horizontal boundary (figure 3.1) was defined as a wall boundary. The no-slip condition is implemented (i.e. 0 fluid velocity at the wall). The pressure along this region is equal to the hydrostatic pressure of the water, as calculated by FLUENT (2009) after the first time step. The distance of the bottom boundary is predefined by the experimental set up of Vugts (1968). Vugts (1968) varied the water depths between 1.80 m and 2.25 m, these depths depended on the models that were tested. For this study the upper depth value of 2.25 m was used. The deeper water level minimises the effects of the bottom boundary on the forces exerted on the hull. It was noted that the pressure at the bottom wall does not remain entirely constant throughout the simulations. This pressure discrepancy is, however, acceptable as the pressure differences did not exceed 3 Pa along a horizontal plane 2.24 m below the free-surface, where the average pressure is 21 934 Pa.

The hull was treated as a moving wall boundary. The no-slip condition was enforced on the boundary surface. Vugts (1968) considered forced oscillations of model hulls. These oscillations were described as functions of displacement. In order to compare this project's numerical results to that of Vugts (1968) experimental results, forced oscillations were considered. The oscillating motion are described through means of a user-defined-function (UDF). This function is written in C code and was compiled with FLUENT (2009) so-called 'interpreter'. The hull motions were assigned to the UDF. The center of gravity (CoG) of the hull is displaced sinusoidally as described by equations (3.2.1)-(3.2.3).

For heave:

$$z = z_a \sin \omega t \quad (3.2.1)$$

For sway:

$$y = y_a \sin \omega t \quad (3.2.2)$$

For roll:

$$\phi = \phi_a \sin \omega t \quad (3.2.3)$$

As mentioned in section 1.2, in this case, the CoG coincides with the intersection of the hull centre-line and initial free water surface. It is assumed that the axis of rotation is about the CoG. Three different hull motions were assigned to each hull at six different frequencies per motion. The different motions are tabulated in table 3.2.

A major challenge was to minimize the disturbance of the waves generated by the oscillating hull and reflecting from the far-field boundaries. Various far-field boundaries (vertical side boundaries) were investigated. Initially, wall

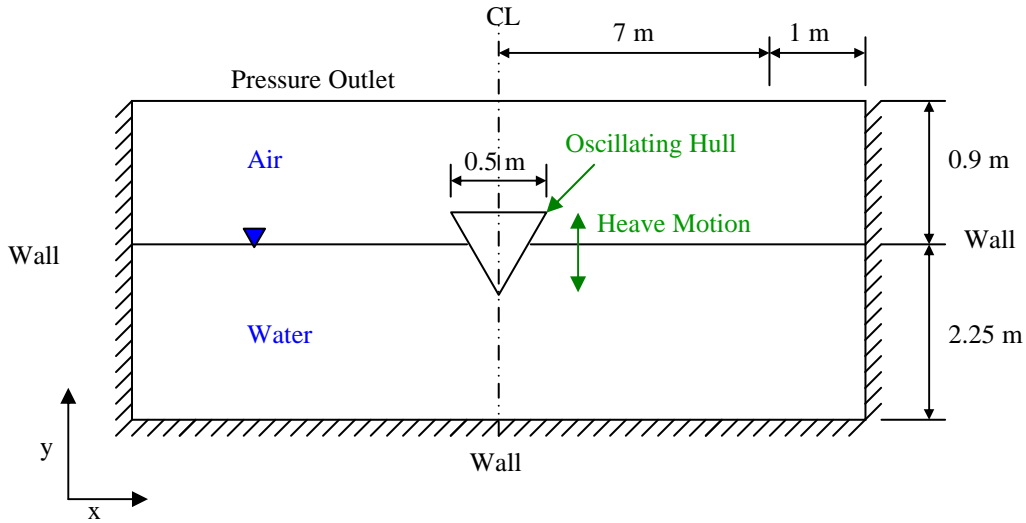


Figure 3.1: Diagram (not to scale) of the computational domain and wall boundary conditions

Table 3.2: Prescribed motions of the hulls

Motion	Displacement	Frequency [rad/s]					
		ω_1	ω_2	ω_3	ω_4	ω_5	ω_6
Heave	0.03 m	1.129	3.023	4.917	6.811	8.705	10.599
Sway	0.03 m	1.129	3.023	4.917	6.811	8.705	10.599
Roll	0.20 rad	1.129	3.023	4.917	6.811	8.705	10.599

boundaries were placed a distance from the hull to observe the number of cycles that the hull can oscillate before the reflected waves influenced measurements (figure 3.1). It was found that for boundaries placed 7 m from the hull, the time taken for wave disturbance to affect the results was proportional to the wave speed. For the test case of a hull oscillating with a frequency of $\omega = 10.599$ rad/s the disturbance occurred at approximately 5 s. Using linear deep water wave theory (Chadwick *et al.*, 2004), and assuming that the wave amplitude is equal to the oscillation amplitude, a wave speed of approximately 3 m/s was calculated. It was difficult to determine exact interference times. Numerous computational domain sizes were tested, the measured force curves were used to visually determining at what time instances the curves varied from each other. This is not a robust method, but only a rough indication of the time before interference occurred was required. This proved that for a wall boundary placed 7 m from the hull, merely 2 or 3 complete hull oscillations could be carried out before wave reflection influenced the results. As mentioned in section 6.1, an excess of 15 complete oscillations had to be executed to obtain usable results. This led to two options being considered: a much larger computational domain could be constructed and simulations run until

interference occurred, or a different boundary condition could be implemented. The conventional increase in domain size requires unacceptable computational time.

A porous boundary condition was tried (figure 3.2). This boundary consisted of a 7 m distance between the hull and the start of a porous boundary zone. The porous zone spanned an additional 1 m. A porosity factor of 0.1 was set to the porous zone. This simulation set up produced results with a lag in the time taken for the wave interference to occur.

Finally an open channel pressure outlet boundary condition (OCPOBC) was exploited (figure 3.3). This boundary was implemented in an example given in FLUENT (2007) for a simulation of a ship sailing through a still body of water. In the example the hull is stationary and a velocity is prescribed to the surrounding fluid. The OCPOBC is applied downstream of this hull. The OCPOBC was applied to all the oscillating hull simulation cases in this thesis. According to FLUENT (2009b) open channel theory is often used to determine wave propagation and the OCPOBC is employed for marine applications. Gravity and inertia dominate these open channel flow cases. The OCPOBC is defined by:

$$p_0 = \frac{1}{2}(\rho_{mix})v^2 + (\rho_{mix})|\vec{g}|(\hat{g} \cdot (\vec{b} - \vec{a})) \quad (3.2.4)$$

The first term on the right hand side represents the dynamic pressure and the second term the static pressure. It is assumed that the free-surface is horizontal and normal to g . This assumption holds because the waves generated by the hull have small amplitudes and large wave lengths. If the flow is sub-critical ($F_r < 1$) then the pressure is taken from the pressure profile specified over the boundary, otherwise the pressure is taken from neighbouring cells. The Froude depth number (F_r) is defined by:

$$F_r = \frac{V}{\sqrt{gy}} \quad (3.2.5)$$

Defining the pressure outlet boundary conditions, an initial water level y is specified which is used by FLUENT (2009) for calculations. As surface waves produced by the oscillating hull progress, the appropriate water level is applied to the boundary. In this way hydrostatic pressure is maintained where free-surface effects become negligible. Inflow and outflow of the two fluids (phases) at the boundaries is allowed. The conservation of mass may, however, be problematic for coarse meshes, as the conservation of the Bernoulli integral does not provide the conservation of mass flow rate for the pressure boundary.

In FLUENT (2009) the boundary backflow direction specification method can be used to specify how the fluid flowing across the boundary out of the computational domain is replaced. The replacing fluid is specified to flow back normal to the boundary. The turbulence specification methods used are intermittency, k and ω . Backflow intermittency, backflow turbulent kinetic

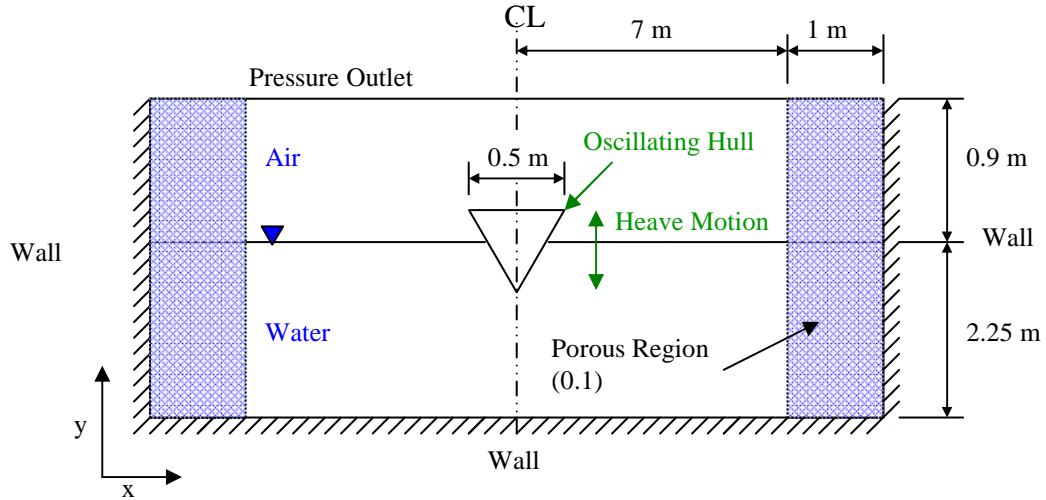


Figure 3.2: Diagram (not to scale) of the computational domain and porous boundary conditions

energy and backflow dissipation rate are all set to 1. The intermittency factor is a measure of the probability that the point under consideration is located inside a turbulent region. If the value is 0 the point is upstream/outside of a turbulent region. In the far boundary region the intermittency should be 0.

The backflow can be predetermined with formulas provided by FLUENT (2009b). These flow properties are dependent on the turbulence intensity of the backflow. The flow velocities at the far field boundaries are very small. A very low turbulence intensity of 0.05 % is assumed. Consider the following equations proposed by FLUENT (2009b):

$$I \equiv \frac{u'}{u_{avg}} \quad (3.2.6)$$

$$l = 0.07L \quad (3.2.7)$$

For this two-dimensional case the depth of the water (2.25 m) is used.

Using the turbulence intensity, the turbulent kinetic energy may be determined with:

$$k = \frac{3}{2}(u_{avg}I)^2 \quad (3.2.8)$$

It may be assumed that the far field velocity (u_{avg}) is very small (a non zero velocity of 0.00005 m/s is assumed for calculation purposes).

Estimating the specific dissipation rate from a length scale (l):

$$\omega = \frac{k^{1/2}}{C_{\mu}^{1/4}l} \quad (3.2.9)$$

The above equations were used to calculate the relevant flow properties (see appendix A). The values of the turbulent kinetic energy and specific dissipation rate are very close to 0. A value of 0 is thus sufficient for the constants of

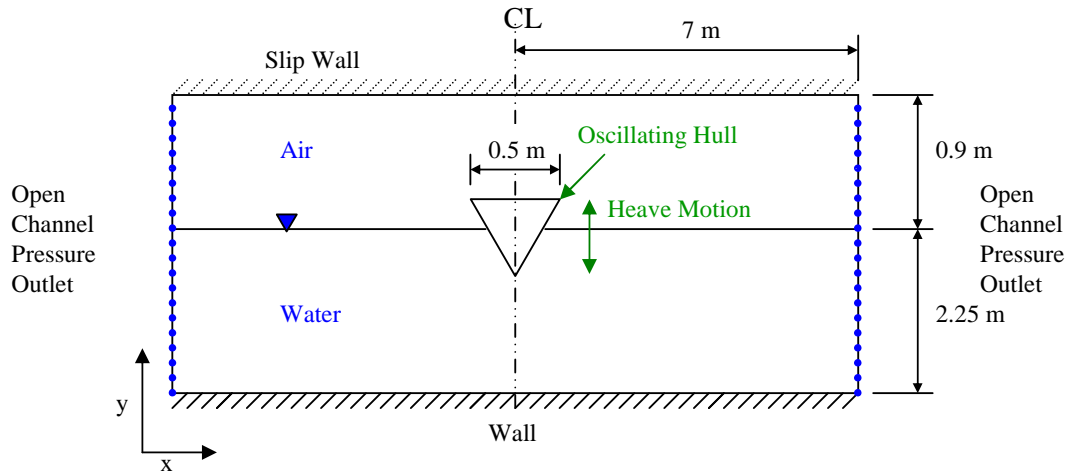


Figure 3.3: Schematic (not to scale) of the computational domain and open channel pressure outlet boundary conditions

these flow properties at the boundaries. As mentioned a value of 1 was set at the boundaries, this is because these settings were overlooked. The effect of these settings are assumed to be negligible because the boundaries are far from the hull and the turbulence is dampened out very quickly. An investigation was conducted for a flow case with the correct settings. Referring to figures 5.6 and 5.7, there is no difference between the current and the adjusted boundary conditions ('Mod BC').

FLUENT (2009) does not have the new 'beach function' boundary condition like FLUENT version 13.0. This boundary condition was not investigated. The principle of this beach function employs numerical diffusion to 'dampen' out the generated waves. The distance at which these open channel boundaries had to be placed was determined through trial and error. Numerous simulations for different computational domain sizes were conducted for the heave case of a v-bottom hull oscillating at 10.599 rad/s (table 3.3).

Table 3.3: Distances of the open channel pressure outlet boundary conditions from the oscillating hull

Motion	Displacement	Distance of OCPOBC from hull [m]					
		Case 1	Case 2	Case 3	Case 4	Case 5	Case 6
Heave	0.03 m	1.5	2.5	5	7	10	15

The amplitude and phase angle of the force measured (figure 3.4) was determined for each complete oscillation. These values were obtained visually (i.e. through plotting graphs and reading off values). It was not practical to carry out statistical analyses on this data as too few data points are available. The average change of the values of force amplitudes and phase angles with

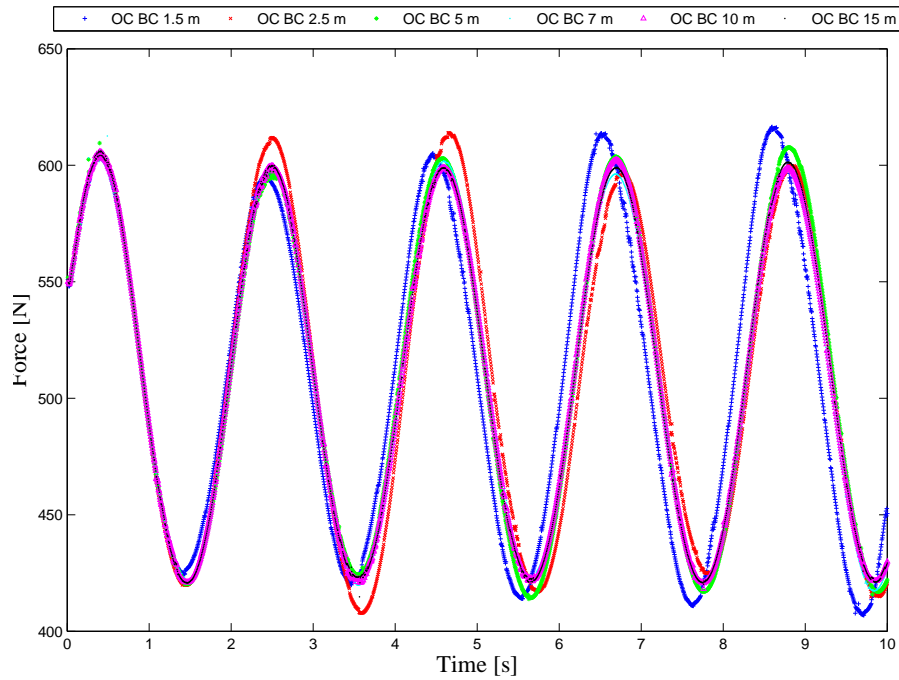


Figure 3.4: Total vertical force measured on a heaving v-bottom hull for various different domain sizes with open channel pressure outlet boundary conditions

respect to the average values of the previous computational domain (i.e. the smaller domain) were plotted (figure 3.5). Consider:

$$(\% \text{ Change of Average})_i = \left| \frac{(Average_i - Average_{i-1})}{Average_{i-1}} \right| \quad (3.2.10)$$

i is the computational domain size under consideration.

The variation in the force amplitude is small from domain size to domain size. It must be remembered that the differences between successive crests or troughs may be up to 6 N. The phase angle transition from small to larger computational domains is not as smooth as the force amplitudes. This jump in figure 3.5 may reveal the distance from the oscillating hull where the water velocity is low and that the free-surface is calm. This condition renders the pressure outlet boundary conditions adequate. If the circular velocity of the water in the wave zone (as in the case of waves with large wavelengths) is small, its effect on the boundaries is negligible. 7 m was found to be a sufficient distance from the hull because it produced results similar to that of cases with 10 m and 15 m boundary placement distances.

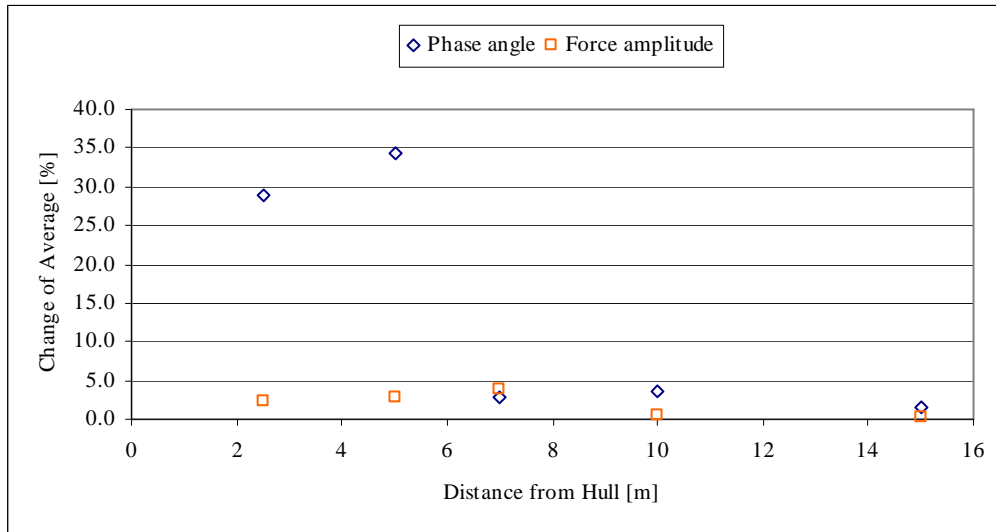


Figure 3.5: Percentage change of the amplitudes and phase angles from one computational domain to the next

3.3 Dynamic Mesh

Every flow simulation in this investigation is concerned with an inner oscillating wall-boundary. The fluid flow near the surface and in close proximity to the hulls under consideration are of interest. With a dynamic mesh, regions where remeshing is required during simulation may be allocated further from the hull. This is done by prescribing a zone around the oscillating hull which moves with the hull. For the heave and sway cases a square moving-fluid-zone ('triangular cell zone' in figure 4.2) was constructed around the hulls. In the roll case a circular moving-fluid-zone (see 'inner mesh region' in figure 4.7) was created to minimise cell skewness in the remeshing zone. More details are given in chapter 4 and subsection E.1.

3.4 Solution Settings

3.4.1 Reference values

Reference values are required by FLUENT (2009) for purposes of calculating the drag lift and moment experienced by the hull (see section 3.4.6). Area is assigned a value of 1 m^2 , density is 1.225 kg/m^3 , length is 1 m and velocity is 1 m/s .

3.4.2 Pressure velocity coupling

The PISO pressure-velocity scheme was selected. Within the PISO algorithm, numerous pressure correction calculations are carried out per iteration. Af-

ter each PISO iteration the corrected velocities converge closer to satisfying the momentum equations. This internal iteration process is the so-called neighbour-correction. If cells are slightly skewed a skewness correction may be used to better approximate the relationship between the mass flux at the cell face and the pressure correction at the adjacent cells. This is achieved through internal iteration pressure-correction gradient calculations. The final pressure-correction per iteration is then used to update the mass flux correction. The skewness correction improves convergence (i.e. convergence is smooth and the number of iterations required reduced). Skewness-neighbour coupling is employed. This coupling applies skewness correction for each separate iteration of neighbour correction.

3.4.3 Spatial and temporal discretization

The gradient discretization was set to Green-Gauss node-based. The PRESTO! scheme is employed. The discretized momentum equation was solved with the second order upwind scheme. For the free-surface, the volume fraction was set to 'geo-reconstruc' (explained in section 2.5). It is recommended in the code manual FLUENT (2009*b*) to use the bounded second order upwind based discretization scheme for the mean flow, turbulence and transition equations. Turbulent kinetic energy, specific dissipation rate, intermittency and momentum thickness Reynolds number were all set to second order upwind.

The first order implicit transient formulation was used, however, this is for the time step only.

3.4.4 Solution controls

Sarkar and Vassalos (2000) set the under-relaxation factor for pressure to 0.3. The upward differencing scheme with an under-relaxation factor of 0.9 was set for momentum. Because the pressure under-relaxation factor was set to 0.3 for this case the momentum under-relaxation was set to 0.7. The sum of the momentum and pressure factors is 1.0. This is recommended (FLUENT, 2009*b*) if only the skewness correction is used in the PISO scheme.

If the skewness and neighbour correction schemes are used, all under-relaxation factors could be set to 1.0. Setting the under-relaxation factors was a trial and error process. The simulation was initially run with the factors all set at 0.9. The values were then reduced according to convergence stability and iteration number. Slow smooth convergence may indicate that the under-relaxation value is too low. A non-smooth convergence or divergent curve indicates that the relaxation factor for that equation is too high. Density, body forces, intermittency, momentum thickness and Reynolds number were set to 0.8. Turbulent kinetic energy and turbulent viscosity was set to 0.7 and specific dissipation rate was set to 0.5. It was not possible to carry

out this type of under-relaxation adjustment on every case. The convergence for all cases were satisfactory.

3.4.5 Solution initialisation

Initial values of turbulence kinetic energy (k) and specific turbulence kinetic energy dissipation rate (ω) are beneficial for convergence when reasonable initial guesses are made. The calculation, however, becomes independent of these initial conditions once a sufficiently large time has elapsed and the solution converges. Initial values can be set for gauge pressure, x-velocity, y-velocity turbulence kinetic energy, specific turbulence dissipation rate, intermittency, momentum thickness Reynolds number and water volume fraction. The first two time steps of each simulation were, however, set up as laminar flow cases to obtain initial velocities for the turbulence models (this improved convergence). FLUENT (2009) uses these velocities to determine turbulent fluid properties in the flow field. Specifying initial turbulent fluid properties is thus not necessary. All initial values for the laminar flow cases (x-velocity, y-velocity, gauge pressure) were set to 0. Because two interacting fluids were considered, the regions containing the different fluids had to be specified. A rectangular region (hexahedron in three-dimensions and a quadrilateral in two-dimensions) containing the water (secondary fluid) was marked. The region spans from -7 m to 7 m in the x-direction and -2.25 m to 0 m in the y-direction. The region was marked beyond the computational domain as to ensure that the water reaches the boundaries. Regions outside of the computational domain are ignored by FLUENT (2009). The marked cells were patched with water, meaning a multi-phase value of 1 was assigned to these cells.

3.4.6 Monitors and calculations

Monitoring the residuals of the calculation is the best way to monitor numerical solution convergence of the discretized differential equations for this transient case. The residual sum of conserved variables is computed after every calculation iteration. Consider a fluid flow property ϕ at cell i . The discretized conservation equation for this variable may be presented by:

$$a_i\phi_i = \sum_{nb} a_{nb}\phi_{nb} + b \quad (3.4.1)$$

The residual (R^ϕ) is computed by summing the imbalance of equation (3.4.1). Scaling the residual with the flow rate of ϕ through the domain produces a qualitative result for judging convergence. Consider the scaled residual definition:

$$R^\phi = \frac{\sum_{cells} i |\sum_{nb} a_{nb}\phi_{nb} + b - a_i\phi_i|}{\sum_{cells} i |a_i\phi_i|} \quad (3.4.2)$$

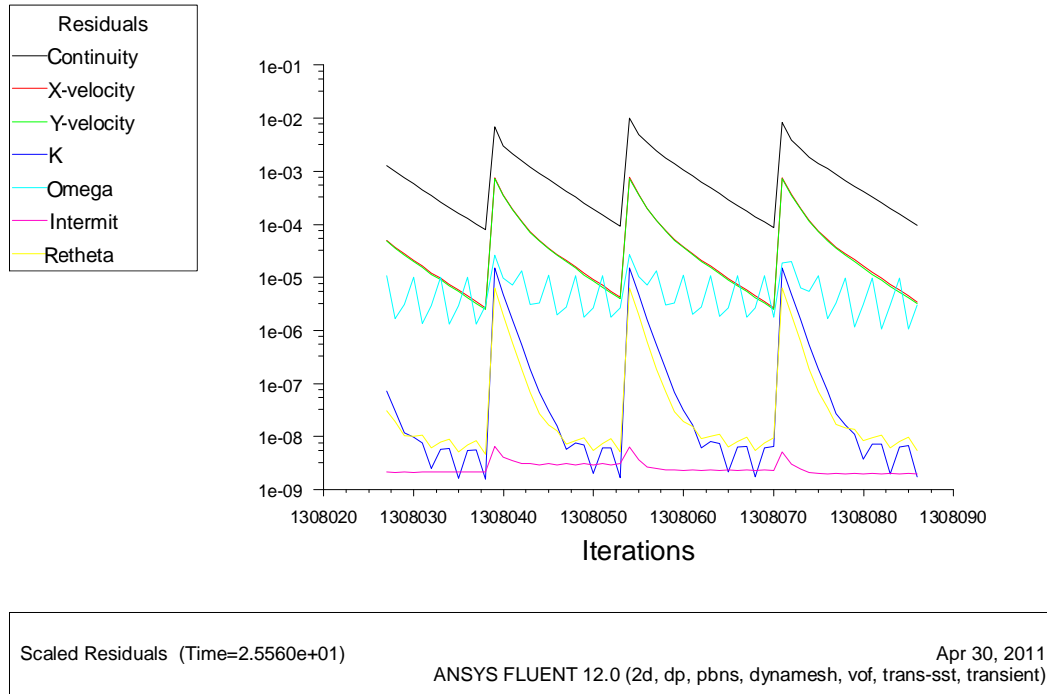


Figure 3.6: Last 60 iterations for a rolling flat-bottom hull, with the SST transition turbulence model

The residuals for the initial laminar calculation were set to 1×10^{-16} for continuity, x-velocity and y-velocity. Once the two-time-step laminar simulation was complete and the turbulence model implemented, continuity, x-velocity, y-velocity, turbulence kinetic energy, specific turbulence dissipation rate, intermittency and momentum thickness Reynolds number residuals were all set to 1×10^{-4} . Considering computational time, the accuracy is sufficient and the residuals reach the limit (figure 3.6)

Monitors were set up for measuring drag, lift and moment. The definition of drag is a force that opposes the relative motion of a body through a fluid. The so-called drag coefficient measured by FLUENT (2009) does not follow this definition and measures this coefficient only in one direction. This leads to negative drag being measured, indicating the direction in which the hull is moving.

Pressure and viscous forces acting on the whole surface of the oscillating hull are calculated by FLUENT (2009). To determine the total force exerted on a hull the force from every cell face adjacent to the hull is summed. The total force acting in a specific direction is calculated (per time step in this case) with:

$$\underbrace{F_a}_{\text{total force}} = \underbrace{\vec{a} \cdot \vec{F}_p}_{\text{pressure force}} + \underbrace{\vec{a} \cdot \vec{F}_v}_{\text{viscous force}} \quad (3.4.3)$$

FLUENT (2009) produces values for the force coefficients. These coefficients

are defined by dividing the total force by $\frac{1}{2}\rho v^2 A$. ρ, v and A are assigned reference values described in subsection 3.4.1. For the purposes of this study the coefficient values were multiplied by the reference values. A point about which the moment is calculated was defined as the axis of rotation (roll axis point A). The products of the pressure and viscous force vectors with the moment vector \vec{r}_{AB} for each cell face (at point B) adjacent to the hull are summed up. Consider:

$$\underbrace{M_A}_{\text{total moment}} = \underbrace{\vec{r}_{AB} \times \vec{F}_p}_{\text{pressure moment}} + \underbrace{\vec{r}_{AB} \times \vec{F}_v}_{\text{viscous moment}} \quad (3.4.4)$$

The right hand rule for cross products is used. As with drag and lift a moment coefficient is calculated, the total moment is divided by $\frac{1}{2}\rho v^2 AL$. L is also defined in subsection 3.4.1. The drag, lift and roll monitors were set up with the FLUENT (2009) monitors setup. All the wall zones (surfaces) making up a hull were included for the measurements. (The square-bottom hull for example consisted of the 'hull_bottom', 'hull_port', 'hull_sb' and 'hull_top' zones). The data was written to a text file for analysis purposes.

Secondary monitors included y^+ surface monitors along the hull surface. The cell face (which would be one cell edge for the two-dimensional case) average and face maximum of y^+ along the hull surface was measured. The face average method simply sums up the face values of the selected variable and divides it by the total number of faces. The face average is defined by:

$$\frac{\sum_{i=1}^n \phi_i}{n} \quad (3.4.5)$$

ϕ_i is the flow property at facet i and n is the number of facet. ϕ_i can for example be replaced by y^+ . The face maximum is the maximum value of a flow/field variable ϕ_i on the edge of a cell (in the two-dimensional case).

The SST transition model require low y^+ values to accurately capture laminar and transitional boundary layers. A value of approximately one is desirable. If larger y^+ values exist ($y^+ > 5$) the location of transition to turbulence onset moves upstream with increasing y^+ . This condition was not met for the all cases. Despite this fact, the results were not very sensitive to increasing y^+ values. This is further discussed in section 5.2. The tabulated y^+ values may be found in appendix A.

3.4.7 Time step

Quérard *et al.* (2009) chose a time step to assure a global average Courant number (explained below) of 1.0 for the whole simulation. An adaptive time stepping was used to achieve this. They found that for the roll case the time step size influenced the hydrodynamic coefficients noticeably. Wilson *et al.*

(2006) employed Menter's blended $k-\varepsilon$ two equation model. For the medium speed case of their simulations, the time step was chosen to produce y^+ values of 0.9.

The time stepping formulation in this study is first-order implicit. No stability criterion need be met for this formulation. It is recommended that Δt is at least one order of magnitude smaller than the smallest time constant in the system being modelled (i.e. the time used for VOF calculations or for the dynamic mesh). According to FLUENT (2009b), the ideal number of iterations per time step is said to be between 5 and 10. This number ensures the computational time is kept low. If the number of iterations exceed this limit, it is suggested that the time step be decreased. If these guidelines are used and convergence is rapid, an investigation into the time dependence of the problem may not be necessary.

A guideline for choosing a transient time step for the VOF method may be found in FLUENT (2007). Consider:

$$\Delta t = \frac{V_{cell,min}^{1/3}}{U} \quad (3.4.6)$$

The case with the largest fluid velocity is tested to meet this requirement. The case of the rolling triangle is where Δt may achieve a minimum value. From this calculation (see appendix A):

$$\Delta t = 0.007825s$$

The largest time step in any of the calculations is 0.0013286 s which is well below the required time step size (almost an order of magnitude). The time step will also produce a Courant number below 0.25. If convergence is not achieved the time step should be decreased to a 10th of the calculated time. Convergence within 10-15 iterations is desirable. A fixed time step assuring convergence of the discretized equations within 15 iterations per time step was used for each case.

For the heave and sway flow cases 15 complete displacement oscillations of the hulls were carried out. 20 oscillations were completed for the roll case. 63000 and 84000 time steps were implemented for the heave and sway, and roll cases respectively. Fixed time steps were specified, as tabulated in table 3.4.

The iteration limit was set to 20.

Table 3.4: Simulation oscillation frequencies and time steps

ω	Period [s]	Time step [s]	Flow time [s]		
			Heave	Sway	Roll
1.129	5.5653	0.001329	83.727	83.727	111.3702
3.023	2.0785	0.000496	31.248	31.248	41.5747
4.917	1.2778	0.000305	19.215	19.215	25.559
6.811	0.9225	0.000220	13.86	13.86	18.4514
8.705	0.7218	0.000172	10.836	10.836	14.44
10.599	0.5928	0.000142	8.946	8.946	11.8996

Chapter 4

Computational Mesh

Discretizing the computational domain is done using the grid generation software GAMBIT (2004). Triangles and quadrilaterals are most often used for two-dimensional problems. Unstructured grids are useful for concentrating a mesh where required (Versteeg and Malalasekera, 2007). A combination of cell shapes can be used to describe complex geometries. Cell combinations were used to generate a so-called hybrid mesh around the hulls investigated. The size of the computational domain was determined by methods discussed in subsection 3.2.2. All the meshes are geometrically symmetrical about the centreline of the hull under consideration (see figures 4.1 and 4.2).

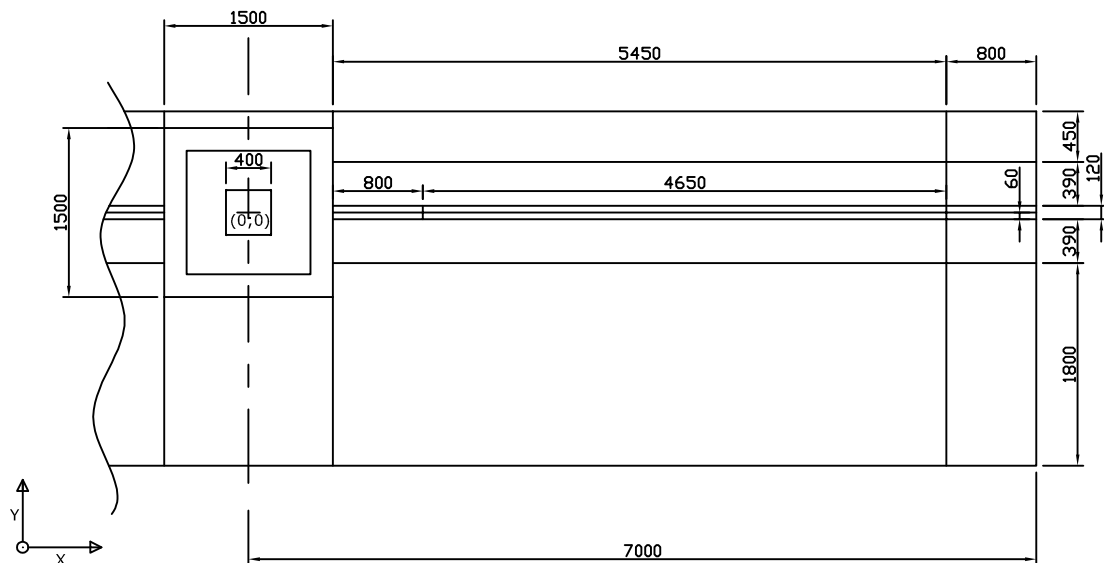


Figure 4.1: Schematic (scale: 1:66.67) of the computational domain

4.1 Meshes Used in Literature

Bangun *et al.* (2010) discretized their computational domain with an unstructured grid using triangular control volumes (CV). The mesh was locally refined where sudden changes in particular flow variables (velocity, pressure) occurred. These sudden changes or steep gradients commonly indicate a specific flow phenomenon such as a point of separation or a vortex. With this approach the aim was to limit the number of cells by coarsening the outer flow field region (outside the areas of interest) along with local refinement. Colocated cell based variable arrangement is used for each CV. The reason for implementing this is that handling intersection points of two boundaries become easier. This is particularly useful for the free-surface boundary condition. The grid is dynamic because of the presence of a free-surface. The positions of the control points of the free-surface are determined by moving the cell vertices vertically. This vertical movement is carried out to enforce a zero net mass flux at every free-surface cell. This satisfies the kinematic boundary condition. A computational domain size of 0.5 m by 10 m with a hull 0.5 m in width with 0.05 m and 0.075 m drafts were considered.

A rolling cylinder lends itself to implementing sliding meshes. Sarkar and Vassalos (2000) used a grid consisting of a moving zone and a stationary zone. The moving zone lies within a circle with radius 0.8 m and origin at the centre of the hull roll axis. This zone was fixed with respect to the rolling cylinder and rotated inside the stationary zone. The moving zone was refined close to the body. Grid independence was achieved by refining the region near the body and the free-surface. A total of 8000 cells were used with 684 for the outer region. The computational domain size was approximately 7.77×2.4 m in size with a hull of 0.34×0.34 m (dimensions are scaled off the article's diagram). An unstructured grid was used.

Chen and Liu (2002) conducted a study on an actual sized hull with a length of 57.3 m, a draft of 3.58 m. A $61 \times 51 \times 21$ m three-dimensional rectangular grid was constructed around this hull. The ship rolls with respect to this grid. At each time step the grid was regenerated to conform to the submerged hull geometry and free-surface elevation.

The geometry of a physical model representing a modern full-scale naval combatant was numerically investigated by Wilson *et al.* (2006). The hull length is 3.048 m with a beam of 0.386 m and draft of 0.214 m. The grid consisted of a hyperbolically generated near-hull grid to resolve the turbulent boundary layer. An algebraic far-field grid between the near-hull grid and far-field boundary was created. The grid totalled to 728 000 grid nodes. Near wall grid spacing was 4.0×10^{-6} m.

Often y^+ values are considered to determine the size of the near wall grid. y^+ is the distance of the first node from the surface in non-dimensional wall units. y^+ values are often required to validate turbulence models.

For the FPSO hull investigated by Kinnas *et al.* (2006) a quadrilateral

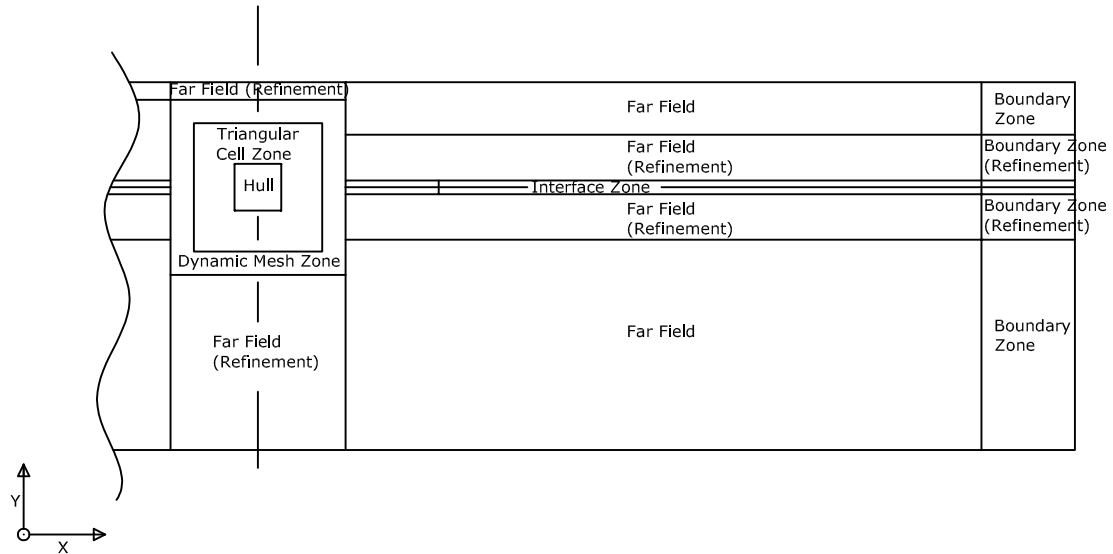


Figure 4.2: Schematic (scale: 1:64.22) of the computational domain block zones

celled mesh was used. A boundary layer mesh was placed along the hull surface. The grids near the hull moved along with the body. Because of this grid movement, additional terms were taken into account to calculate the time derivative term. For the second part of their investigation using FLUENT (2009), Reynolds stress model with standard wall functions was applied. y^+ values of 40 in the turbulent case were obtained.

Quérard *et al.* (2009) constructed a mesh consisting of approximately 32 000 cells. Even though this was a two-dimensional investigation, three-dimensional grids were constructed with only one layer of cells on the third dimension. The meshes were designed by considering the following:

- An average periodic y^+ value < 10 was required.
- The cell aspect ratio below 7 in the free-surface region had to be achieved.
- The cell height near the free-surface was $1/40$ of the mean draft of the section.

For the circular cylinder, the grid consisted of 33 423 hexahedrons structured in 20 blocks. The grid for the rectangular cylinder consisted of 32 268 hexahedrons also structured in 20 blocks. 10 blocks were used to increase the mesh density in the near-body vicinity and totalled to 3 744 hexahedrons. A hybrid mesh consisting of 15 840 hexahedrons, used to further refine the near-body vicinity, was created. A structured grid was created close to the body and the free-surface regions, the remainder of the domain was meshed with unstructured prisms. Even though the number of cells in the boundary layer and around the sharp corners were increased, the total number of cells were kept to 34 011.

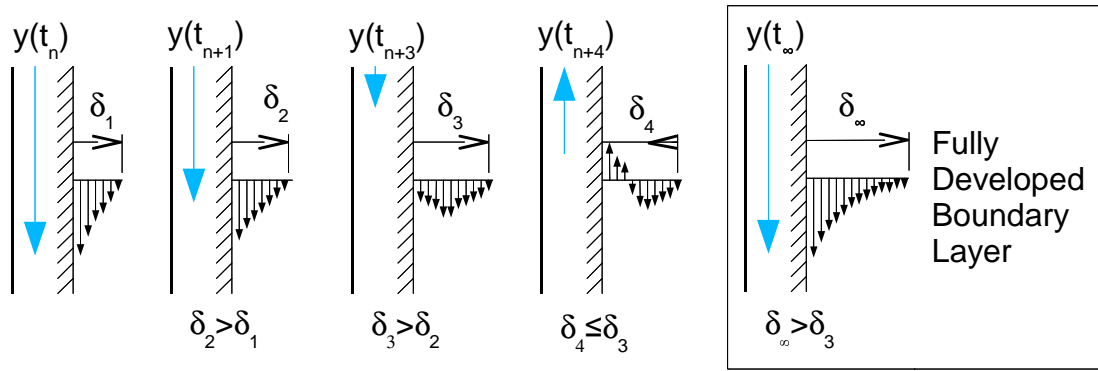


Figure 4.3: Schematic (not to scale) of the expected flow near the boundary wall (hull)

4.2 Mesh Requirements

4.2.1 Introduction

The important flow characteristics of the fluid flow problem examined in this thesis occur near the hull surface. Regions around geometric complexities (for example corners) are of interest. Also, requirements such as close wall grid fineness, close wall grid thickness and free-surface grid fineness for the transition and volume of fluid models were considered.

The determination of the fineness and thickness of the mesh region surrounding the hull (figure 4.4) is difficult. The complexity added to this flow case by geometry and its time dependence is considerable. The law of the wall is not valid because of adverse pressure gradients along the wall. The boundary layer also does not have sufficient time to develop because the hull oscillates returning to its initial position at every cycle (figure 4.3). This produces alternating positive and negative flow velocities along the wall in the direction of a chosen axis parallel to the hull motion. Also the flow is rarely parallel to the boundary wall. It is because of these complications that the $k-\omega$ model is required for near wall treatment and low Reynolds number flow. Such models are solved numerically.

It was desirable to obtain an indication of the scale of the mesh required near the oscillating hull. Numerous assumptions provide the opportunity to implement simple flat plate theory in a conservative manner to obtain the required information. These assumptions may be valid in local regions but will certainly not be applicable to the entire hull surface.

It must be stressed that these assumptions and calculations are not expected to guarantee the creation of an ideal or even accurate mesh meeting all the transition SST flow requirements. A discussion of the comparison between what was expected and the actual numerical results may be found in chapter 6 subsection 6.1.1.

4.2.2 Close wall grid fineness

Regarding the transition SST model that was employed, a y^+ plus value of < 5 is required at the hull surface.

$$y^+ = \frac{\rho u_\tau y_\omega}{\nu} \quad (4.2.1)$$

The so-called friction velocity u_τ is defined by $u_\tau = \sqrt{\tau_w/\rho}$. From equation (4.2.1) it is clear that y^+ is directly proportional to u_τ . Also, u_τ is proportional to the free-stream velocity U . U is dependent on the motion prescribed by the oscillating hull. Because the hull motion changes direction, U will also assume a negative value. For this reason the maximum value that U will reach (considering all cases) is used for determining the value of the first grid node distance y . Assuming a linear sub-layer, y^+ values were calculated. For this case $u^+ = y^+$. Where:

$$u^+ = \frac{U_e}{u_\tau} \quad (4.2.2)$$

For flow perpendicular to the boundary U_e is defined by Falkner and Skan (1930), as:

$$U_e = Cx^a \quad (4.2.3)$$

$a = 1$ for stagnation boundary layer flow. The free-stream velocity is taken as the maximum local velocity of the surface of a hull. The v-bottom hull in roll yields a maximum tip speed of 0.636 m/s. The local velocities near the hull edges are difficult to estimate. For this reason the flat plate flow velocity will also be taken to be this maximum tip speed velocity. It is not possible to accurately determine the boundary layer mesh thickness without knowing the final numerical results. Flat plate flow and stagnation point flow may be present in the heave and sway cases, its (applicability to roll is unknown). The boundary layer momentum thickness Reynolds number ($Re_{\delta^{**}}$) for flow over a flat plate is used to locate the point of instability. The point of separation is determined with Thwaites' momentum integral relation λ (defined by equation (4.2.4)). Separation may be assumed to occur at $\lambda = -0.09$. The conditions for the points of instability and separation are presented in table 4.1.

Table 4.1: Instability and separation conditions

Flow condition	Stability $Re_{\delta^{**}}$	Transition (λ)
Flow parallel to flat plate	201	-0.09
Flow normal to flat plate	5636	-0.09

λ is defined by:

$$\lambda = \frac{(\delta^{**})^2}{\nu} \frac{dU_e}{dx} \quad (4.2.4)$$

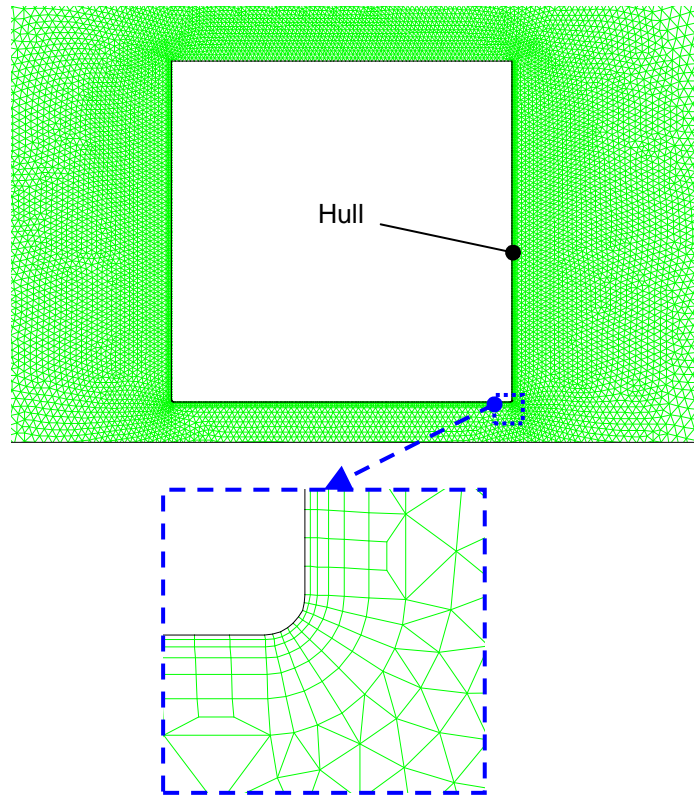


Figure 4.4: Schematic (scale: 1:8.89) of the boundary layer grid

Determining the y value required for the mesh, the equation for the vorticity Reynolds number (Re_v) is used:

$$Re_v = \frac{\rho y^2}{\mu} \frac{\partial u}{\partial y} \quad (4.2.5)$$

For a Blasius boundary layer (laminar flow), Menter *et al.* (2006) related the vorticity Reynolds number and the momentum thickness Reynolds number by:

$$Re_{\delta^{**}} = \frac{Re_v \max}{C} \quad (4.2.6)$$

The constant C is assigned a value of 2.193 by Menter *et al.* (2006). For transition, FLUENT (2009) uses a value of 3.235 for C . FLUENT (2009*b*) claims that this modification improves the prediction of separated flow transition. The shape factor ($H(\lambda)$) at the point of transition is 3.5 where $\lambda = -0.09$.

Momentum thickness Reynolds numbers for the transition flow conditions are presented in table 4.2. The values for the transition flow case must be determined using the relation between λ and $Re_{\delta^{**}}$. From Menter *et al.* (2006), the empirical correlation is defined by:

$$Re_{\delta^{**}} = 803.73[I + 0.6067]^{-1.027} F(\lambda) \quad (4.2.7)$$

$$F(\lambda) = 1 - [-10.32\lambda - 89.47\lambda^2 - 265.51\lambda^3]e^{[-I/3.0]}, \quad \lambda \leq 0 \quad (4.2.8)$$

Free-stream turbulence (I) values of 0 and 0.03 were substituted to illustrate the sensitivity of this model to free-stream turbulence. The turbulence I is taken as a fraction, not a percentage. The results are tabulated in table 4.2.

Table 4.2: $Re_{\delta^{**}}$ numbers for transition

Free-stream turbulence (I)	Transition ($Re_{\delta^{**}}$)
0	805.54
0.03	771.68

The final values for Re_v are tabulated in table 4.3.

Table 4.3: $Re_{v, max}$ numbers for instability and transition

Flow condition	Stability (Re_v)	Turbulence (I)	Transition(Re_v)
Parallel to flat plate	441	0	2606
		0.03	2496
Normal to flat plate	12360	0	2606
		0.03	2496

$u^+ = y^+$ where $y^+ < 5$ (approximately), this region is known as the linear or viscous sub-layer. Consider equation (4.2.2) and equation (4.2.5). Making τ_w the subject of the formula in both cases:

$$\tau_w = \rho \left(\frac{U_e}{u^+} \right)^2 \quad (4.2.9)$$

And,

$$\tau_w = \frac{Re_v \mu^2}{\rho y^2} \quad (4.2.10)$$

Equating (4.2.2) to (4.2.10) and making y the subject of the formula yields:

$$y = \frac{\nu u^+}{U_e} \sqrt{Re_v} \quad (4.2.11)$$

Setting $U = 0.636$ m/s as calculated for subsection 3.4.7. The results are presented in table 4.4.

The distance from the hull wall to the first node perpendicular to the wall was 0.3 mm. A distance of 0.4 mm and 1.3 mm was implemented for only two cases . This is discussed in chapter 6.

Table 4.4: Distance y of the first grid node from the hull surface, required to capture instability and transition

Flow Condition	Stability (y) [mm]	Turbulence (Tu)	Transition (y) [mm]
Parallel to flat plate	0.166	0 %	0.403
		3 %	0.395
Normal to flat plate	0.878	0 %	0.403
		3 %	0.395

4.2.3 Close wall grid thickness

As mentioned in subsection 4.2.1, boundary layer theory is merely used as a guide to determine the type of grid required near the hull surface. The flow along the hull wall boundary is expected not to become fully developed (figure 4.3). The change in wall velocity does not allow sufficient time for the outer region of fluid to be affected by the shear force of the hull. This leads to a shear affected fluid region thinner than a fully developed boundary layer.

It must be stressed that flat plate boundary layer theory was used only as a guide to determining the scale required for the fine grid near the hull. Assuming a fully developed boundary layer the thickness of this boundary layer at the points of instability and transition were calculated.

Using Blasius solution for an infinitely long flat plate downstream of the leading edge.

$$\frac{\delta}{x} \approx \frac{4.9}{\sqrt{Re_x}} \quad (4.2.12)$$

For the momentum thickness:

$$\frac{\delta^{**}}{x} \approx \frac{0.664}{\sqrt{Re_x}} \quad (4.2.13)$$

Making x the subject of the formula of equations (4.2.12) and (4.2.13) and equating the two yields:

$$\delta = \frac{4.9\delta^{**}}{0.664} \quad (4.2.14)$$

δ^{**} may be extracted from Re_δ^{**} through:

$$\delta^{**} = \frac{Re_\delta^{**}\nu}{U} \quad (4.2.15)$$

Table 4.5 gives a summary of the values of Re_δ^{**} along with the corresponding values of δ .

The so-called boundary layer grid is considerably finer than the surrounding grid. A sudden size difference in the grid is undesirable and usually results in poor or inadequate grid construction. If the boundary layer flow can be captured before this transition, accuracy is not compromised. The actual properties of the boundary layer grids used are summarised in tables 4.6 and

Table 4.5: Momentum thickness Reynolds number ($Re_{\delta^{**}}$) and corresponding boundary layer thickness (δ) for instability and transition

Flow condition	Instability		Transition		
	$Re_{\delta^{**}}$	δ [mm]	Tu [%]	$Re_{\delta^{**}}$	δ [mm]
Parallel to flat plate	201	2.34	0	805	9.39
			3	772	9.00
Normal to flat plate	5636	65.71	0	805	9.39
			3	772	9.00

4.7. 'No.' is a number assigned to a grid with certain properties. '1st Node' is the distance of the first grid node perpendicular to the hull surface. 'Transition' is the distance from the surface of the hull at which point the grid geometrically transforms from the fine cells near the hull to the larger cell size of the inner cell region. 'Thickness' is the total thickness of the so-called boundary layer grid, including the transition region.

Table 4.6: Properties of the boundary layer grid at the surface of the hulls

No.	Mesh	1st node [mm]	Transition [mm]	Thickness [mm]
1	Coarse	0.6	7.9	12.5
	Medium	0.4	5.3	8.3
	Fine	0.3	4	6.2
2	Coarse	0.6	11.3	19.8
	Medium	0.4	7.6	13.2
	Fine	0.3	5.7	9.9
3	Coarse	0.7	9.7	15.3
	Medium	0.5	6.8	10.7
	Fine	0.3	4.1	6.4
4	Coarse	1.9	20.8	31.2
	Medium	1.3	14.6	21.8
	Fine	0.9	9.7	14.5

The grids used to obtain the numerical results, boundary-layer grids were between 6.2 and 9.9 mm thick. In one case (round-bottom roll) a boundary layer 21.8 mm thick was used. The effects and differences are discussed in chapter 6.

4.2.4 Fluid interface

Capturing the fluid flow near the free-surface is required. Free-surface waves contribute to energy dissipation. The far-boundaries in this case require surface flow variable data to adjust the water surface level at these OCPOB's.

Table 4.7: Boundary layer grids assigned to different simulated cases

Motion	Hull	Mesh no.
Heave	Round-bottom	1
	Flat-bottom	1
	V-bottom	3
Sway	Round-bottom	4
	Flat-bottom	2
	V-bottom	3
Roll	Round-bottom	4
	Flat-bottom	1
	V-bottom	3

For these reasons the number of cells in the grid region near the free-surface was increased (figure 4.5). According to FLUENT (2007) the mesh should be smooth and of good quality in this region. Meeting these recommendations usually leads to quick and smooth convergence of the VOF model. Large cell skewness, size variation and high aspect ratio results in poor convergence. At the fluid interface there is a steep fluid density gradient which defines the free-surface. Steep gradient flow properties require fine mesh regions. The free-surface region can be seen in figure 4.5 (with fluids water, red, and air, blue). It was not required to accurately calculate the exact position of the free-surface throughout the simulations because the waves are downstream of the oscillating hull. A coarser grid facilitates the loss of detail in the description of the free-surface and flow variables. This numerical damping reduces the influence of any wave reflection at the boundaries to the remainder of the computational domain.

4.2.5 Boundary

The grid fineness at the outer boundary surface regions is increased. The waves described in this region must pass through the boundary. A fairly accurate description of the free-surface at the far-boundaries is necessary to minimise disturbances (in the form of wave reflection) to the oscillating hull. As mentioned in subsection 4.2.4, numerical damping may reduce wave amplitude requiring a fine grid region to capture these small waves.

4.2.6 Dynamic mesh region

Referring to figure 4.2, the 'dynamic mesh zone' is a square zone surrounding the inner mesh region. The shape of this zone allows for any hull and inner mesh region geometries to be defined without influencing the remainder of the computational domain grid. The flow variables calculated in the dynamic mesh region, which is close to the hull, have the most influence on the forces of the

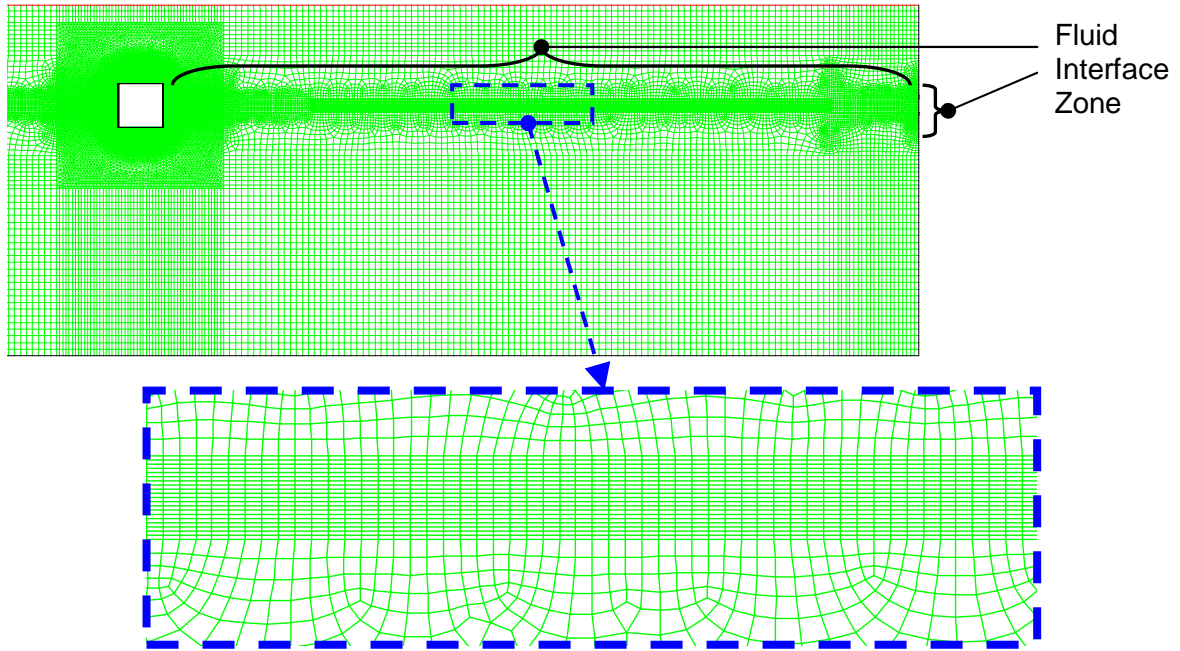


Figure 4.5: Schematic (scale: 1:67.96) of the fluid interface grid zone (and close-up of grid details)

water exerted on the hull. The quality and geometric transition (for example increasing cell size and changing cell shapes) must be smooth in this region. Triangular cells are used in this region to assure smooth and even remeshing.

4.2.7 Inner mesh region

Complex geometries may be difficult to mesh using structured grids. Both unstructured quadrilateral and triangular cells were exploited (figure 4.7). Because the dynamic mesh region consists of triangular cells, the inner mesh region was also meshed with the same shape in most cases. This was done to ensure a smooth mesh geometric transition. Initially structured quadrilateral cells were employed for all cases, but the geometric mesh transition between this region and the dynamic mesh region was too abrupt in most cases. Meshing around the different hull sections was also difficult with this structured cell method.

Triangular cells provide a smooth geometric transition and can be used to mesh complex geometries relatively easy. One disadvantage is that with triangular cells, the number of cells in a region increases compared to quadrilateral cells.

In an example of a mesh for a v-bottom hull in roll, the total number of cells, with quadrilateral cells surrounding the hull, totalled 60 416. This same case with triangular cells around the hull totals to 65 122. This is a 7.8 % increase in the total number of cells in the computational domain.

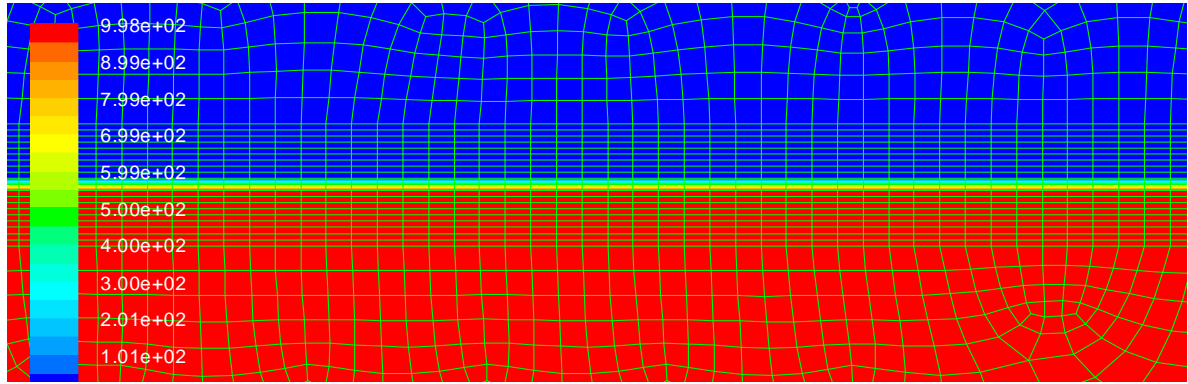


Figure 4.6: Contours of density (kg/m^3) of the fluid interface grid zone (same close-up as in figure 4.5) (scale: 1:7.5)

The outlining shape of the inner mesh region assumes the shape of a square for the heave and sway cases. Cell skewness in the dynamic mesh region of the cells surrounding this region is reduced if in the roll cases, a circular outline shape is used for the inner mesh region.

4.2.8 Far field

In the far field regions the flow variables have smooth gradients (figure 4.8). Fluid velocities are low and pressure is close to hydrostatic. To save computational time mapped (structured) quadrilateral cells were created. This method reduces computational time because of the simple cell geometry and size. Regions between small and large cells were paved with quadrilateral cells to accommodate size transition.

4.3 Mesh Specifications

A total of 27 meshes were created for this investigation. The motion, hull shape and mesh refinement were taken into consideration (see table 4.8).

The details of the seeding of the edges (also for refinement) may be found in appendix D. A grid independence study was carried out and is discussed in section 5.1. Referring to figure 4.2 the 'triangular cell zone', 'dynamic mesh zone' and 'interface zone' were refined. The finest grids were not used in all cases, this is further discussed in section 5.1.

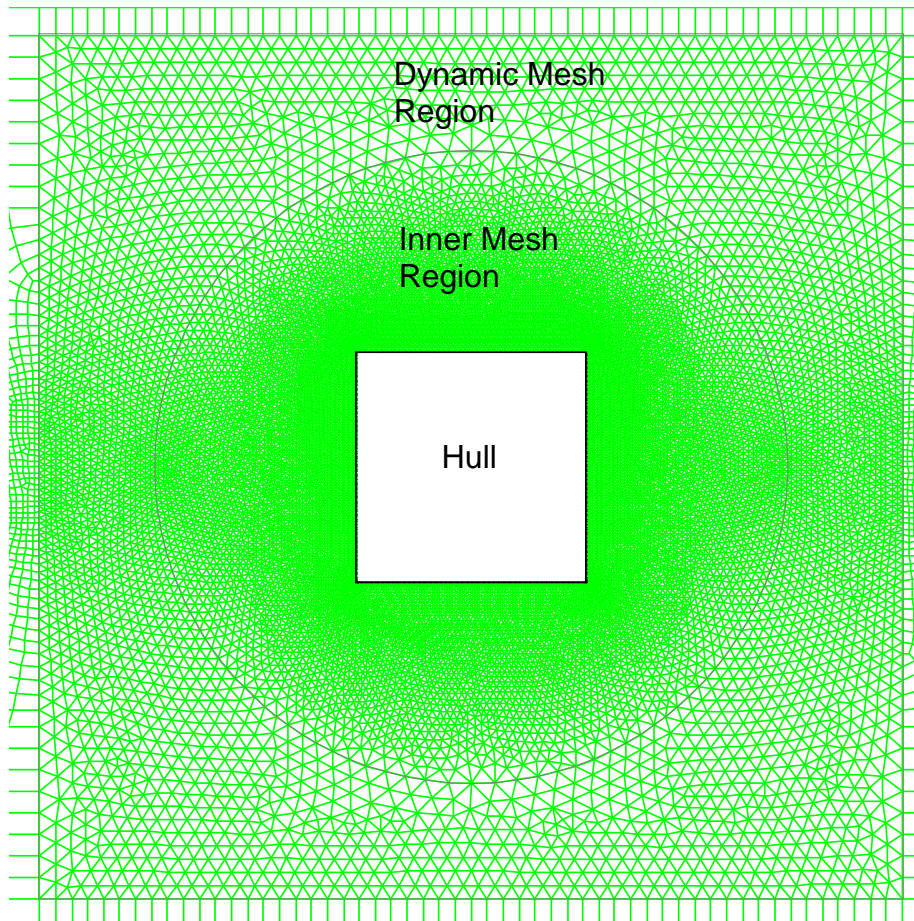


Figure 4.7: Close up of the grid regions around the hull (scale: 1:13.16)

Table 4.8: Mesh specifications

Case	No. of cells			Max. cell skewness			Grid used
	Coarse	Medium	Fine	Coarse	Medium	Fine	
Heave							
V-bottom	10825	18429	31602	0.63	0.79	0.7	Fine
Round-bottom	11689	20547	38199	0.79	0.77	0.77	Fine
Flat-roll	13666	24224	43923	0.76	0.7	0.7	Fine
Sway							
V-bottom	21843	35878	61661	0.89	0.78	0.68	Medium
Round-bottom	21027	36272	62692	0.69	0.76	0.68	Fine
Flat-bottom	23128	40542	70322	0.7	0.82	0.81	Fine
Roll							
V-bottom	21680	34811	60416	0.93	0.79	0.58	Fine
Round-bottom	23205	36076	62116	0.68	0.68	0.68	Medium
Flat-bottom	26044	41438	72204	0.76	0.79	0.78	Medium

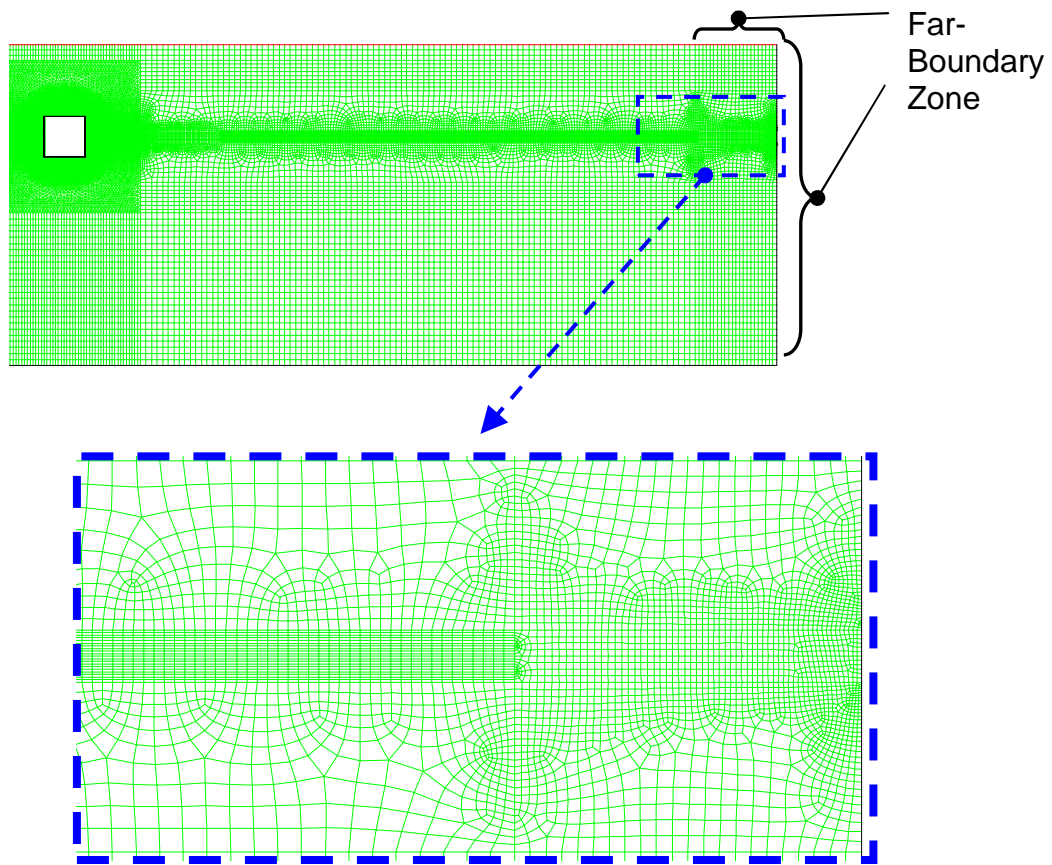


Figure 4.8: Close up of the boundary grid zone (scale: 1:74.47)

Chapter 5

Verification And Validation

5.1 Validation: Grid Independence Study

5.1.1 Introduction

Grid independence is vital in determining whether the set of conservative mass and momentum partial differential equations for the flow field have been solved. The highest hull oscillation frequency ($\omega = 10.599$) was used for the grid independent study. This case is expected to produce the highest flow velocities and flow field variable gradients. It is considered to be a so-called worst case.

A grid independence study method is taken from Versteeg and Malalasekera (2007). Consider the equation for the determination of the error of a flow variable.

$$E_{U,1} = \frac{U_2 - U_1}{1 - r^p} \quad (5.1.1)$$

In this case U is the force, moment or phase angle and r is 0.667. 1 and 2 are the initial and refined mesh numbers respectively. The error for the finer mesh may be calculated with:

$$E_{U,2} = r^p \left(\frac{U_2 - U_1}{1 - r^p} \right) \quad (5.1.2)$$

thus:

$$E_{U,2} = r^p E_{U,1} \quad (5.1.3)$$

The order of the discretization equations (p) may be replaced by a more accurate value \tilde{p} , calculated with:

$$\tilde{p} = \ln \left(\frac{U_3 - U_2}{U_2 - U_1} \right) / \ln(r) \quad (5.1.4)$$

To determine the exact solution value of U , the following equation can be used after some rearrangement:

$$E_U(h) = U_{exact} - U \approx Ch^p \quad (5.1.5)$$

From equations 5.1.1 to 5.1.5, the exact solutions for the force amplitude, moment amplitude and phase angle are determined. The calculated amplitude errors are presented in figures 5.1 to 5.3 as percentages errors of the exact solution. The phase angle cannot be presented in the same way. The points in figures 5.1 to 5.3 labelled as 'Extended' are points determined theoretically using equations 5.1.1 to 5.1.5.

5.1.2 Discussion

Figure 5.1 illustrates a quick convergence of the solution with grid refinement. For the V-bottom hull, only two of the three cases ran successfully. An observer order $\tilde{p} = 1$ was chosen where three refinement meshes were not available, even though second order upwind discretization equations were used for all the cases. From this graph it is clear that one more mesh refinement may have been required for the v-bottom hull case. It must, however, be taken into consideration that $\tilde{p} = 1$ is very conservative. When considering figure 6.6, the overall effect that further mesh refinement would have on the coefficients is negligible.

The flat-bottom hull case displays a smooth convergence curve with mesh refinement (this may be because \tilde{p} could be accurately calculated). Again the effects of the grid refinement on the determined coefficients (figure 6.7) were very small. The error for the round-bottom hull is satisfactorily low to conclude grid independence.

Grid independence is rapidly achieved for the v-bottom hull in sway (figure 5.2). No further grid refinement is required for this case. The flat-bottom hull indicates a slow, almost linear, convergence with mesh refinement. An amplitude error of approximately 1 % was regarded as being satisfactory. Looking at figure 6.10, no difference between the coefficients determined by the different meshes are visible. The final grid for the round-bottom hull case is considered to be sufficiently fine. Similar observations to that of the flat-bottom hull of the effects of the different grids were noted in figure 6.11.

In figure 5.3 the third refinement for the v-bottom hull case is sufficient to accurately model the case. An almost linear error reduction is illustrated because again \tilde{p} was taken to be unity. Figure 6.12 does not indicate any large changes in the coefficient between mesh refinements. Figure 6.12 points to something very interesting regarding the damping coefficient, the final data point in this figure is considerably larger than that of the other two data points for the damping coefficient. This extreme data point is either an outlier or the grid is fine enough to capture all the fluid phenomenon effects. This specific case can be isolated and investigated in detail. For purposes of this grid independent study, this point was treated as an outlier. The validity of this point in future studies should, however, not be regarded as void.

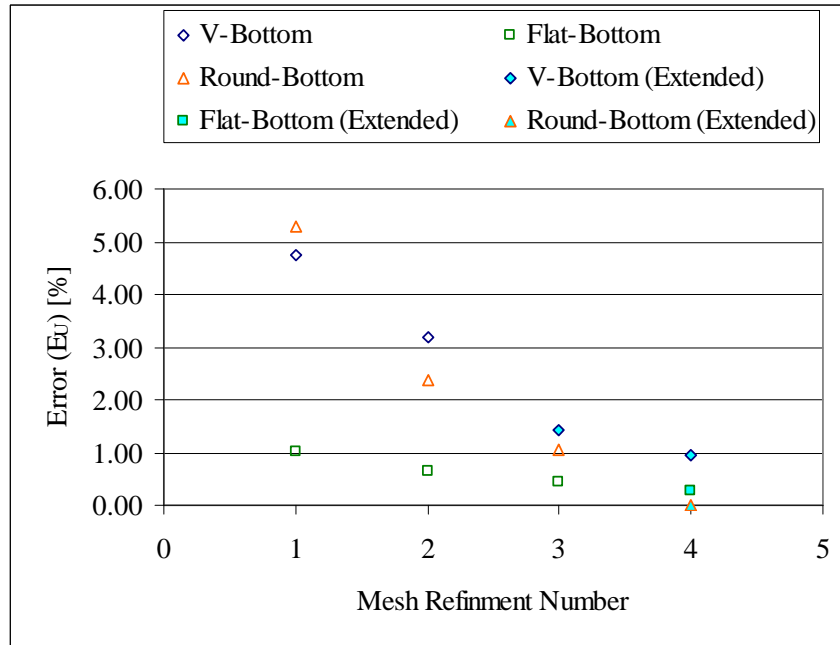


Figure 5.1: Amplitude errors for each hull shape in heave for the highest oscillation frequency

For both the flat-bottom and round-bottom hulls, satisfactory grid independence could not be achieved looking at figure 5.3. Validating these grids required an inspection into the coefficients obtained for these two cases. Figure 6.13 makes it clear that even if the error for the flat-bottom hull were further reduced, the overall effect on the coefficients will not be significant. This indicates that the current numerical model does not fully capture the effects of the flow field on the oscillating hull. Figure 6.14 indicate very little differences between the coefficients determined from the different size grids.

5.1.3 Conclusion

In the heave and sway cases grid independence was successfully achieved. The rolling hull cases may require further mesh refinement to improve the credibility of these results. These specific large roll cases should be further investigated, perhaps case by case because of the flow field complexities involved. Further mesh refinement, however, becomes considerably computationally expensive, and due to time constraints could not be carried out.

Grid independence could not be proven in every case. Considering the effects of the amplitude and phase angle on the overall determination of the mass and damping coefficients, the validity of the overall results is considered satisfactory, however, for the purposes of this project.

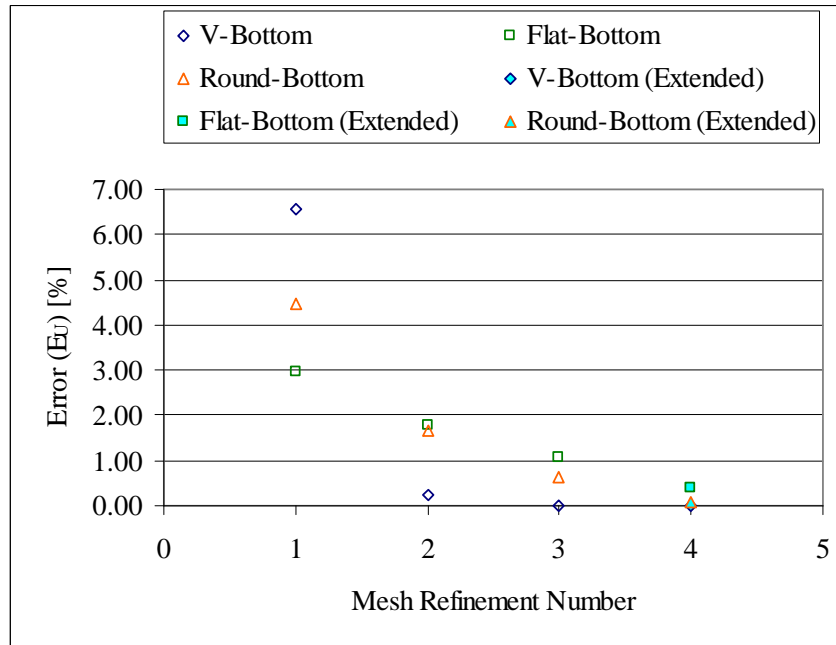


Figure 5.2: Amplitude errors for each hull shape in sway for the highest oscillation frequency

5.2 Validation: y^+ Values

The effects of the y^+ values, larger than the recommended limit of 5 for the selected turbulence model, on the results obtained in this study were investigated. For each simulation, the maximum and mean y^+ values were measured and integrated over the hull regions respectively (as discussed in subsection 6.1.1). These measurements cannot, however, point out where the maximum y^+ values occur. The validity of the measured y^+ values also had to be assessed. The transition SST model makes use of an intermittency equation and the transition onset Reynolds number (Re_{ot}) to predict the onset of turbulence. This is a low Reynolds number model. For the accurate prediction of transition, the y^+ values are required to be well below 5. In this region the a linear sub-layer, where turbulent eddy motions are absent, is assumed. For $30 < y^+ < 500$, the log-law is assumed and the SST turbulence model (Menter, 1992a) is applied. In the case where $5 < y^+ < 30$ (approximately) a blending function is employed (Menter *et al.*, 2006) to deal with the determination of the wall shear stresses used to solve the RANS equations. This means that if the y^+ values are not below 5 near the wall, the results may still be more accurate than for numerical models assuming fully turbulent flow.

The case for a rectangular cylinder rolling with an oscillation frequency of 4.917 rad/s was investigated. The y^+ values at 8 points (figure 5.4) along the hull, as illustrated in figure B.15, were measured for the duration of the simulations. These points are not directly on the hull but a distance of the first

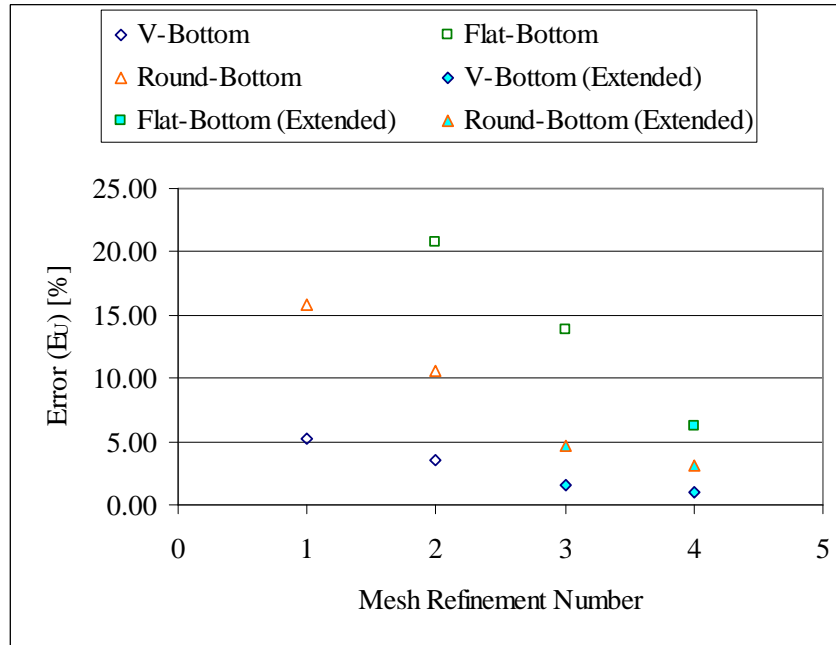


Figure 5.3: Amplitude errors for each hull shape in roll for the highest oscillation frequency

boundary layer grid point from the hull (0.6 mm). Unfortunately these points do not move with the hull, because they are fixed in space. Another method to observe the y^+ values was to plot these values along the hull starboard and bottom surfaces for 9 heel angle positions of the hull (figure 5.5) in the last complete oscillation measured. These results are presented in figures B.1 to B.5.

The measurements made for the 8 points and the hull surface y^+ values are presented in appendix B figure B.15. Referring to this figure, points 5 and 6 are where the maximum y^+ values are measured considering all 8 measuring points. This indicates that at the corners of the hull, the highest y^+ values result from the high local velocities in these regions. Figures B.1 to B.5 agree with this finding and also indicate the local regions where the y^+ values steeply increase. This corresponds with the maximum measured y^+ values presented in appendix C table C.4. These maximum and mean values are, however, not a good indication of the severity of the high y^+ values, because these high values occur locally.

Grid refinement is required around the corner regions of sharp edged hulls. The locality and small presence of the large y^+ values indicate that despite the values not remaining below the recommended limit of 5, the overall effect that this has on the flow field is not extreme. If the limit of 5 is exceeded, the point of transition moves upstream. This point will move into a region where the y^+ is well below 5 where the point of transition will then be determined. This effect is not regarded as severe. A mesh refinement at the corners of the flow

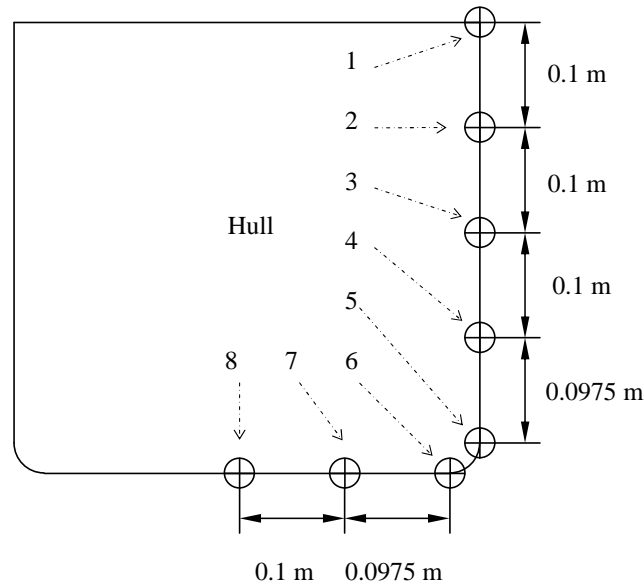


Figure 5.4: Schematic (not to scale) of the flat-bottom hull and eight y^+ measuring points

field is more important for purposes of capturing the flow effects as opposed to obtaining smaller y^+ values.

5.3 Verification: Turbulence Models

Numerous simulations were conducted in order to select the most appropriate turbulence model to be used throughout this project. The case for a rolling rectangular hull (which was regarded as being the most difficult case to model) was chosen as a test case. The hull was oscillated at a frequency of 4.917 rad/s. This oscillation frequency is approximately mid-range between the highest (10.599 rad) and lowest (1.129 rad/s) oscillation frequencies.

Figure 5.6 shows the mass moment of inertia coefficients for the different numerical models available in FLUENT (2009) and applicable to this transient flow case, and compared to the experimental results by Vugts (1968). An inviscid solution was obtained to observe the validity of neglecting viscosity effects. Neglecting viscosity is clearly inappropriate. The RSM model is assumed to be the more accurate model, however, this was the only flow case where the amplitudes fluctuated dramatically between each oscillation. The transition $k - kl - \omega$ model over-predicted the mass coefficient considerably, shortly followed by the $k - \varepsilon$ realizable model. The transition SST and laminar flow models provided the best solutions for this case. This indicated that for this case, turbulence is not strongly present.

In figure 5.7 it is clear that the viscous and inviscid models produce extremely different results. The viscosity is over-predicted by all the viscous

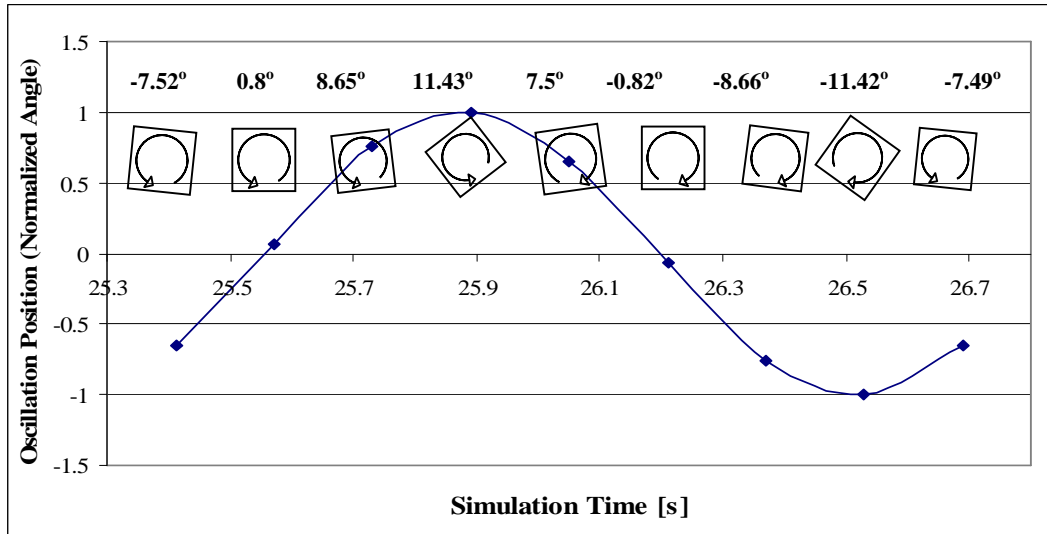


Figure 5.5: Schematic (not to scale) of the flat-bottom hull and eight y^+ measuring points

models. Considering, however, that the laminar flow model and turbulent flow models produce similar coefficient values, the turbulent viscosity predicted by the turbulence models may not be the reason why the damping coefficient is over-predicted. The effects of the major flow phenomenon present (which may be reducing damping for this specific and isolated case) cannot be captured by the two-dimensional numerical models tested and illustrated in figures 5.6 and 5.7.

The transition SST model produced the most satisfactory results and was thus employed on the bases of literature and on the results obtained from this test. Unfortunately extensive testing for every case could not be conducted because of time constraints.

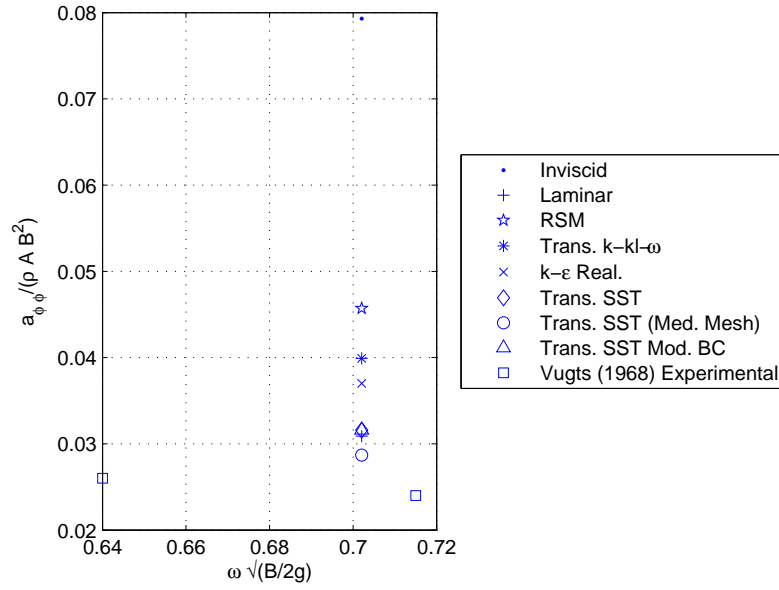


Figure 5.6: Hydrodynamic mass coefficient for a flat-bottom hull oscillating at 4.917 rad/s in roll

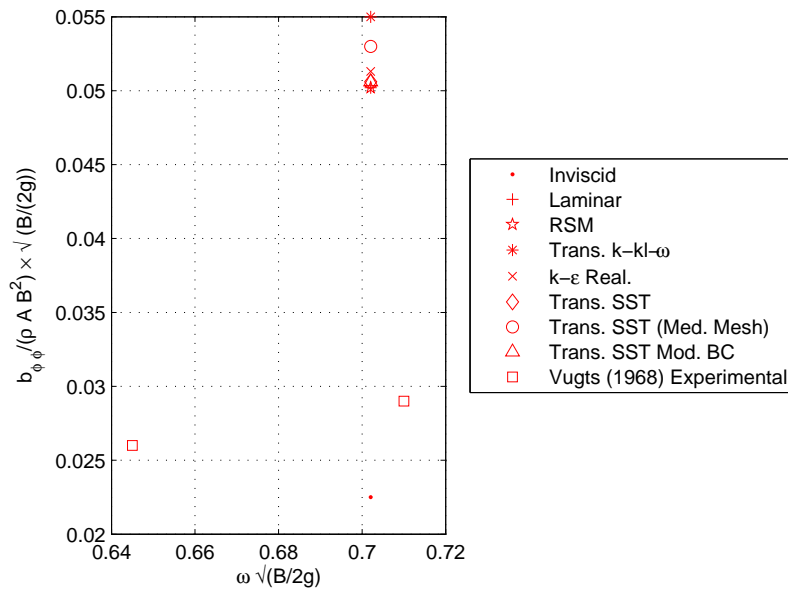


Figure 5.7: Damping coefficient for a flat-bottom hull oscillating at 4.917 rad/s in roll

Chapter 6

Results

6.1 Computational Simulation Results

The total drag, lift and moment experienced by each hull section for each oscillating frequency were determined (as discussed in subsection 3.4.6). The values of flow-time and drag, lift or moment coefficients are written to text files.

Examples of the total force and moment measured for a v-bottom hull section oscillating with a frequency of 6.811 rad/s in heave, sway and roll, are presented in figures 6.1 to 6.3. This data is obtained by multiplying the values in the FLUENT (2009) output files with the appropriate constant reference values (subsection 3.4.1). For the cases presented, measurements were made at every time step of 2.2×10^{-4} s.

Figure 6.1 is a plot of the total vertical force exerted on the vertically oscillating hull with time. The force amplitude of the graph slightly decreases at every oscillation. This was observed for most heave cases. In several cases the amplitude decreases and then slightly increases or fluctuates. The fluctuating amplitudes never increase to the same magnitudes of the first few oscillations. The source of this amplitude decline may be from a physical phenomenon as opposed to a numerical one.

This phenomenon can also be observed in the numerical work of Sarkar and Vassalos (2000), Kinnas *et al.* (2006) and Lin and Kuang (2008). This behaviour is not identified or discussed in literature. The phenomenon is not clear in the experimental work by Yeung *et al.* (1998) but it is present.

This decrease in amplitude may indicate that as the fluid adjacent to the hull becomes excited over time, the fluid next to the excited region also becomes excited extending the excitation further into the flow field. Eventually a very large region of fluid surrounding the hull is set into motion. This motion of the fluid seems to reduce the overall damping effect of the water. It is possible that the moving fluid leads to a reduction in the rate of shear strain ($\partial u/\partial y$) around the hull. The water appears to become less 'stiff' when layers

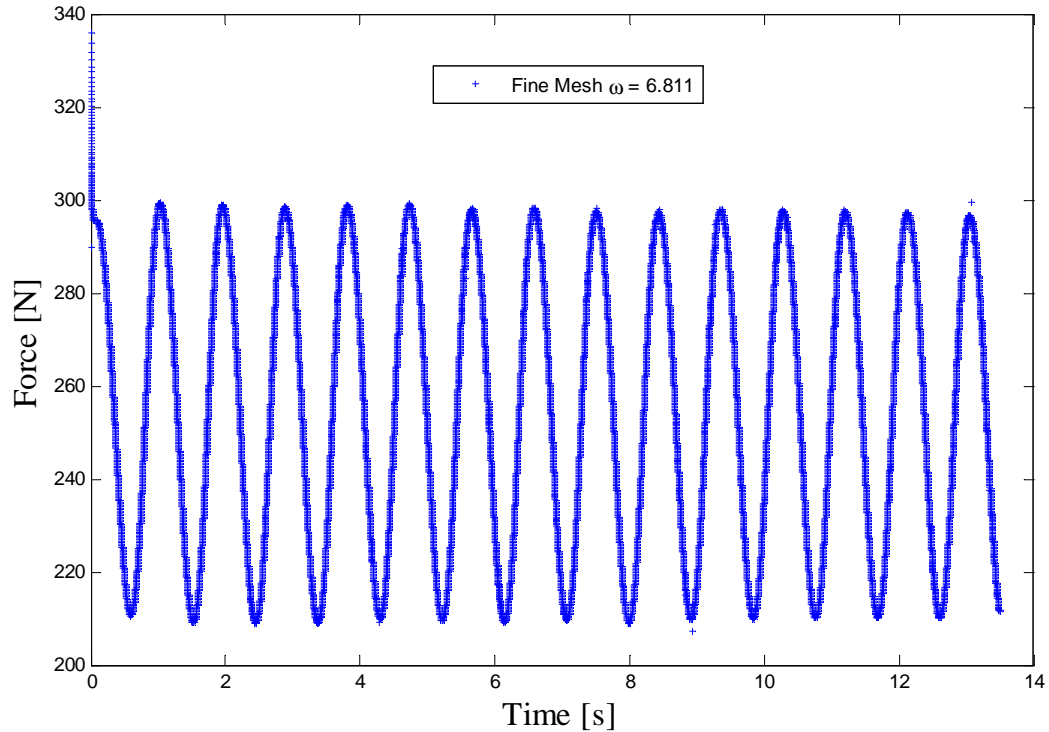


Figure 6.1: Total vertical force experienced by v-bottom hull oscillating at 6.811 rad/s in heave

of this fluid 'slide' over each other.

The amplitude reduction for the sway case over time is much more severe than that of the heave case (figure 6.2). Numerous oscillations are required before a 'near' periodic state is reached. It should be stressed that achieving a perfectly periodic curve is impossible, even with experiments, because the movement of the water is not periodic. Bearing this in mind, simulations were run until the change in force or moment amplitude was below 1 % between crests (or troughs). Typically the number of oscillations required for this to occur for the sway case is 15.

The roll case shows a similar trend to the sway case (figure 6.3). The amplitude reduction is initially severe and continues with time. In this case a mean amplitude is reached in only a few oscillations and the amplitude even increases slightly. This behaviour was not observed in all cases. In general more oscillations were required before the curves reached a periodic state, compared to the sway case. Setting the same force amplitude fluctuating limit as for the sway cases, generally 20 complete oscillations were required. It was observed that the slower a hull oscillates, the longer it takes for the force amplitude to reach a stable mean amplitude.

Wilson *et al.* (2006) found that roll period increases with a decrease in forward speed and damping increases with an increase in speed. The increase

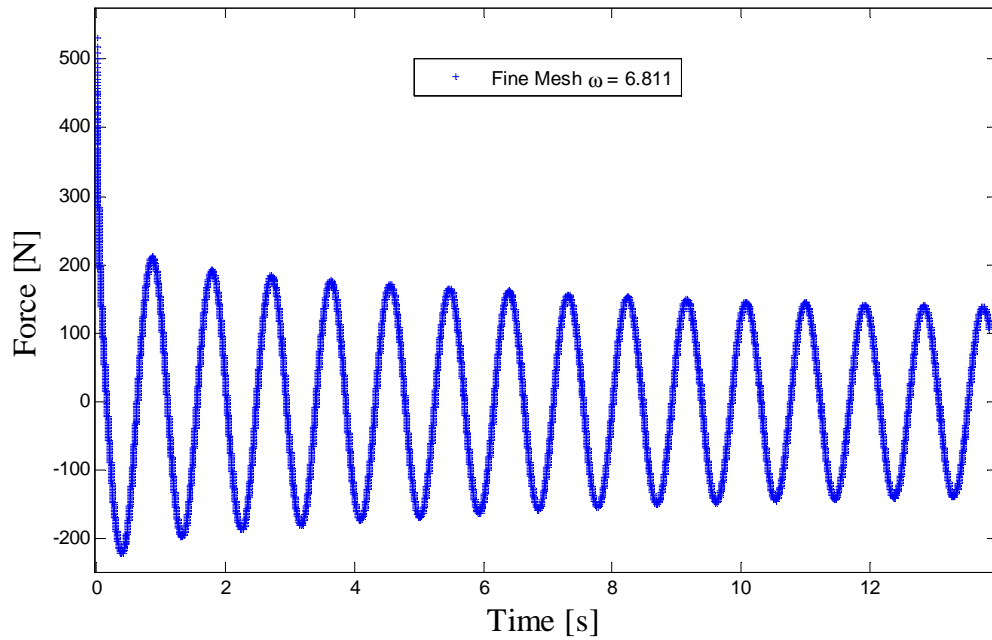


Figure 6.2: Total horizontal force experienced by v-bottom hull oscillating at 6.811 rad/s in sway

in damping may be because as the rolling hull moves forward it enters a new initially still free water surface. Each time the surrounding fluid starts to become excited by the hull, the hull moves to the next region of stationary fluid. Still water is expected to increase the damping on an oscillating hull. A saturation point must also exist where the damping becomes independent of forward velocity, because the fluid surrounding the hull has very little time to become excited. This phenomenon is open to further investigation.

Continuing a simulation for more than 20 cycles is computationally uneconomical. A case for a flat-bottom hull oscillating at 10.588 rad/s in sway is used to illustrate this (figure 6.4. 10.599 rad/s is the highest oscillation frequency used in this study).

The amplitude of each crest was read from the force-time graph (similar to figure 6.2). The amplitude reduction percentages (ARP) of the first to the second and second last to last crest was determined. Thus:

$$Start \% = \frac{A_1 - A_2}{A_1} \quad (6.1.1)$$

$$End \% = \frac{A_{N-1} - A_N}{A_{N-1}} \quad (6.1.2)$$

Where A is the amplitude of the crest and N is the total number of crests under consideration. A constant decrease in ARP was observed in most cases, thus a cumulative reduction approach was implemented. The decrease in ARP

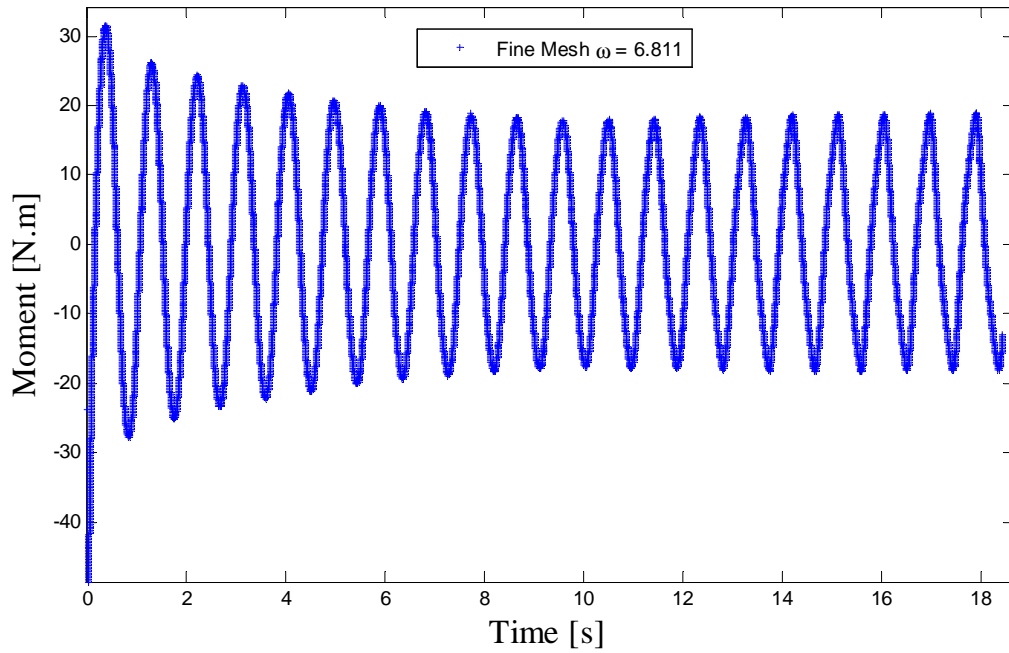


Figure 6.3: Total moment experienced by v-bottom hull oscillating at 6.811 rad/s in roll

is assumed to be constant so that:

$$ARP_n = ARP_{n-1} - \frac{Start \% - End \%}{N} \quad (6.1.3)$$

The force amplitude curve is normalised by dividing all the force amplitudes by the first force amplitude. The curve (figure 6.4) may then be described by:

$$y_n = y_{n-1} - y_{n-1} \times ARP_n \quad (6.1.4)$$

When the ARP_n value drops below 0.25 % the change in amplitude is assumed to be negligible. The oscillation number at this point is the last oscillation number. A computational-time curve is plotted assuming a linear relationship. The total computational time is assigned the value of 1 at the last oscillation number.

In figure 6.4, the dashed line on the graph indicates the point at which the simulations were stopped and the convergence of the force and moment amplitudes achieved. According to the curve 83 % of the total computational time required for an amplitude reduction of 0.25 % was used. This error effect diminishes quickly. It is computationally uneconomical to allow the simulations to continue for longer considering the slight increase in accuracy and the extra time required for this.

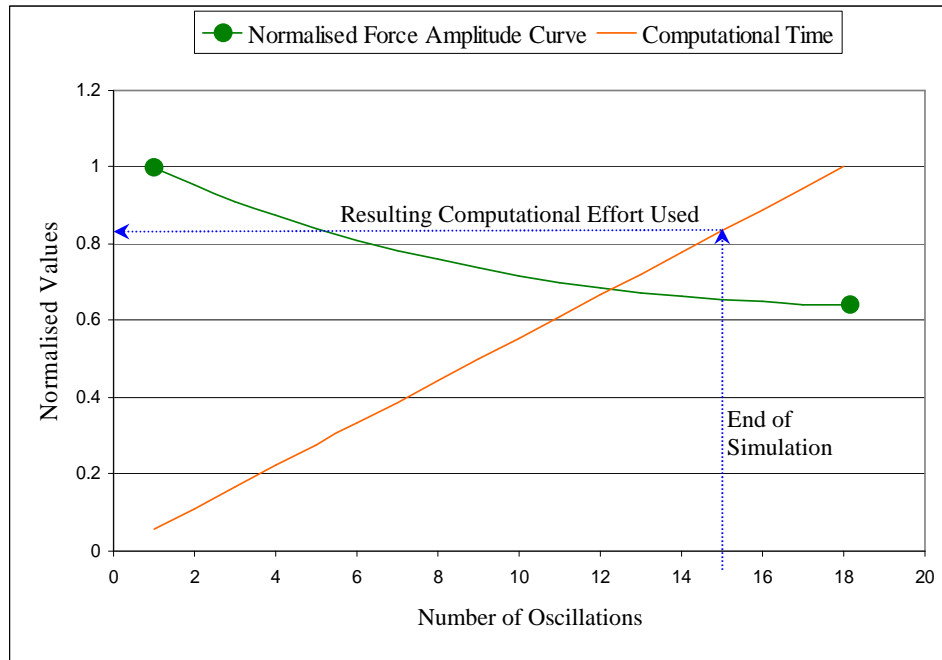


Figure 6.4: Number of oscillations required for a periodic force and moment curves, along with computational time required with normalised y-axis values

6.1.1 y^+ values

The y^+ values measured are tabulated in tables C.2-C.5 appendix C. In all cases the hulls considered were divided up into edge regions (figure 6.5) where the average and maximum values of y^+ for each complete region were monitored. This monitoring method is discussed in subsection 3.4.6. It was desirable to achieve y^+ of 1 or at least below 5 (FLUENT, 2009a) at the first grid node to accurately capture laminar and transitional boundary layers.

A geometrically symmetrical grid was used for the heave case, therefore only half a hull section was considered. Surface y^+ monitors were set up for the starboard and top sides of the triangular hulls. The desired upper limit y^+ values of 5 were achieved for the cases where the hull oscillation frequency (ω) = 1.129 rad/s and ω = 3.023 rad/s.

The flat-bottom hull starboard and bottom sides were monitored. Maximum y^+ values of below 5 were only attained for the ω = 1.129 rad/s case.

Similar to the flat-bottom case, the round-bottom hull starboard and bottom sides were monitored. For ω = 1.129 rad/s and ω = 3.023 rad/s the maximum y^+ values are satisfactory and the ω = 4.917 rad/s case is slightly above the limit of 5.

More simulations were carried out for the sway case than the heave case, because two different displacements were prescribed for the flat-bottom and round-bottom hulls. This was done to maintain consistency in the displacement prescribed to the majority of the hulls (y_a = 0.03 m), and also to simulate

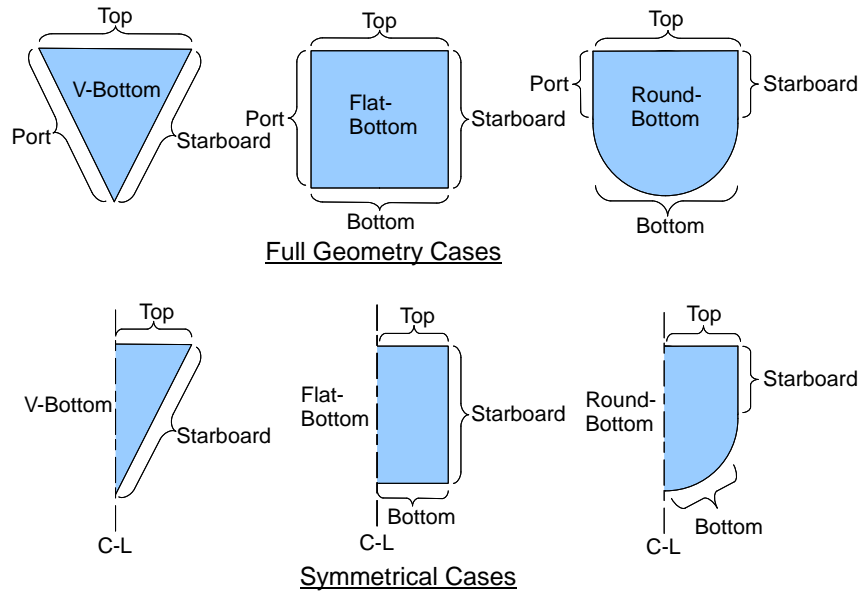


Figure 6.5: Hull surfaces divided into sub-surfaces for monitoring purposes (not to scale)

the same displacement as prescribed by Vugts (1968) for some specific cases ($y_a = 0.02$ m).

In the v-bottom hull case, only the displacement $y_a = 0.03$ m was required. The hull regions consisted of port and starboard sides. In this case none of the maximum y^+ values measured were below 5.

Two prescribed displacement amplitudes were simulated for the flat-bottom hull with port and bottom hull sides. For the larger displacement, only the $\omega = 1.129$ rad/s case produced satisfactory y^+ values. Even though the second prescribed displacement amplitude is 33 % lower than that of the first, again only the $\omega = 1.129$ rad/s case is below the limit. It must be mentioned that the y^+ values did decrease considerably for the smaller displacement. Also, for the $\omega = 3.023$ rad/s case, the maximum values are 5.4 on the port and 6.0 on the bottom sides. The round-bottom hull with monitors on the port and bottom sides yielded the same qualitative results as the flat-bottom case. A complete set of simulations were not conducted for the case concerned with the smaller prescribed displacement.

Considering the roll case, the y^+ values for the v-bottom hulls' edges were monitored collectively to observe whether it is acceptable to consider all the sides collectively or whether the hull sides must be split. In the $\omega = 1.129$ rad/s case a y^+ maximum value of 6.1 was obtained. Both the flat-bottom and round-bottom hull y^+ values were monitored on the port and bottom sides. The flat-bottom hull values for the $\omega = 1.129$ rad/s case achieved maximum values of 5.8 and 5.4 along the bottom and port regions respectively. For the round-bottom hull case maximum y^+ values of 5.7 for the bottom and 5.6 for

the port were measured.

The hull surfaces in contact with water are regions of interest. The hulls were monitored in segments to determine the y^+ values in these regions. The mesh in the air region was coarser compared to the water region. y^+ values were generally larger in the regions in contact with air than regions in sides in contact with water. A single monitor for all the sides collectively would not have been sufficient for checking the maximum y^+ values of the hulls.

The current grids do not maintain y^+ values below 5 for most of the simulation cases.

The dimension estimations from the boundary layer theory are not very conservative. The grid fineness estimations were based on the $\omega = 10.599$ rad/s cases, but the y^+ values achieved for these frequencies are an order of magnitude larger than predicted from an approximation analysis (subsection 4.2.2). This method is, however, useful if it is kept in mind that the boundary layer is not fully developed.

6.2 Data Analysis

The monitors regarding the lift, drag and moment were of primary interest. This data was used to determine the added mass and damping coefficients to be compared to the experimental coefficients. MATLAB (2005) was employed for filtering noisy data and for data analysis. The noise present in the data files arises because the cases are transient, and the discretised equations do not always converge sufficiently fast enough within the prescribed number of iterations at every time step.

6.2.1 MATLAB (2005)

The motion, hull shape, oscillation frequency and time step for each case must be specified in the MATLAB (2005) function and the data file read. For each motion a data file was analysed to determine the relevant motion coefficients (table 6.1).

Table 6.1: Data extraction of uncoupled motions

Motion	Data file	Uncoupled force	Motion coefficient
Heave	lift coefficient	Total vertical	a_{zz}
			b_{zz}
Sway	Drag coefficient	Total horizontal	a_{yy}
			b_{yy}
Roll	Moment coefficient	Total moment	$a_{\phi\phi}$
			$b_{\phi\phi}$

The last three measured force/moment oscillations are assumed to have reached a periodic state and were used for data analysis purposes. Each complete oscillation curve of length T may be estimated with a Fourier series (FS). This FS description is very convenient when solving the simple equations of motion. Consider the Fourier series definition:

$$f(t) = \frac{a_0}{2} + \sum_{k=1}^{\infty} \left(a_k \cos(k.\omega.t) + b_k \sin(k.\omega.t) \right) \quad (6.2.1)$$

The Fourier coefficients for a discrete series with equal time steps (dt) are defined as:

$$a_k = \frac{2 \times dt \times \sum_{i=1}^N (f_i \times \cos(k\omega t_i))}{T} \quad (6.2.2)$$

and:

$$b_k = \frac{2 \times dt \times \sum_{i=1}^N (f_i \times \sin(k\omega t_i))}{T} \quad (6.2.3)$$

Where:

$$a_0 = \frac{2 \times \sum_{i=1}^N (f_i)}{T} \quad (6.2.4)$$

k is = 2 in this case. N is the number of discrete coefficient values in one period (T).

$$T = 2 \times \frac{\pi}{\omega} \quad (6.2.5)$$

The data from FLUENT (2009) contains numerous outliers, originating from unconverged time step results, that need to be filtered out. A median filter (Mitra, 2006) with a sliding window spanning over five samples (data points) is used. The data must be linearised before the filter can be applied. A second-order FS curve is sufficiently accurate enough for this curve fitting. The data is linearised by subtracting the fitted curve from the data points. After this linearisation, the median value of the samples specified in the window is determined. The standard deviation (σ) of the complete set of linearised data points is calculated with:

$$\sigma = \sqrt{\frac{1}{N} \sum_{i=1}^N (f_{lin} - \overline{f_{lin}})^2} \quad (6.2.6)$$

Where:

$$\overline{f_{lin}} = \frac{1}{N} \sum f \quad (6.2.7)$$

N is the total number of discrete f_{lin} values. If a point within the sliding window deviates more than σ , the point is considered to be an outlier. The data point is reassigned to the value of the median within that (five sample) window. The data is filtered twice before the coefficients are extracted.

A first-order FS is fitted to the filtered data. Higher order FS will estimate the measured force curves better but to comply with the simple equations of motion, this route cannot be followed. In this step accuracy will deteriorate, but maintaining simplicity must be enforced.

The first-order Fourier curve fit provide coefficients a_1 and b_1 that are used to determine the force amplitude Z_{osc} and the phase angle ε_{phase} through equations:

$$Z_{osc} = \sqrt{a_1^2 + b_1^2} \quad (6.2.8)$$

$$\varepsilon_{phase} = \arctan\left(\frac{a_1}{b_1}\right) \quad (6.2.9)$$

The equations from chapter 1 section 1.4 are then used to determine the coefficients a_{zz} , b_{zz} , c_{zz} , a_{yy} , b_{yy} , c_{yy} , $a_{\phi\phi}$, $b_{\phi\phi}$ and $c_{\phi\phi}$.

Finally the non-dimensional coefficients are calculated, plotted and compared to the results obtained by Vugts (1968).

6.3 Results and Discussion

6.3.1 Introduction

The experimental data points measured by Vugts (1968) were not electronically available. These points had to be manually read off the curves presented in his article. Slight inaccuracies are expected from this manual method. Vugts (1968) also mentions slight experimental inaccuracies, as discussed in subsection 6.3.10. The final results are presented in the same form as the experimental results by Vugts (1968). The x-axis values are defined by:

$$\omega\sqrt{\frac{B}{2g}} \quad (6.3.1)$$

Regarding the hulls in heave and sway, the mass coefficient ¹ is presented in the graphs by:

$$a_{ii}^* = \frac{a_{ii}}{\rho A} \quad (6.3.2)$$

and for the damping coefficient by:

$$b_{ii}^* = \frac{b_{ii}}{\rho A} \sqrt{\frac{B}{2g}} \quad (6.3.3)$$

The roll y-axis values are described by:

$$a_{\phi\phi}^* = \frac{a_{\phi\phi}}{\rho AB^2} \quad (6.3.4)$$

¹The mass coefficient refers to the hydrodynamic mass or mass moment of inertia

for the mass coefficient, and by:

$$b_{\phi\phi}^* = \frac{b_{\phi\phi}}{\rho AB^2} \sqrt{\frac{B}{2g}} \quad (6.3.5)$$

for the damping coefficient.

The frequency is non-dimensionalised through equation (6.3.1). The coefficients in the equations of motion are calculated per unit length (of hull along its longitudinal direction). Normalising the coefficients (with equations (6.3.2) to (6.3.5)) allows the results to be compared to the graphs plotted by Vugts (1968).

Using the submerged area and waterline breadth for normalising the coefficients is useful when comparing hulls of different sizes and shapes. Hull characteristic changes with dimension and geometry alterations may be observed on the same normalised coefficient curves. Geometry scale effects on the coefficients are not linear.

In cases where the numerically determined data points are beyond the limits of the x-axis of a plot, the data points are considered to be outliers. In the proceeding discussion of the results the numerically determined coefficients, for each oscillation frequency, will be referred to as data points 1-5 in ascending order of frequency. The last group of coefficient points at $\omega = 10.599 \text{ rad/s}$ will be referred to as data points 6a-6c. 6a is the result for the fine mesh, 6b for the medium and 6c for the course mesh simulations. Data points 1-5 are the results for meshes described in table 4.8.

6.3.2 V-bottom hull heave

In figure 6.6 the data point at $\omega = 10.599$ ($\omega \sqrt{\frac{B}{2g}} = 1.408$) looks slightly bolder than all the other points, this is an overlap of the values achieved for each case for this frequency with coarse, medium and fine grids.

Referring to figure 6.6, in general the numerically determined mass coefficient values correlate very well with the experimental ones. The first value (in ascending order of oscillation frequency, $\omega = 1.129$) is not present because it has a value of -9.74. This large discrepancy is assumed to be an outlier. The second data point ($\omega = 3.023$) is slightly larger than the experimental values. Points 3-5 and 6a-c correlate well with the overall trend of the experimental data points.

The damping coefficients seen in figure 6.6 are slightly over-predicted by the numerical model. An increase in the damping coefficient indicate that energy transfer from the oscillating hull to the surrounding fluid is larger than suggested by the experimental data. Again the first two data points seem unreliable. The reason for this poor correlation may be a result of the low

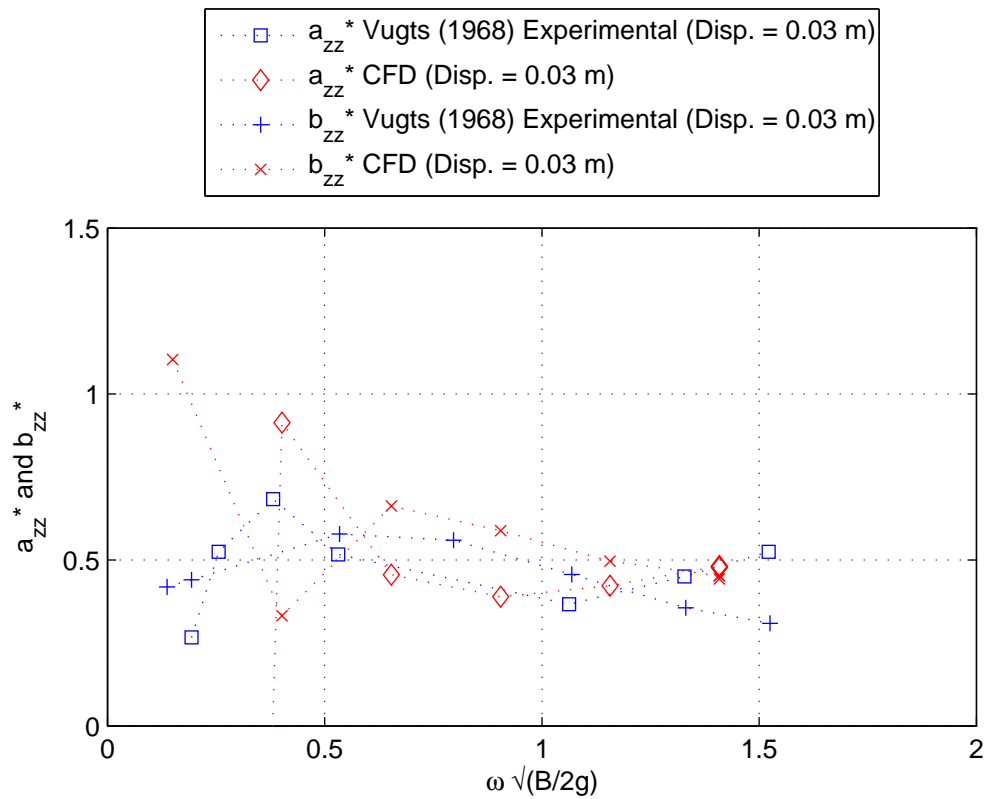


Figure 6.6: Mass and damping coefficients of a v-bottom hull in heave versus oscillation frequency presented by Vugts (1968) and the numerical coefficients obtained with CFD (FLUENT, 2009)

oscillation frequencies of the hulls in these simulations. As the oscillation frequency decreases, the near wall velocity decreases. The apparent turbulent viscosity becomes higher at this low frequency, thus affecting the numerical solution.

Presenting the measured numerical and experimental data in the form of measured force amplitude and phase angle may allow for clarity of coefficient observations. The amplitudes and phase angles of the forces or moments measured on the hulls are presented in Appendix B figure B.6.

Referring to the vertical force amplitude curve in figure B.6, a clear difference between the amplitude of the first data point ($\omega = 1.129$) and the experimental value near this point exists. The second data point does not dramatically deviate from the trend of all the data points, however the amplitude of this point affects the mass and damping coefficients considerably.

Data points 1 and 2 are the only cases where all maximum y^+ values measured along the surface of the hull remain below the recommended value of 5. It is interesting to note that from figure 6.6, these two points deviate the most from the experimental values. It is unclear why.

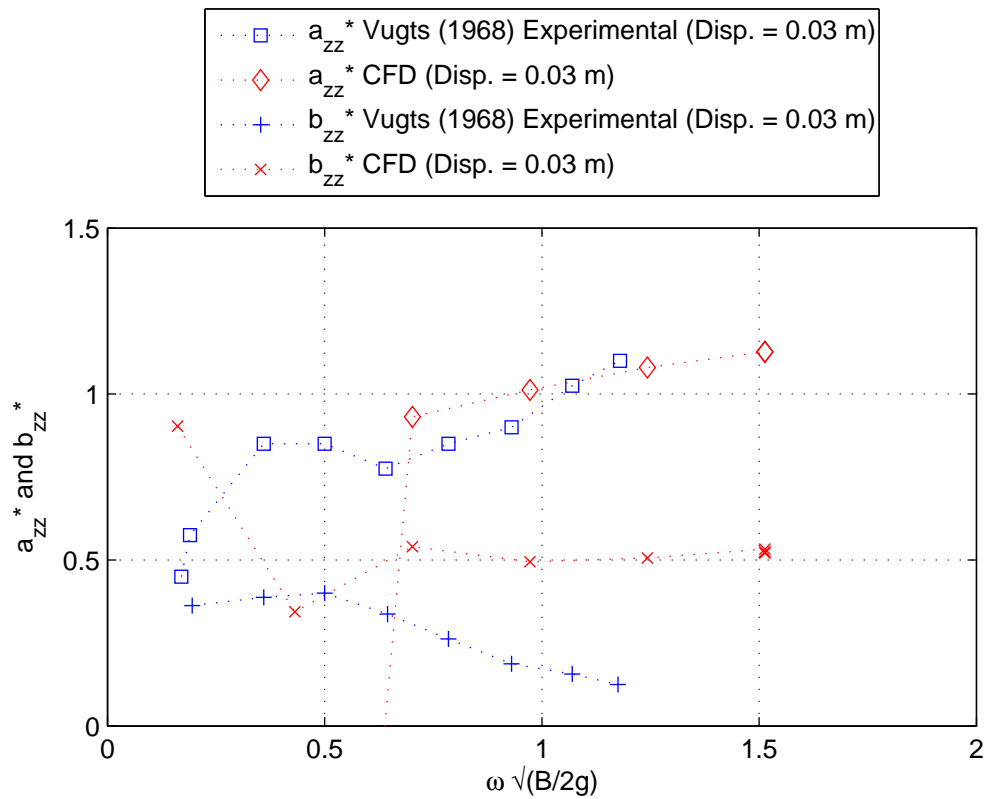


Figure 6.7: Mass and damping coefficients of a flat-bottom hull in heave versus oscillation frequency presented by Vugts (1968) and the numerical coefficients obtained with CFD (FLUENT, 2009)

It was expected that the first two numerical data points should correlate the best with the experimental results. At these low frequencies the y^+ values are acceptable and the flow velocities are low.

6.3.3 Flat-bottom hull heave

The first numerically determined data point (coefficient) in figure 6.7 cannot be seen on this curve because it has a value of -6.9886. Data points 2-4 predict a slightly higher damping coefficient value than the experimental points. Data point 5 is in good agreement with the last experimental coefficient point. Data points 6a-c cannot be directly compared to the experimental data because it is beyond the experimental test range.

Despite the good correlation between the mass coefficients discussed above, the damping coefficients in figure 6.7 display very different characteristics. Data point 1 of the numerical set has a much larger value than that of the experimental point. This point may be assumed to be an outlier. The trends of the experimental and numerical coefficients are considerably different. The

damping in the case of a flat-bottom hull is provided predominantly from the vortices that result as the sharp corners of the hull move through the water. This is discussed in more detail later.

Quérard *et al.* (2009) found good agreement between his numerical and Vugts (1968) experimental results. The added mass coefficient is slightly over-predicted at $\omega\sqrt{\frac{B}{2g}} < 1$, and slightly under-predicted at $\omega\sqrt{\frac{B}{2g}} > 1$. This is in agreement with figure 6.7. The damping coefficient is under-predicted by Quérard *et al.* (2009) in contrast to the extreme over-prediction of figure 6.7.

Despite the very large mass coefficient determined for the first numerical data point, the actual amplitude and phase angle of the data point does not seem entirely extreme (figure B.7). The vertical force amplitude, measured numerically, for this point is approximately 20 % larger than the experimental value presented by Vugts (1968). This indicates that the description of the hull characteristics in the form of mass and damping coefficients, in this case, is sensitive to the force amplitude measured. The numerical force amplitude and experimental points correlate well.

Data point 1 is the only case where the maximum y^+ values measured along the surface of the hull remain below 5. This point, however, deviates most from the data and is assumed to be an outlier.

Overall the numerical results correlate well with the experimental results for the mass coefficient. The damping is unacceptably over-predicted with the numerical method. Vortex shedding is suspected to be the main reason for this inaccuracy. Results obtained by Quérard *et al.* (2009) indicate that the numerical turbulence model used in this study is able to describe the flow field effects on the hull sufficiently.

For this case, the mass coefficient contributes mostly to the overall force measured on the hull. Looking at the simplified theory and force curve components, if the damping component increases, the phase angle increases and the amplitude increases. This is in agreement with figures 6.7 and B.7.

6.3.4 Round-bottom hull heave

A heaving round-bottom hull consists of a smooth geometry and a simple transitional motion. As the cylinder is displaced into the surrounding fluid, the problem can be solved accurately with numerical methods and models, however, the developing boundary layer is disturbed when the motion changes direction. The surrounding fluid has momentum in the opposite direction to the new motion. This case may lead to a complex flow field and phenomenon developing (including vortex shedding) around the geometrically simple hull.

Figure 6.8 shows that overall the numerically determined mass coefficients at higher frequencies correspond well with the experimentally determined points. Similar to the v-bottom and flat-bottom cases, the first numerical data point is an outlier. Data point 1 has a value of -12.061. Data point 2 is substan-

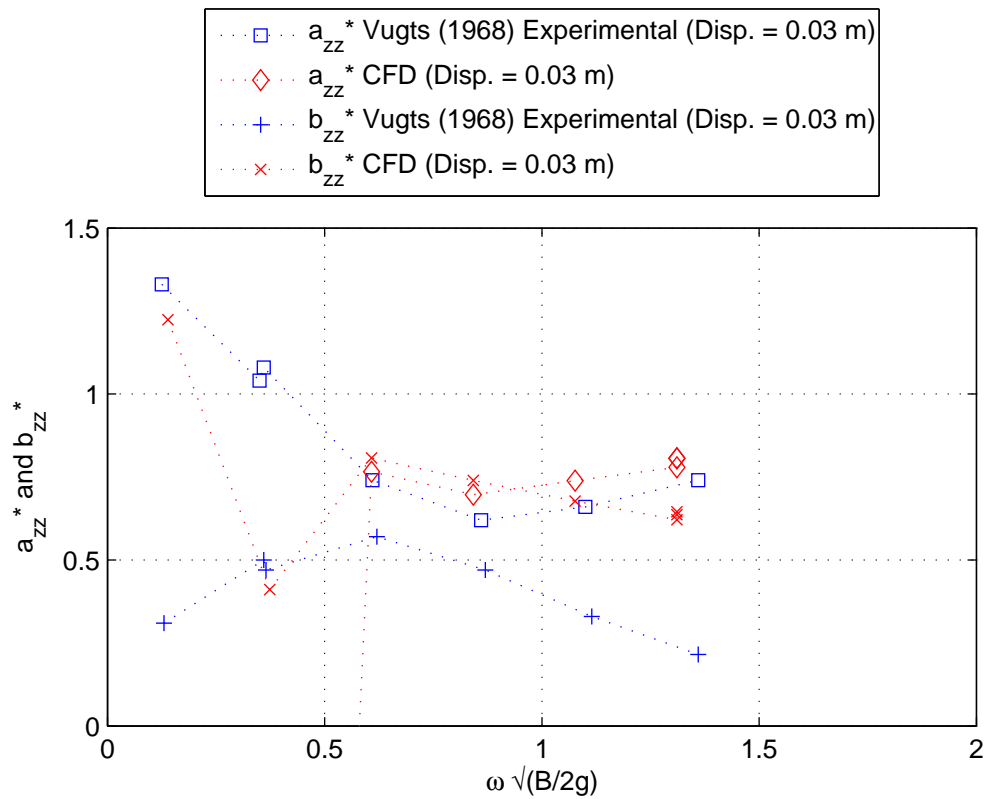


Figure 6.8: Mass and damping coefficients of a round-bottom hull in heave versus oscillation frequency presented by Vugts (1968) and the numerical coefficients obtained with CFD (FLUENT, 2009)

tially larger than the experimental values. Points 3, 4, 5 and 6a-c slightly over-predict the mass coefficients.

The damping coefficients seen in figure 6.8, are over-predicted at higher frequencies. Data point 1 is four times larger than the experimental value at a similar oscillating frequency. Data point 2 is under-predicted.

The force amplitude (figure B.8) of data point 1 is approximately 23 % larger than the amplitude of the experimental case. Data point 2 has a slightly smaller but acceptable amplitude. As the oscillating frequency increases from data point 3, the difference between the numerical and experimental force amplitudes increase.

Data point 1 and 2 adhere to y^+ values of smaller than 5. Data point 3 only slightly exceeds this limit and has a maximum value of $y^+ = 6.7$. This means that the point of transition to turbulence will move upstream. Simple boundary layer theory illustrates the sensitivity of the position of the point of transition with a change in y^+ values.

Numerical data point 1 in all the heave cases adhere to the $y^+ < 5$ condition, however these points remain to be regarded as an outliers. It may be

that the time step chosen for this simulation is not sufficiently small enough. Time step size was chosen as to increase linearly with a decrease in oscillation frequency. Vortices may be generated in this case, affecting the damping coefficients. A theoretical solution, proposed by Ursell (1949) and modified by Jong (1967), is a much simpler method to implement in predicting the coefficients for the flat-bottom and round-bottom heave cases. Below frequencies of $\omega\sqrt{\frac{B}{2g}} < 0.5$, the numerical results are inadequate.

6.3.5 V-bottom hull sway

The sway displacement is described in the same way as heave, however the motion considered is horizontal and not vertical. This is the only motion where a restoring moment is absent. Considering figure 6.9 the numerical mass coefficient in general correlates well with the experimental coefficients. Numerical data points 1 and 2 over- and under-predict the coefficient respectively. The experimental data trend is mimicked by the numerical points, especially in the higher frequency range. It should be noted that the hull motion displacement is 0.02 m in magnitude as opposed to 0.03 m. Later it will be seen how the displacement amplitude does not have major effects on the coefficients in the sway case.

Figure 6.9 also shows a very good correlation between the numerical and experimental results. In the lower frequencies (data points 1, 2 and 3) slightly over-predict the damping coefficients. The higher frequency range (points 4, 5 and 6a-c) slightly under-predict the damping.

The amplitude plot in figure B.9 shows an excellent correlation between the numerical and experimental force amplitudes. In the higher frequency range the numerical and experimental points follow the same trend.

The maximum y^+ values at the walls of the hull for data point 1, are all below 5.

The overall numerically determined coefficients correlate very well with the experimental coefficients. For this case, a good theoretical solution does not exist.

6.3.6 Flat-bottom hull sway

Vugts (1968) carried out this set of experiments with a hull oscillation displacement amplitude of 0.02 m. The numerical analysis carried out included both 0.02 m and 0.03 m displacement amplitudes.

In figure 6.10, the experimental mass coefficients presented by Vugts (1968) follow the same trend but is smaller in magnitude to the v-bottom case (6.9). The numerical data again over-predicts the coefficient at point 1 and under-predicts it at point 2. Data point 3 also slightly under-predicts the mass

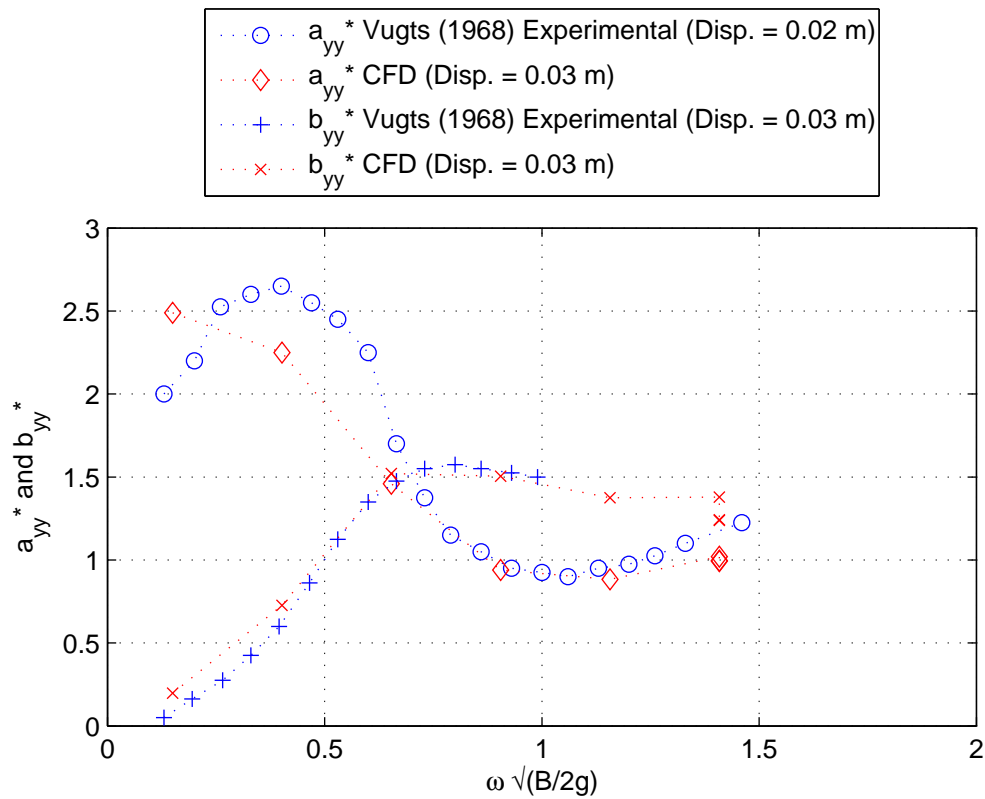


Figure 6.9: Mass and damping coefficients of a v-bottom hull in sway versus oscillation frequency presented by Vugts (1968) and the numerical coefficients obtained with CFD (FLUENT, 2009)

coefficient. Regarding the numerically determined coefficients, the hull oscillation displacement amplitude does not seem to influence the coefficients greatly. The overall trends of the three data sets are similar to one another.

It can again be seen in figure 6.10 that data points 1 and 2 do not correlate very well with the experimental data. Data points 3, 4, 5 and 6a-c for both numerical sets produce well correlating damping coefficients. The damping coefficients in this higher oscillation frequency range are, however, slightly under-predicted.

The force amplitude measured numerically (figure B.10) is lower than the experimentally measured ones. It is surprising that the lower displacement numerical amplitude is approximately half that of the experimental results. In figure 6.10 the data correlation looks much better than in figure B.10. This misleading contrast illustrates that the force amplitude and phase angle combination is vital in determining the correct coefficients.

A theoretical method presented by Vugts (1968) predict the mass and damping coefficients better than the numerical solution.

The first points of the experimental coefficients for both the large (displace-

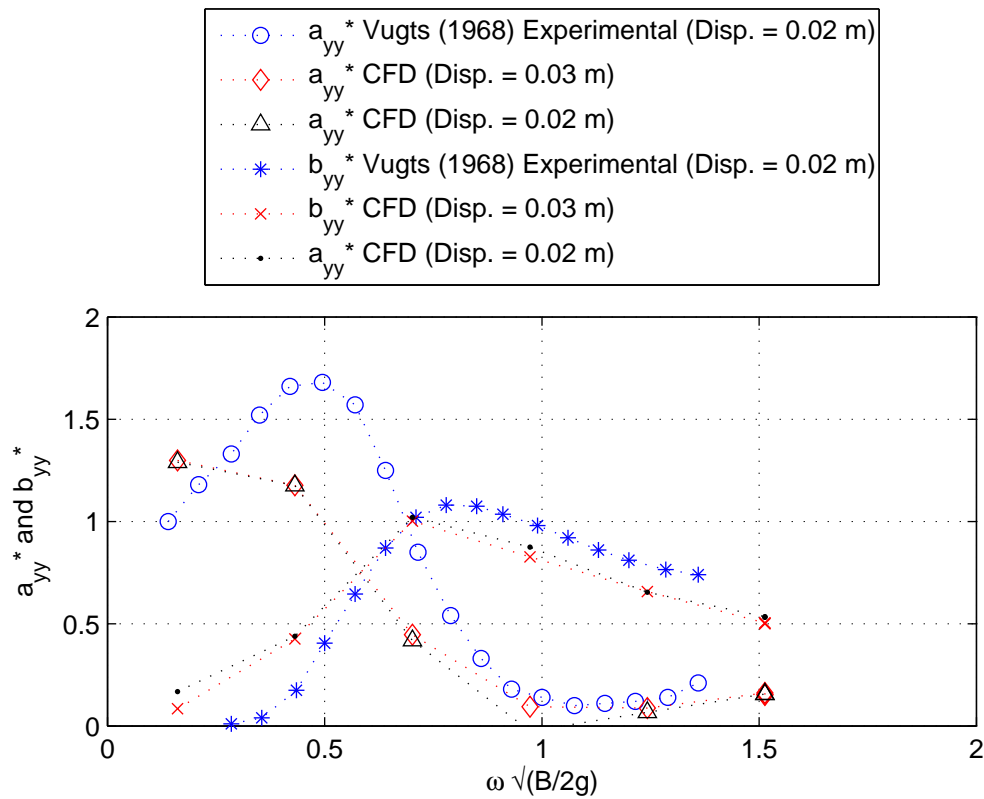


Figure 6.10: Mass and damping coefficients of a flat-bottom hull in sway versus oscillation frequency presented by Vugts (1968) and the numerical coefficients obtained with CFD (FLUENT, 2009)

ment = 0.03 m) and small (displacement = 0.02 m) amplitude displacement cases meet the y^+ requirement. The results obtained from the numerical solutions do not indicate that they are very sensitive to the value assumed by y^+ along the wall surface. All the y^+ values remain below 20. The flat-hull geometry lends itself to producing complicated flow fields. In this case the numerical solution performed well considering the flow complexities involved. Figure 6.10 clearly indicate that the amplitude does not play a significant role in determining the coefficients, because the forces measured are divided by the hull displacement amplitude illustrated in equations 1.4.7 to 1.4.12.

6.3.7 Round-bottom hull sway

Contrary to the heave case the sway case is asymmetrical which may allow for water flow towards the free-surface producing waves.

The experimental and numerical added mass coefficients in figure 6.11 show similar trends and are of similar magnitude to the coefficients presented in figure 6.10. In this case the numerically determined data points are largely

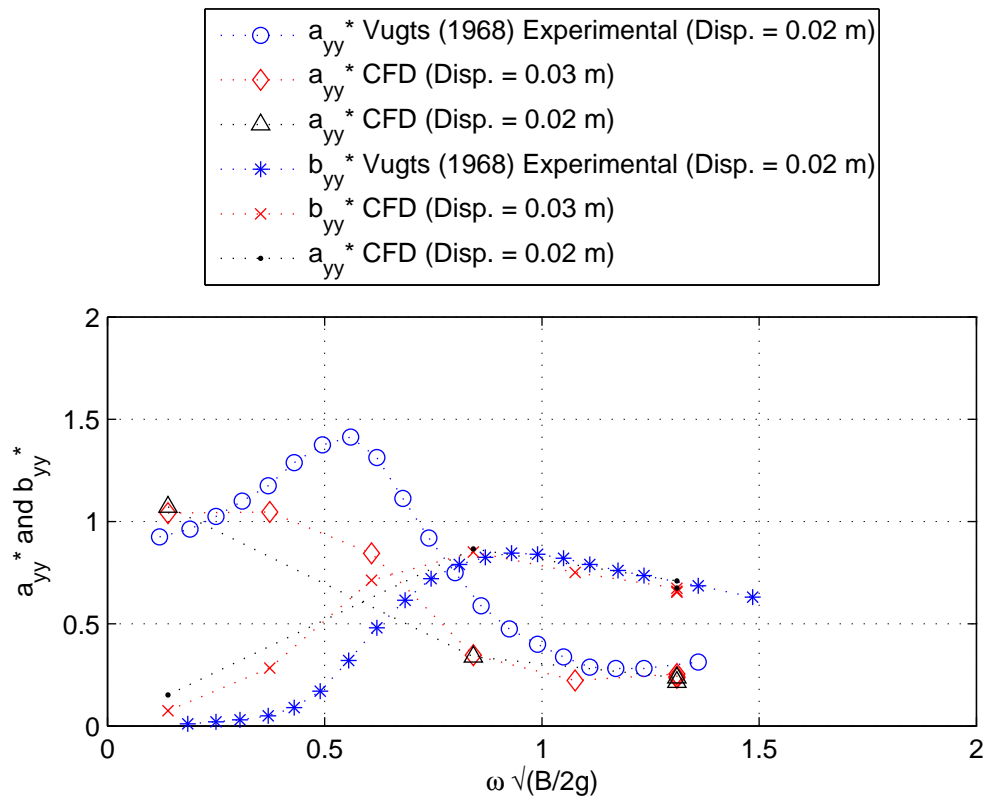


Figure 6.11: Mass and damping coefficients of a round-bottom hull in sway versus oscillation frequency presented by Vugts (1968) and the numerical coefficients obtained with CFD (FLUENT, 2009)

underestimated. The correlation between the numerical and experimental coefficients seem very similar to the flat-bottom hull case. Again the coefficients for the large and small hull motion displacements assume very similar values. All the numerical coefficients, except for data point 1, under-predict the coefficients.

The damping coefficients in figure 6.11 indicate that the experimentally determined coefficients are smaller than that of the flat-bottom hull case. This is expected because of the smooth geometry of the round-bottom hull. The numerical coefficients over-predict the damping before the coefficient value turning point, where the coefficient decreases with an increase in frequency. After this turning point, the damping is slightly under-predicted. It is as if there is a shift in the damping values with respect to the oscillation frequency. The small and medium oscillation displacement numerical coefficient values are in close proximity to one another. At the lowest tested frequency the two sets of numerical data differ noticeably. The horizontal force amplitude of the large oscillation displacement and experimental points in figure B.11 correlate well. At the smallest oscillation frequency the numerical and experimental

amplitudes seem to agree. The scale of the curve may conceal the actual difference in amplitude at this low frequency. The actual percentage difference is 14 %.

The theoretical solution presented by Vugts (1968) correlate much better to the experimental coefficients than the numerical solution.

The y^+ values for the medium and large oscillation amplitude displacement flow cases are below 5 only for the lowest oscillation frequencies. Meeting the y^+ value requirement does not seem to have a very significant positive (or negative) effect on the coefficients.

As with the flat-bottom case, the numerical results display similar trends to the experimental plots. The numerical prediction of the coefficients are not satisfactory. Even though a simple flow field is expected, physical phenomenon may be present that complicates the flow field. The visualization of these flow fields may allow insight into apply flow specific models to each motion and hull shape case. By doing this, the mass and damping coefficients may be better predicted.

6.3.8 V-bottom hull roll

Data point 2 is not displayed in figure 6.12 because the results obtained for this specific case did not make sense. The numerical prediction of the mass moment of inertia coefficients and experimentally determined coefficients correlate well, with the exception of data point 4. It must be noted that in all the previous cases, data points 1 were regarded as being outliers. Whether data point 1 is reliable cannot be verified by figure 6.12. Data point 6a has a noticeably larger value than points 6b and 6c. This is further discussed in chapter 5. The experimental data points are derived from a smaller oscillation amplitude case. As seen in figures B.9 to B.11, the oscillation amplitude does not have a large impact on the predicted coefficients

Figure 6.12 also shows a very good correlation between the numerical and experimentally determined damping coefficients. Here data point 4 is slightly over-predicted, but still correlates well with the experimental data. Point 6a is again completely different to points 6b and 6c.

The moment measured and presented in figure B.12 indicates that all the numerical values are in agreement with the experimental ones. It is surprisingly interesting that the two data sets consider two different roll angles but match up well. Vugts (1968) indicated that his measurements are for a roll case where the roll angle is 0.1 rad. The numerical solution is for a case where the roll angle is 0.2 rad. Both coefficients are normalised by the roll amplitude. The reason for this very good correlation is may be because the difference between the roll angles is only 0.1 rad.

Chen and Liu (2002) conducted a numerical investigation into the roll motion of a three-dimensional hull. They found that the skag of a hull, which is geometrically similar to a triangle, produced very large fluid vertical velocity

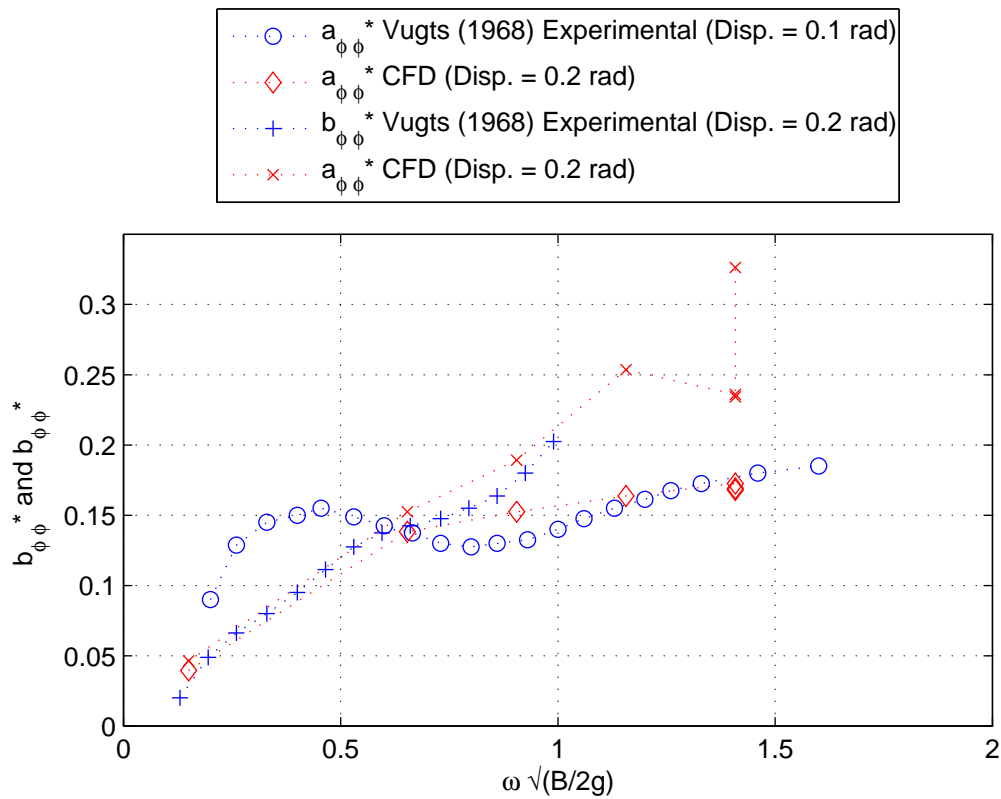


Figure 6.12: Mass moment and damping coefficients of a v-bottom hull in roll versus oscillation frequency presented by Vugts (1968) and the numerical coefficients obtained with CFD (FLUENT, 2009)

components at the free-surface. This results in waves forming at the water surface. There is very little other data available in literature for this case.

None of the rolling v-bottom hull cases comply with the y^+ limit of 5. Shear stresses may not play a very large role in affecting the hydrodynamics of a rolling v-bottom hull. Regarding figure B.12, it is clear that data point 1 is not an outlier. This point follows the same trend as the experimental points for the lower oscillation frequency region. The numerical prediction of the mass moment of inertia and damping coefficients correlate very well to the experimental coefficients. The numerical solution also produces significantly more accurate results than the theoretical solution presented by Vugts (1968). As mentioned, wave making contributes to most of the damping. This phenomenon predominantly involves linear pressure differences between mesh cells resulting in a simpler flow field compared to vortex shedding. A very fine grid is thus not required to capture the flow phenomenon. Even though the y^+ values are larger than the recommended limit of 5, results are satisfactorily accurate.

6.3.9 Flat-bottom hull roll

Flat-bottom hulls in roll have recently been extensively investigated, both numerically and experimentally. Most current numerical investigations are concerned with these sections in roll (see work by Yeung *et al.* (1998), Sarkar and Vassalos (2000), Quérard *et al.* (2009)). Available data makes benchmarking the current investigation easier and more reliable. This flow case is also one of the more complex cases because of flow phenomenon such as vortex shedding.

Figure 6.13 illustrates that the numerically determined mass moment of inertia coefficients over-predict the experimental coefficients slightly. Data point 2 is considerably over-predicted numerically. With an increase in oscillation frequency, the numerical solution increasingly over-predicts the damping. The trend of the numerical data points is similar to that of the experimental points with regard to oscillation frequency increase.

The damping coefficients in figure 6.13 are also over-predicted by up to 50 % of the experimentally determined coefficient. Again the two data sets follow the same trends with regard to an increase in oscillation frequency. These results are, however, not satisfactory. The effects of the phenomenon that contribute to damping are not fully captured. Even though an increase in mesh fineness decreases the damping coefficient, the numerical model may be insufficient in solving this case.

The amplitude plot (figure B.13) reveals that the amplitude measured numerically is realistic compared to the coefficient comparison. The numerical amplitude is, however, over-predicted. Again, as the oscillation frequency increases, the difference between the numerical and experimental coefficients increase.

Sarkar and Vassalos (2000) discussed how vortices are generated around a flat-bottom hull rolling at a free-surface. A roll angle of 11.5° was investigated. The velocity vectors become very large near the corners of the hull. It was also emphasize that theoretically, the RANS-based technique used had the ability to predict separation points and vortex formations accurately. The accuracy of the technique depends on the turbulence model for a particular type of flow. Sarkar and Vassalos (2000) achieved very similar results for a rolling square to those presented in this report. They also presented coefficients for a flat-bottom hull with the same bilge radius as the hull tested by Vugts (1968). These radius-bilge results correlate better with the experimental results than the perfect square-hull. The numerical solution achieved in the present study for radius-bilge hulls, produces the same results as a perfect square-hull modelled by Sarkar and Vassalos (2000). The current grid must be even more refined at the corners of the hull. The corners and corner radii of these hulls play a very large role in influencing the hull hydrodynamic characteristics.

A free-surface random-vortex method (FSRVM) was used by Yeung *et al.* (1998) to predict the mass moment of inertia and damping coefficients for a rolling flat-bottom hull. This method was used because vortex shedding is ex-

pected in this oscillating hull case. Experimental work was also conducted for validation purposes. The cylinder was geometrically similar to the one tested by Vugts (1968) with dimensions 1' x 1' (0.3048 x 0.3048 m) as opposed to 0.4 x 0.4 m. This smaller model produced a larger mass moment of inertia but a similar (and slightly lower) damping coefficient to Vugts (1968) experimental tests. The numerical results from this article were not available. The current numerically determined coefficients do not correlate very well with the experimental results presented by Yeung *et al.* (1998).

The mass moment of inertia obtained by Quérard *et al.* (2009) is over-predicted by much larger values than the work presented in this report. Quérard *et al.* (2009) managed to predict the mass and damping coefficients extremely well with a hybrid grid for heave and sway cases, but failed to achieve the same accuracy for this roll case. Their numerically predicted damping coefficient presented correlates better than that of the results presented in this report. It must be stressed that the work presented by Quérard *et al.* (2009) is for a cylinder rolling with a roll angle of 2.87° whereas this study is concerned with a roll angle of 11.46° . At small angles of roll, vortex shedding may not be as prominent as for large angles of roll. Chen and Liu (2002) found that bilge keels induce local flow separation and strong vortices. A flat-bottom hull induce similar flow effects but to a lesser degree.

As with most of the cases only the first data point's y^+ value is below 5. The maximum y^+ value for the data point 6a is 25.

Predicting the mass moment of inertia and damping coefficients for a rolling flat-bottom hull is difficult for large roll angles. Vortex generation and flow separation play increasingly larger roles in these hull motions with an increase in roll angles. The numerical solution in this report may be verified with the results obtained by Sarkar and Vassalos (2000) for a perfectly square-hull. Numerical data presented by other authors correlate very well for small displacement translations and angles.

6.3.10 Round-bottom hull roll

The round-bottom hull in roll is considered to be a simple case where only frictional forces are present (Blagoveshchensky, 1962) and wave and vortical forces are absent. It is interesting that the added mass moment of inertia (figure 6.14) is negative for this roll case. The phase angle is the only factor that can cause this. This indicates that the fluid contributing to the added mass has a lag which reduces the overall mass moment of inertia effect. The numerical and experimental coefficients do not correlate well. Both data sets follow similar trends. Data point 6c is absent from the data set because this simulation case produced unusable results.

The experimental coefficients presented in figure 6.14 are negative at $\omega\sqrt{\frac{B}{2g}} < 0.5$. This error is discussed by Vugts (1968). The numerical data points do not

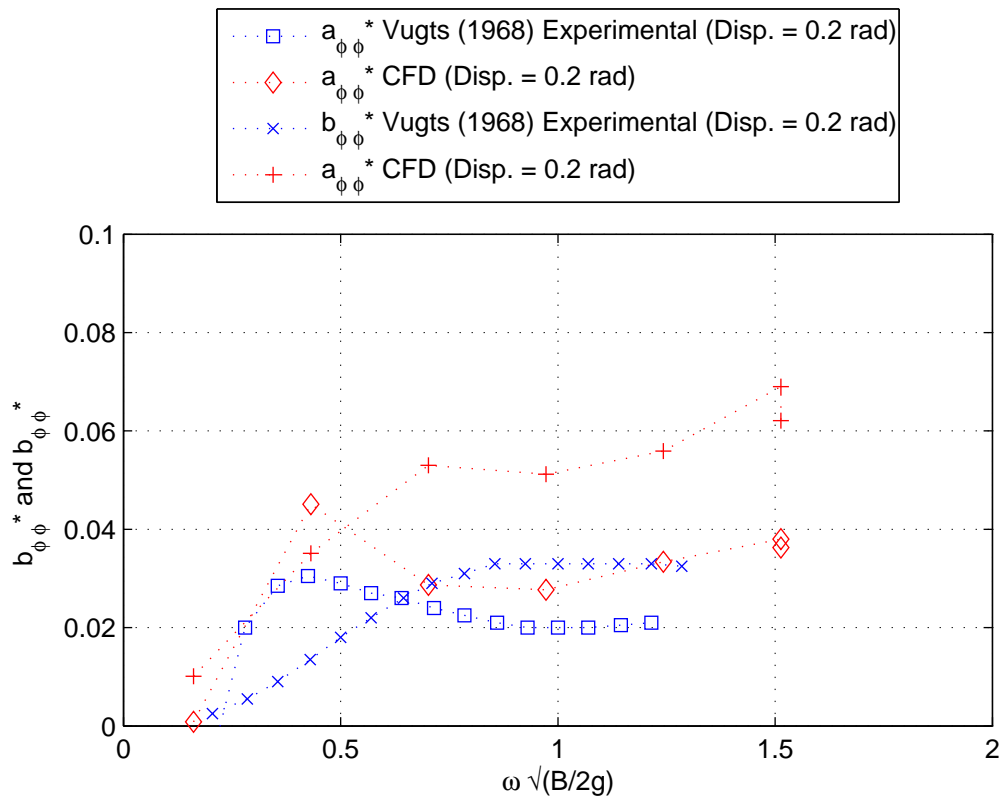


Figure 6.13: Mass moment and damping coefficients of a flat-bottom hull in roll versus oscillation frequency presented by Vugts (1968) and the numerical coefficients obtained with CFD (FLUENT, 2009)

become negative at these oscillation frequencies and increases slightly with an increase in frequency. The experimental and numerical data start to diverge from each other at approximately $\omega \sqrt{\frac{B}{2g}} = 0.6$. Despite the small error in the experimental tests, the numerical solution does not seem to capture the physical flow phenomena effects for this motion, because of the complexity of this transient problem's boundary layer. Skin friction is the main damping factor for a rolling circular cylinder (Blagoveshchensky, 1962). The y^+ values achieved in the numerical simulation are larger than 5 for all the data points presented in figure 6.14. This influences the results noticeably for this specific case.

It is clear in figure B.14 that the numerical solution fails to capture the moment exerted on the hull (from surface shear stresses) by the surrounding fluid. Comparing the results from figures B.12, B.13 and B.14, the round-bottom hull in roll experiences the least amount of moment (by a factor of 10). This indicated that the shear stress exerted on the hulls in all the cases contribute differently in each case. The shear stresses are not accurately pre-

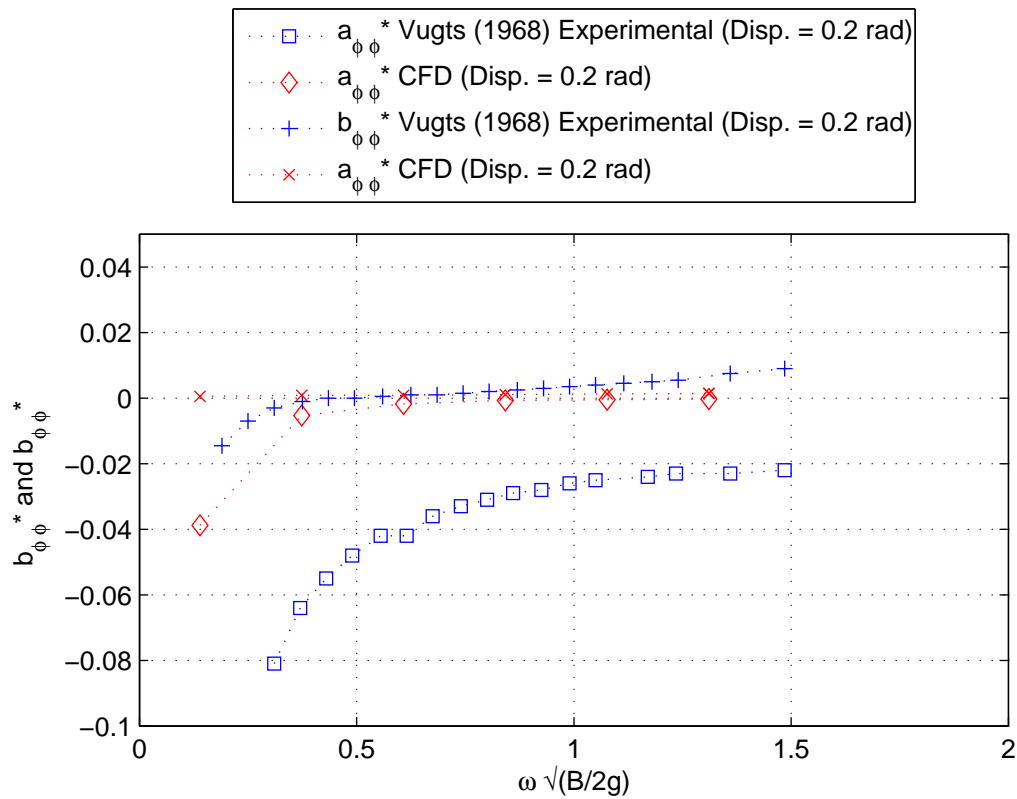


Figure 6.14: Mass moment and damping coefficients of a round-bottom hull in roll versus oscillation frequency presented by Vugts (1968) and the numerical coefficients obtained with CFD (FLUENT, 2009)

dicted with this current numerical model. This error may be acceptable in cases where shear stress contributes very little to the overall measured moment (such as the v-bottom hull in roll). For the flat-bottom hull in roll the surface shear stress inaccuracy may lead to inaccurate results.

Vugts (1968) states that his experimental tests may contain slight errors with regards to the results presented for a round-bottom hull in roll. Despite this, the current model for this case fails to capture the surface shear stress effectively.

The y^+ value of data point 1 slightly exceeds the limit of 5 and assumes a value of 5.7. The maximum y^+ value achieved for the higher frequencies is 19.5. Because the surface shear stress plays a large roll in the total moment measured on the hull, the y^+ values for this case are vital.

Regarding the shear stressed and the influence that it may have in certain cases, a round-bottom hull in roll should be used to initially benchmark a model's ability to capture this frictional force. The numerical solution for this case is inappropriate and may require a much finer mesh to capture the surface shear stress effects on the measurements of the moment exerted on the hull.

The effects of the y^+ values is further discussed in section 5.2.

6.4 Conclusion

It is suspected that vortex shedding is the main reason for major discrepancies. In the case of the v-bottom hull, the fluid is slightly displaced horizontally (by the wedge shape of the hull) and then flows back toward the hull (as the hull returns to its original position). In the case of the round bottom and flat-bottom hulls, the horizontal fluid displacement is very large. As the hull moves out of the water, the expelled fluid needs to be replaced. Fluid flows back horizontally and vertically to the regions of lower pressure under the hull. This counter and cross flow results in circular flow (i.e. vortices). The round-bottom hull case flow field is similar to that of the flat-bottom hull, but less severe.

The v-bottom hull has an average normalised hydrodynamic mass coefficient value of approximately $a_{zz}/(\rho A) = 0.5$. The flat-bottom hull coefficient is approximately $a_{zz}/(\rho A) = 1$ across the frequency ranges. The coefficient for the round bottom hull varies from $a_{zz}/(\rho A) = 1$ at lower frequencies to $a_{zz}/(\rho A) = 0.6$ for the higher frequency range. This indicates that the flat-bottom hull entrains the most water as it oscillates vertically. The damping coefficients for all the hulls display similar characteristics. At oscillation frequencies $\omega\sqrt{B/2g} < 0.5$, the coefficients are lower than the mean damping values, maximum at $\omega\sqrt{B/2g} = 0.5$ and then steadily decreases from $\omega\sqrt{B/2g} > 0.5$.

In the sway cases, slight differences between the numerical and experimental results occur at frequencies where $\omega\sqrt{B/2g} < 1$. The flat-bottom and round-bottom hull damping coefficients are both over-predicted numerically for $\omega\sqrt{B/2g} < 0.7$ and under-predicted above this frequency. It is not surprising that the round-bottom hull has the lowest hydrodynamic mass, because the fluid flows around this body more easily than in the other cases.

These results for the roll cases again illustrate how the v-bottom hull acts as a wave-maker. The negative coefficients calculated for the round-rolling cylinder may be from some of the excited fluid surrounding the hull flowing in the opposite direction to the rotation of the hull. The overall result is a reduction of the mass moment of inertia. The difference between the numerical and experimental coefficients for the flat-bottom hull are magnified because of the scale of the graph.

Chapter 7

Conclusion And Recommendations

7.1 Summary

Forced hull oscillations were investigated.

Numerical models were used to determine the hydrodynamic properties of three distinctly different typical ship-like hull sections. The validity of these characteristics were evaluated with the experimental results presented by Vugts (1968).

The dominant flow features for the different hull forms were identified. The influence and effects of these dominant flow phenomenon for the different cases were observed.

7.2 Numerical Characterisation and Model Evaluation

CFD results were successfully compared to the experimental results presented by Vugts (1968). The hull shapes numerically investigated in the heave motion produced satisfactory results for the hydrodynamic mass coefficient. The damping coefficients were over-predicted, especially for the flat and round bottom hulls.

Characterising the hull forms with equations 1.4.1 to 1.4.5 may reduce the accuracy and details of the true characteristics of a hull. Out of the three hulls, the v-bottom hull has the lowest hydrodynamic mass. The damping coefficients for the v-bottom and round-bottom hulls are interestingly higher than the damping coefficient of the flat-bottom hull.

For the sway cases, the hydrodynamic mass and damping coefficients are also predicted very well numerically, especially for the v-bottom hull. Vortex shedding in the sway cases is not as dominant as for the heave cases because of the direction of the oscillation. Comparing all three hulls in sway, the v-bottom hull has the highest hydrodynamic mass coefficient, then the flat bottom hull

and finally the round bottom hull. The v-bottom hull in this motion acts as a wave-maker with its high draft versus submerged-area ratio.

With regard to the damping of the three different shapes, the order in descending hydrodynamic and damping coefficient are the v-bottom, flat-bottom and round-bottom hulls.

The numerical hydrodynamic mass and damping coefficients for a v-bottom hull in roll corresponds very well with the experimental values. The numerical results for the round-bottom hull look promising, but for the flat-bottom, further investigation is required.

The v-bottom hull has an extremely high mass moment of inertia coefficient when compared to the flat-bottom and round-bottom hulls. The damping for the v-bottom hull is largest. The difference between the flat-bottom results and the v-bottom hull results may after all not be as drastic as expected.

It is clear that numerical models are very powerful tools in these complex flow cases. The results obtained from these numerical simulations indicate that in most cases the models capture the effects of the flow phenomena reasonably well.

Quérard *et al.* (2009) obtained a good correlation between numerical and experimental results by Vugts (1968). The main reason for this is that small displacement oscillations were considered. This project deals with large oscillation displacements, which challenges the applicability of some numerical models.

7.3 Presence and Effects of Fluid Phenomena

The effects of flow phenomena on hull resistance are qualitative and cannot explicitly be quantified. Table 7.1 tabulates the dominant flow features in each case and the current numerical approach suggested to capture the effects of the relevant flow phenomenon.

It is not possible to use a single numerical technique for every hull-motion case. Certain numerical models often capture specific flow phenomenon very well but fail to describe others.

7.4 Prescribed Displacement

The approach of forced displacement of the hulls are very convenient for experimental purposes. Reliability and consistency is more easily achieved than in the free roll decay test cases. Forced motion experimental data is also more readily available in literature (potentially because of the above mentioned reasons). It was found, however, that for the purposes of a numerical investigation, achieving a periodic solution was difficult. A substantial number of oscillations

Table 7.1: Numerical models recommended for hull characterisation

Hull	Predominant resistance	Recommended model
Heave		
V-bottom	Wave	Transition SST
Flat-bottom	Vortical (eddy)	Theory (Jong, 1967)
Round-bottom	Vortical (eddy)	Theory (Jong, 1967)
Sway		
V-bottom	Wave	Transition SST or Theory (Jong, 1967)
Flat-bottom	Wave & vortical (eddy)	Theory (Jong, 1967)
Round-bottom	Vortical (eddy)	Theory (Jong, 1967)
Roll		
V-bottom	Wave	Transition SST
Flat-bottom	Vortical (vortex shedding)	FSRVM (Yeung <i>et al.</i> , 1998)
Round-bottom	Frictional	Theory (Jong, 1967)

are required to achieve a periodic solution, (15+ for heave and sway, and 20+ for roll cases). This approach is computationally very expensive.

7.5 Future Work

A case by case investigation with different numerical models may indicate which models are most applicable in different cases. A extremely fine mesh refinement may be employed for the corner regions of a flat-bottom hull. Numerical models also perform differently where certain flow phenomena are present. RANS-based methods may work well for cases where small displacements are considered (Quérard *et al.*, 2009), but for larger displacements and different hull forms a FSRVM may be more appropriate. As mentioned by Yeung *et al.* (1998), the FSRVM does not model turbulence. This may allow for vortices to decay more slowly numerically than they physically do, resulting in an over-predicted damping. The effects of adding a third dimension to the problem may be further investigated.

Conducting experimental and numerical work for free-oscillating hulls of different cross section may further validate the current work and potentially reveal different hull characteristics.

Appendices

Appendix A

Additional Numerical Set-Up Calculations

A.1 Numerical Model Calculations

A.1.1 Boundary Condition Constants and Calculations

Determining the characteristic length as proposed by FLUENT (2009a) for calculating boundary turbulence parameter values:

$$l = 0.07L \quad (\text{A.1.1})$$

$$= 0.07 \times 2.25 \quad (\text{A.1.2})$$

$$= 0.1575 \text{ m} \quad (\text{A.1.3})$$

Estimating the turbulent kinetic energy from turbulence intensity:

$$k = \frac{3}{2}(u_{avg}I)^2 \quad (\text{A.1.4})$$

$$= \frac{3}{2}(0.00005 \times 0.0005)^2 \quad (\text{A.1.5})$$

$$= 9.375 \times 10^{-16} \text{ m}^2/\text{s}^2 \quad (\text{A.1.6})$$

Estimating the specific dissipation rate from a length scale:

$$\omega = \frac{k^{1/2}}{C_\mu^{1/4}l} \quad (\text{A.1.7})$$

$$= \frac{(9.375 \times 10^{-16})^{1/2}}{0.09^{1/4}0.1575} \quad (\text{A.1.8})$$

$$= 354.39 \times 10^{-9} \text{ s}^{-1} \quad (\text{A.1.9})$$

A.1.2 Time Step Calculations

The angular displacement is 0.2 rad and the maximum frequency (ω) is 10.599 rad/s. It is assumed that the hull wall velocity value is equal to the value of the

free-stream velocity used for maximum flow and boundary layer calculations.

$$\begin{aligned}\phi &= \phi \cdot \sin(\omega \cdot t) \\ \dot{\phi} &= \phi \cdot \cos(\omega \cdot t) \cdot \omega \\ \dot{\phi}_{max} &= \phi \cdot 1 \cdot \omega \\ \dot{\phi}_{max} &= 0.2 \cdot 10 \cdot 599 \\ v_{max} &= r \cdot \dot{\phi}_{max} \\ v_{max} &= 0.3 \times 0.2 \times 10 \cdot 599 \\ v_{max} &= 0.636 \text{ m/s}\end{aligned}$$

The minimum cell volume is 1.232495×10^7 (for the flat-bottom hull, heave case) thus using equation (3.4.6)

$$\begin{aligned}\Delta t &= \frac{(1.232495 \times 10^{-7})^{1/3}}{0.636} \\ \Delta t &= 0.007825 \text{ s}\end{aligned}$$

A.2 y^+ Calculations

It is assumed that the maximum fluid velocity is approximately equal to the maximum hull motion velocity (it was noted that fluid flowing in the opposite direction of the hull motion will experience even larger fluid velocities.) From the time step calculation the maximum flow velocity is: $v_{max} = 0.636 \text{ m/s}$ Boundary layer surface shear stress calculations:

$$\tau_w = \frac{0.332 \rho U_\infty^2}{\sqrt{Re_x}}$$

For the point of instability: $Re_x \approx 9.1 \times 10^4$

$$\begin{aligned}\tau_{w,instability} &= \frac{0.332/10000 \cdot 636^2}{\sqrt{9.1 \times 10^4}} \\ &= 0.4452 \text{ N/m}\end{aligned}$$

For the point of final transition to turbulence: $Re_x \approx 3 \times 10^6$

$$\begin{aligned}\tau_{w,transition} &= \frac{0.332/10000 \cdot 636^2}{\sqrt{3 \times 10^6}} \\ &= 0.0775 \text{ N/m}\end{aligned}$$

Determining the friction velocity:

$$u_\tau = \sqrt{\tau_w / \rho}$$

$$\begin{aligned} u_{\tau,instability} &= \sqrt{0.4452/1000} \\ &= 0.0211 \text{ m/s} \end{aligned}$$

$$\begin{aligned} u_{\tau,transition} &= \sqrt{0.0775/1000} \\ &= 0.0088 \text{ m/s} \end{aligned}$$

Substituting these values into the y^+ equations to determine y

$$\begin{aligned} y_{\omega} &\leq \frac{y^+ \nu}{\rho u_{\tau}} \\ &\leq \frac{5 \times (100.3 \times 10^{-5}/998.2)}{998.2 \times 0.0211} \\ y_{instability} &\leq 238.5 \times 10^{-6} \text{ mm} \\ &\leq \frac{5 \times (100.3 \times 10^{-5}/998.2)}{998.2 \times 0.0088} \\ y_{transition} &\leq 571.9 \times 10^{-6} \text{ mm} \end{aligned}$$

A.2.1 Falkner-Skan Calculations

$$U_e = Cx^a \quad (\text{A.2.1})$$

For a wedge angle of $\alpha = 90^\circ$, $a = 1$ and for flat plate flow $\alpha = 0^\circ$, $a = 0$, thus $C = U_\infty$, thus:

$$U_e = U_\infty x$$

The point of instability is at $Re_{\delta^*} = 12490$.

$$Re_{\delta^*} = \frac{U_e \delta^*}{\nu} \quad (\text{A.2.2})$$

Making δ the subject of the formula:

$$\delta^* = \frac{12490\nu}{U_e} \quad (\text{A.2.3})$$

From the Falkner-Skan solution:

$$\frac{\delta^*}{x/\sqrt{Re_x}} = 0.648 \quad (\text{A.2.4})$$

Making δ^* the subject of the formula:

$$\delta^* = \frac{0.648x}{\sqrt{Re_x}}$$

Equating equations (A.2.1) and (A.2.4)

$$\frac{12490\nu}{U_e} = \frac{0.648x}{\sqrt{Re_x}}$$

Substituting equation (A.2.1) into the above equation:

$$\frac{12490\nu}{U_e} = \frac{0.648x}{\sqrt{Re_x}}$$

From equation (A.2.1)

$$\frac{12490\nu}{U_\infty x} = \frac{0.648x}{\sqrt{U_\infty}}$$

Referring back to equation (4.2.5). The shear strain rate $\left(\frac{\partial u}{\partial y}\right)$ is computed at each grid point with Navier-Stokes equations. Flat plate boundary layer theory was used beforehand to estimate this value. The Blasius solution for flat-plate flow solves the shear stress with:

$$\tau_w = \mu \left(\frac{\partial u}{\partial y}\right)_{y=0} \approx \frac{0.332\rho U_\infty^2}{\sqrt{Re_x}} \quad (\text{A.2.5})$$

Appendix B

Additional Results

B.1 Additional y^+ Value Verification

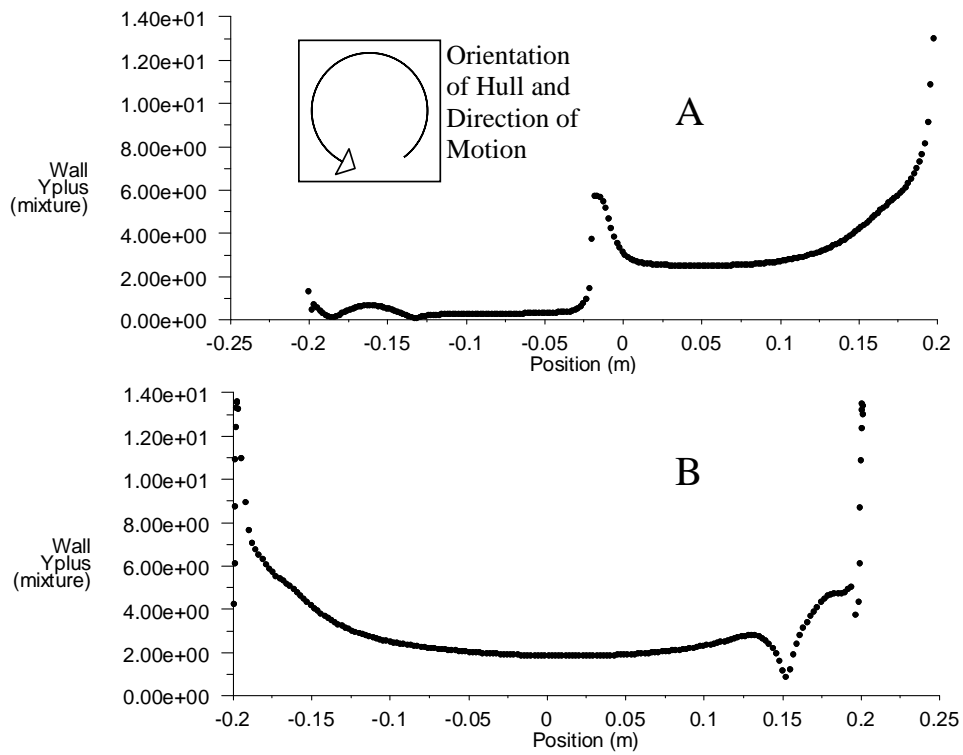


Figure B.1: y^+ values of the hull at time step $t = 25.411378$ s along A: the starboard side surface B: the bottom side surface

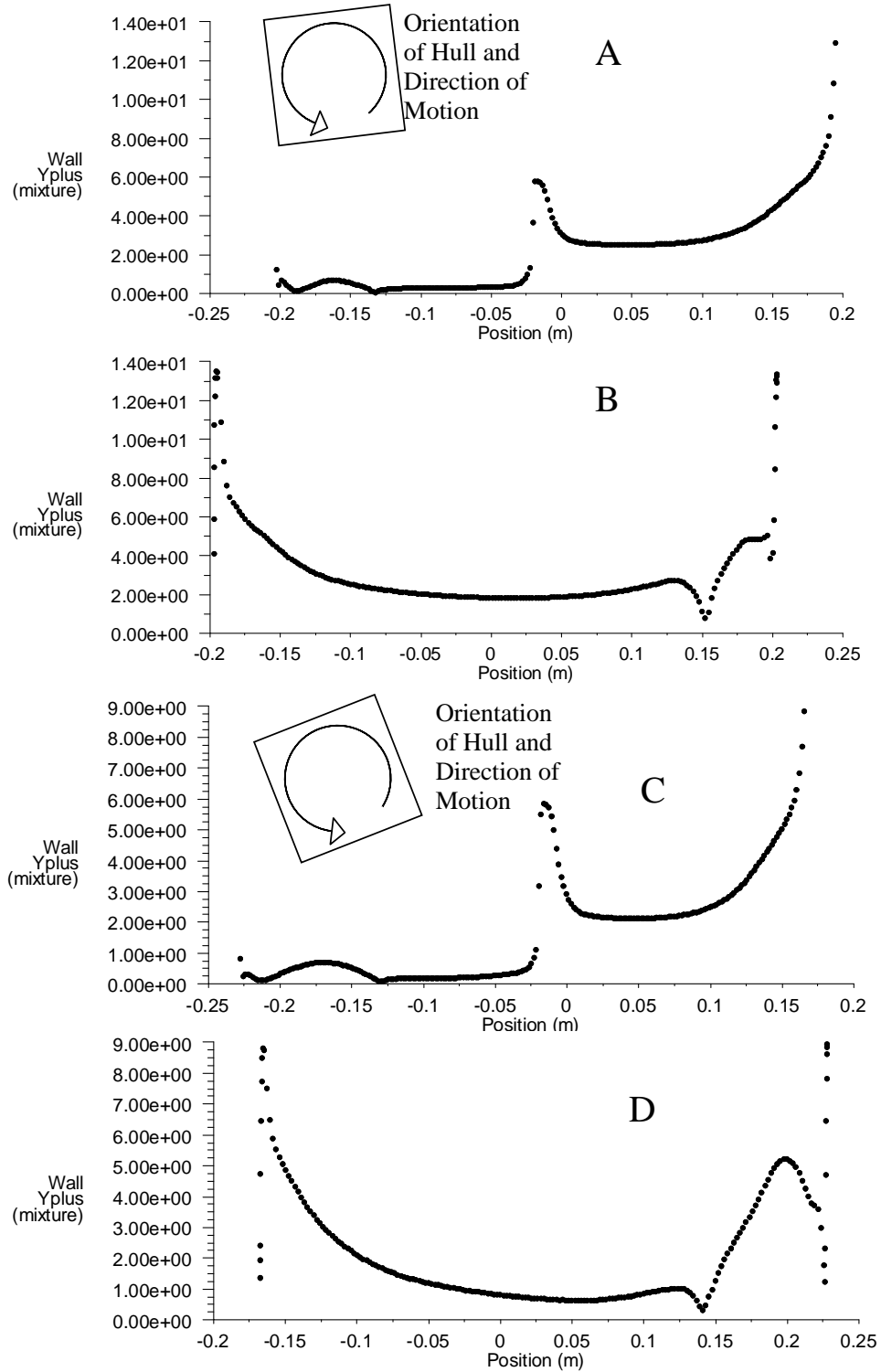


Figure B.2: y^+ values of the hull at time step $t = 25.571199$ s along A: the starboard side surface B: the bottom side surface. $-y^+$ values of the hull at time step $t = 25.73102$ s along C: the starboard side surface D: the bottom side surface

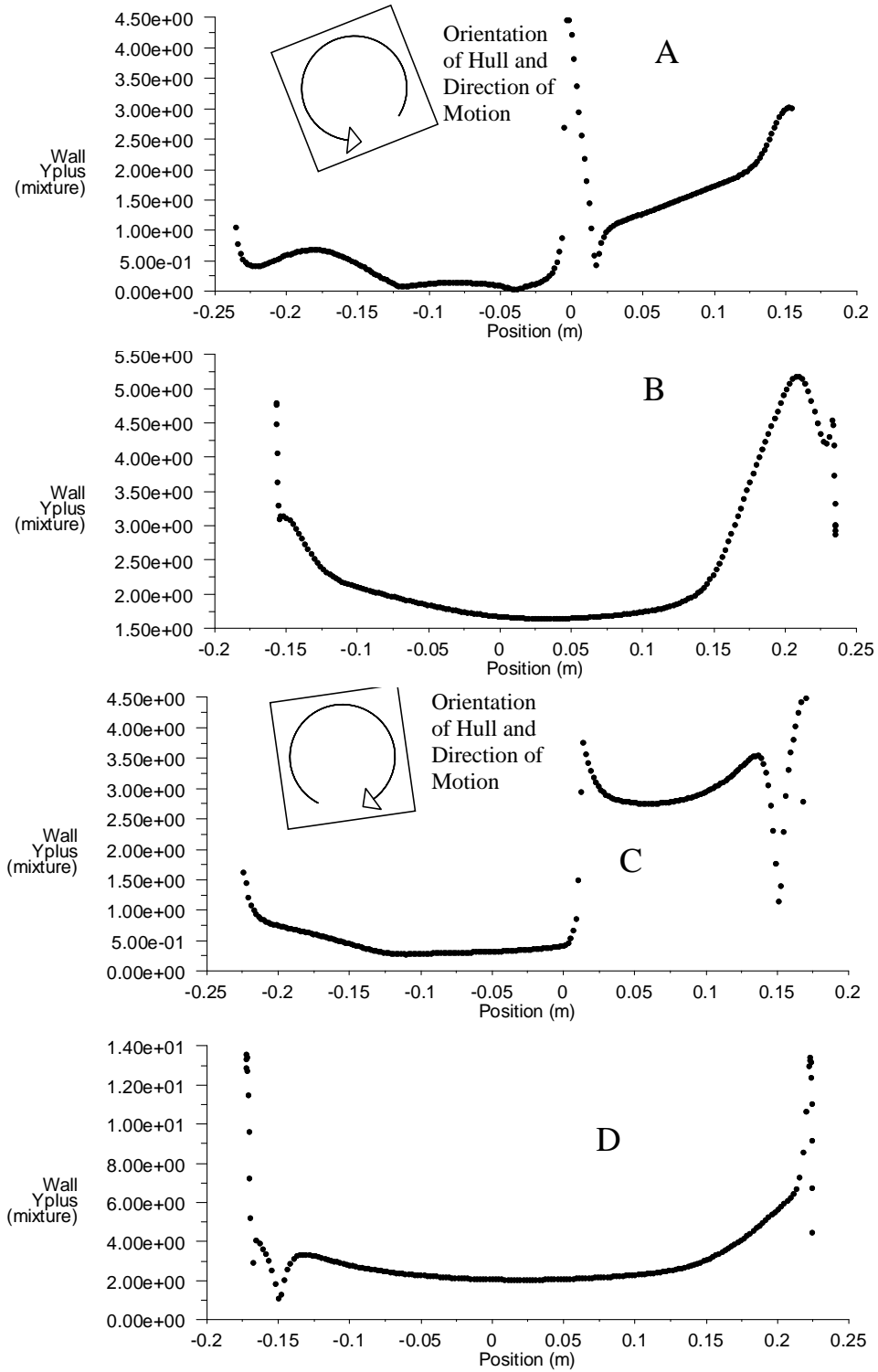


Figure B.3: y^+ values of the hull at time step $t = 25.890841$ s along C: the starboard side surface D: the bottom side surface. $-y^+$ values of the hull at time step $t = 26.050659$ s along A: the starboard side surface B: the bottom side surface

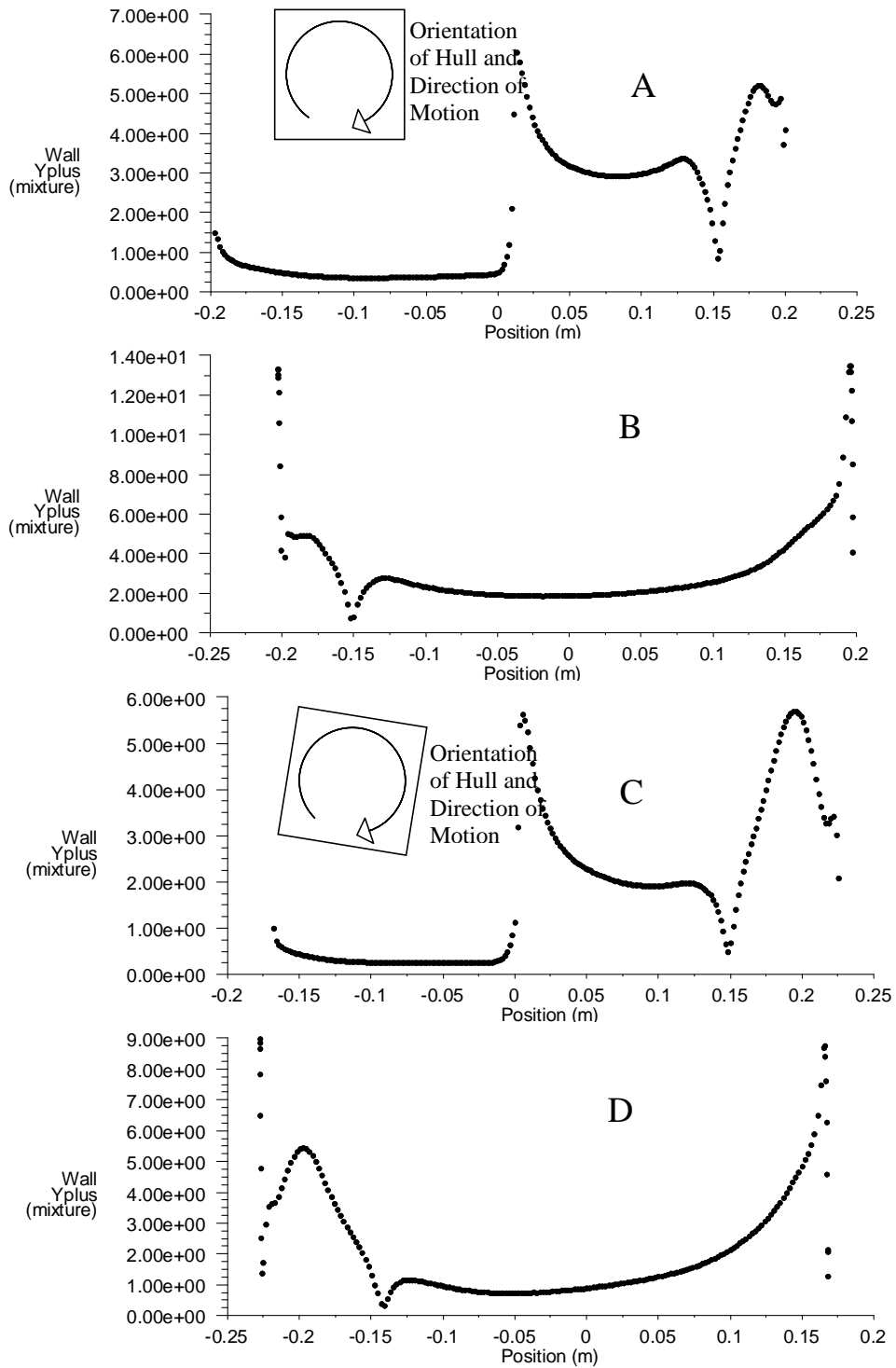


Figure B.4: y^+ values of the hull at time step $t = 26.21048$ s along C: the starboard side surface D: the bottom side surface. $-y^+$ values of the hull at time step $t = 26.3703$ s along A: the starboard side surface B: the bottom side surface

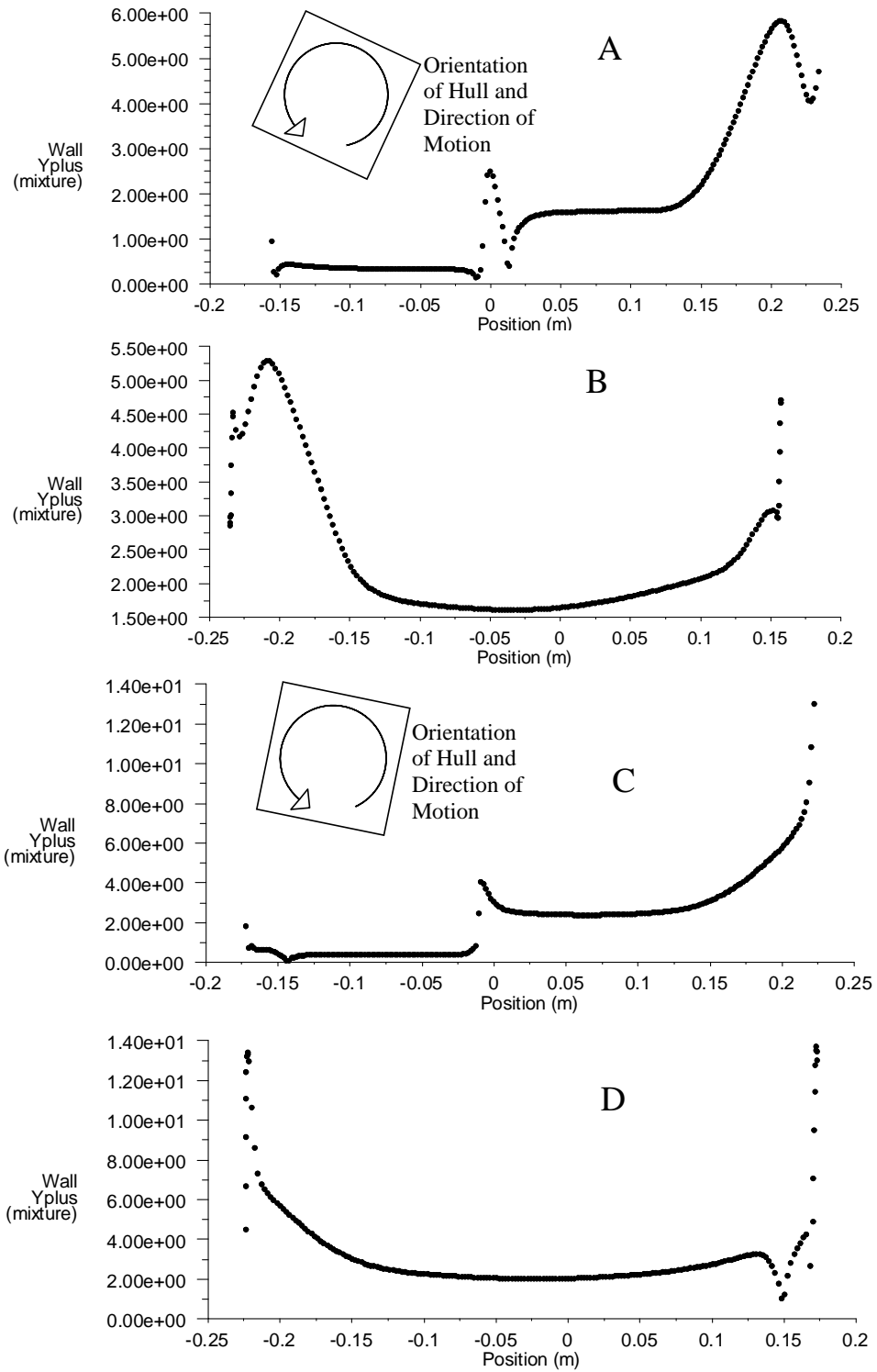


Figure B.5: y^+ values of the hull at time step $t = 26.530121$ s along C: the starboard side surface D: the bottom side surface. $-y^+$ values of the hull at time step $t = 26.689939$ s along A: the starboard side surface B: the bottom side surface

B.2 Additional Amplitude Plots

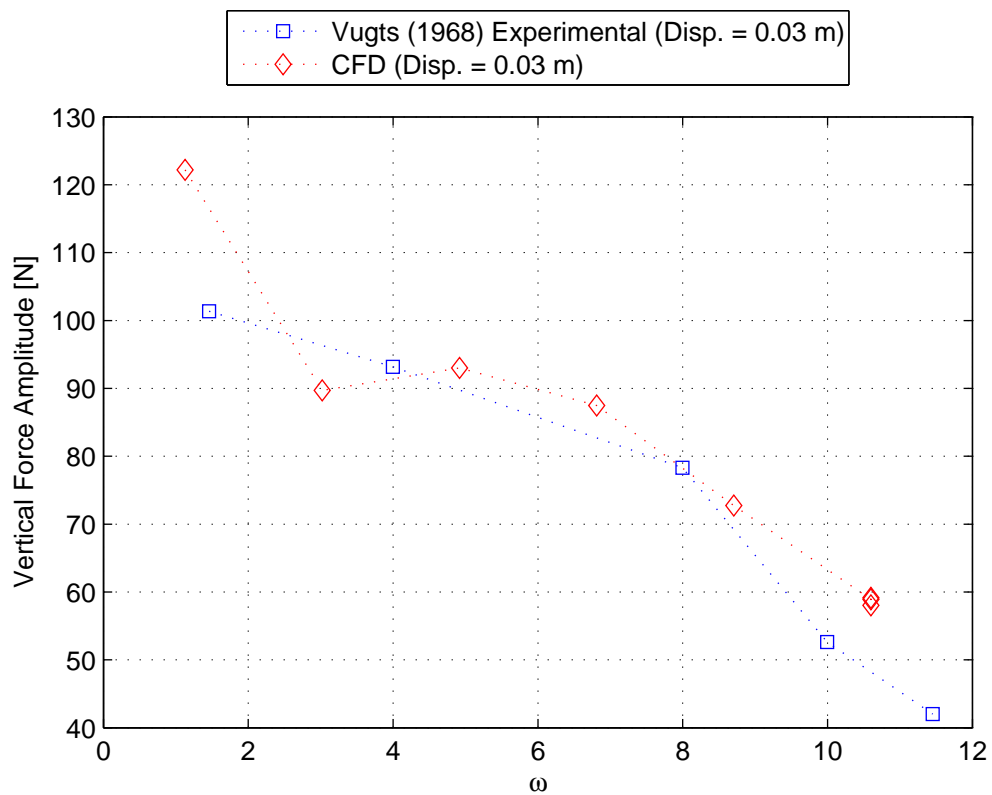


Figure B.6: Force amplitude of a v-bottom hull in heave versus oscillation frequency presented by Vugts (1968) and force amplitude obtained with CFD (FLUENT, 2009)

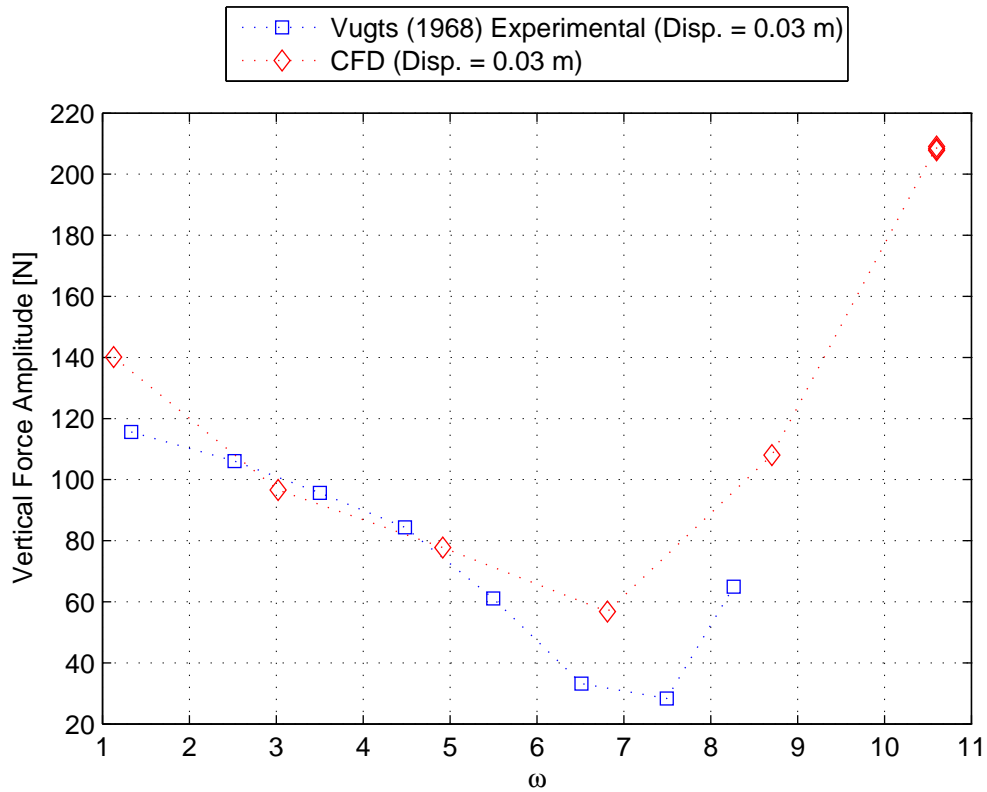


Figure B.7: Force amplitude of a flat-bottom hull in heave versus oscillation frequency presented by Vugts (1968) and force amplitude obtained with CFD (FLUENT, 2009)

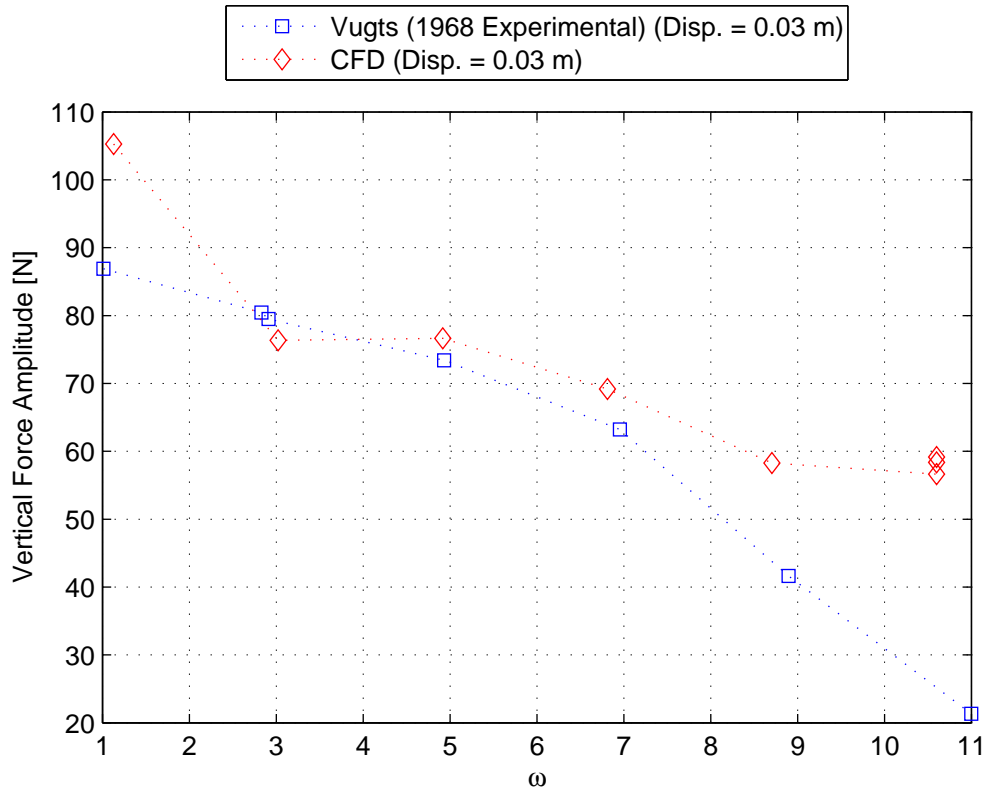


Figure B.8: Force amplitude of a round-bottom hull in heave versus oscillation frequency presented by Vugts (1968) and force amplitude obtained with CFD (FLUENT, 2009)

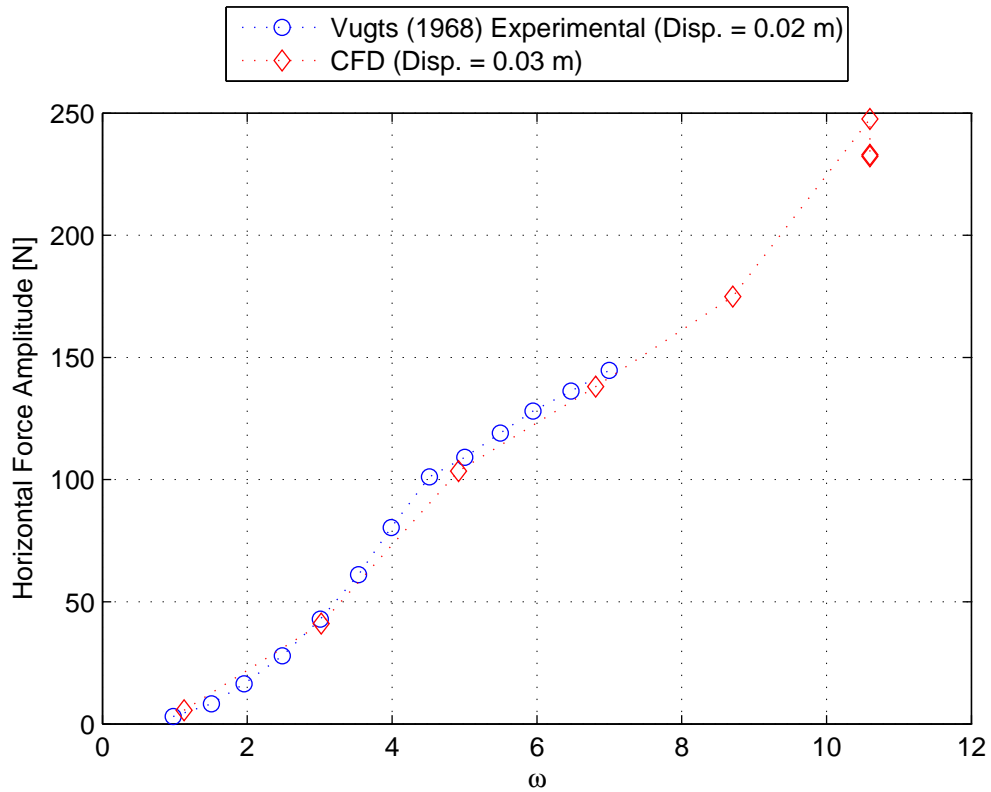


Figure B.9: Force amplitude of a v-bottom hull in sway versus oscillation frequency presented by Vugts (1968) and force amplitude obtained with CFD (FLUENT, 2009)

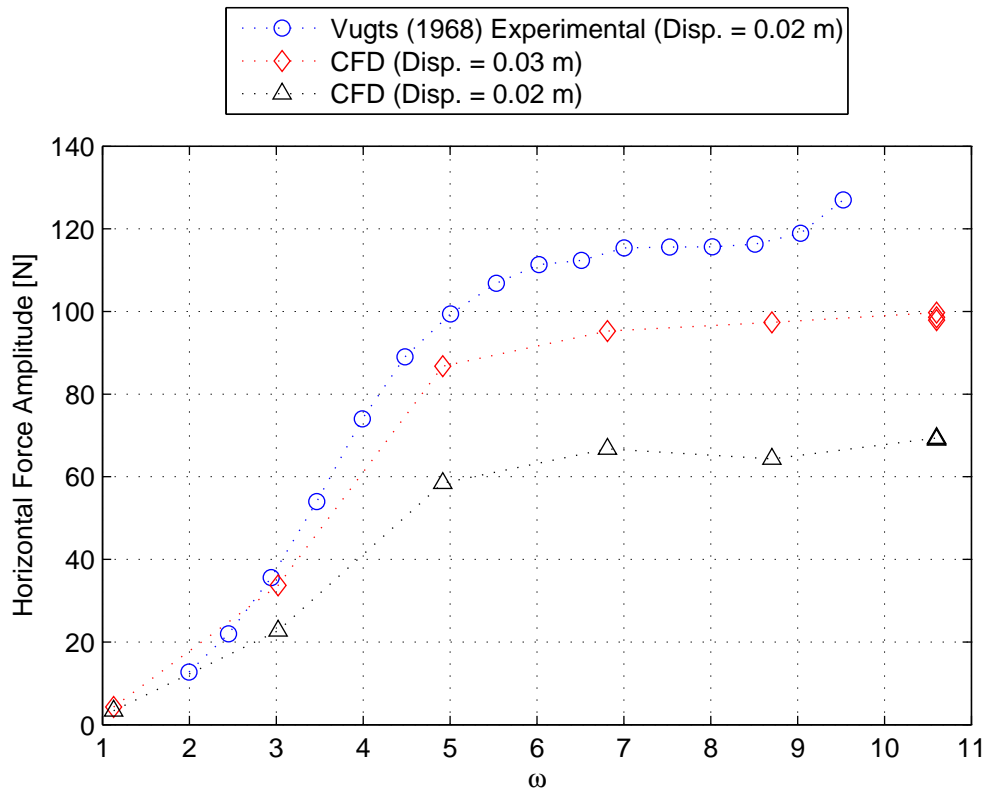


Figure B.10: Force amplitude of a flat-bottom hull in sway versus oscillation frequency presented by Vugts (1968) and force amplitude obtained with CFD (FLUENT, 2009)

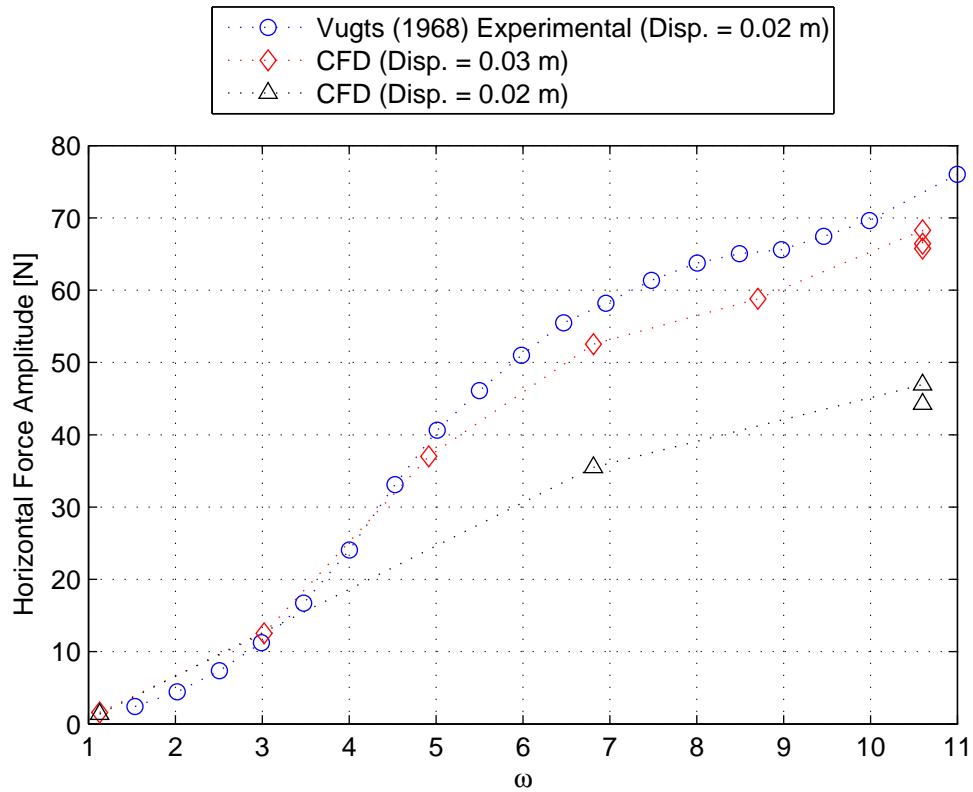


Figure B.11: Force amplitude of a round-bottom hull in sway versus oscillation frequency presented by Vugts (1968) and force amplitude obtained with CFD (FLUENT, 2009)

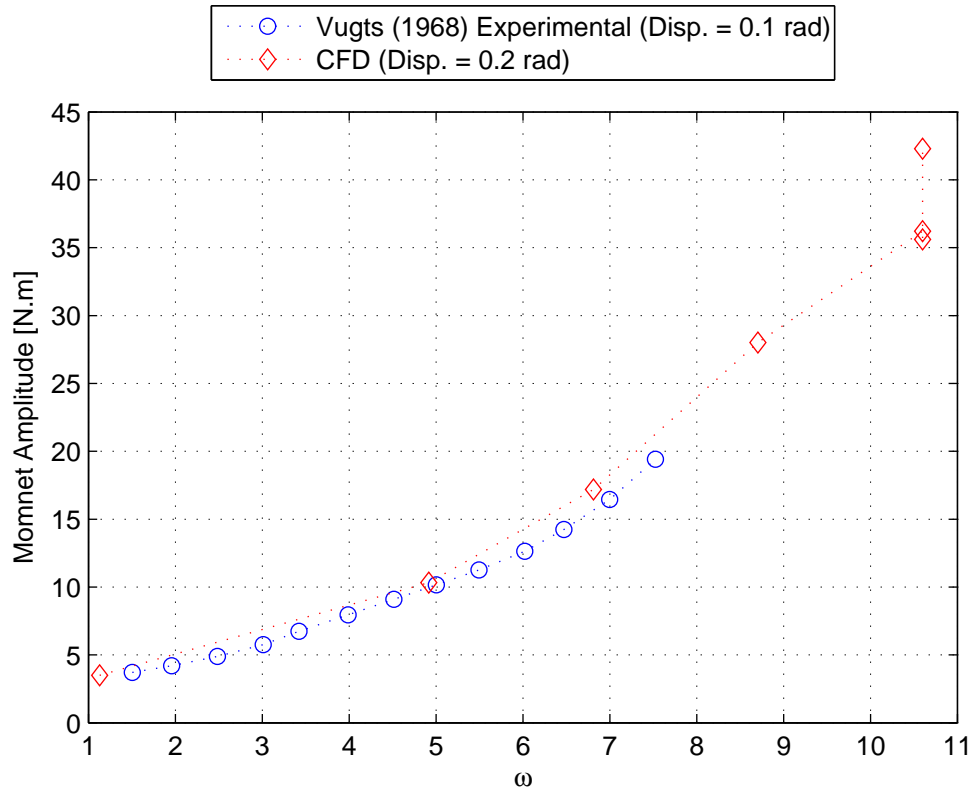


Figure B.12: Moment amplitude of a v-bottom hull in roll versus oscillation frequency presented by Vugts (1968) and moment amplitude obtained with CFD (FLUENT, 2009)

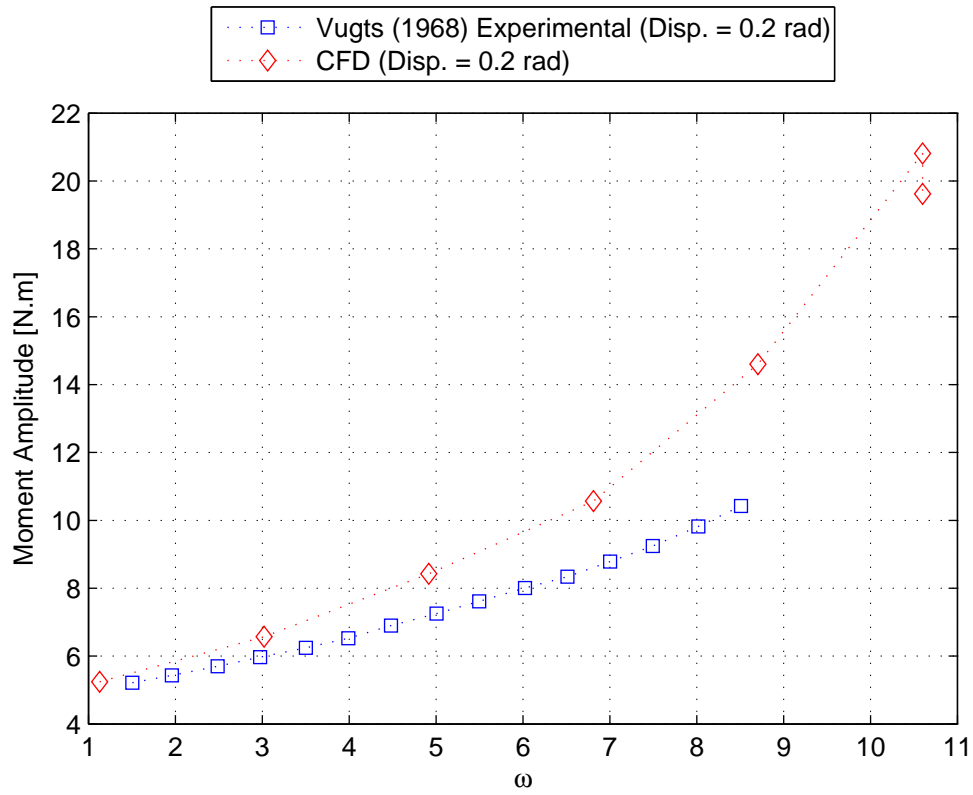


Figure B.13: Moment amplitude of a flat-bottom hull in roll versus oscillation frequency presented by Vugts (1968) and moment amplitude obtained with CFD (FLUENT, 2009)

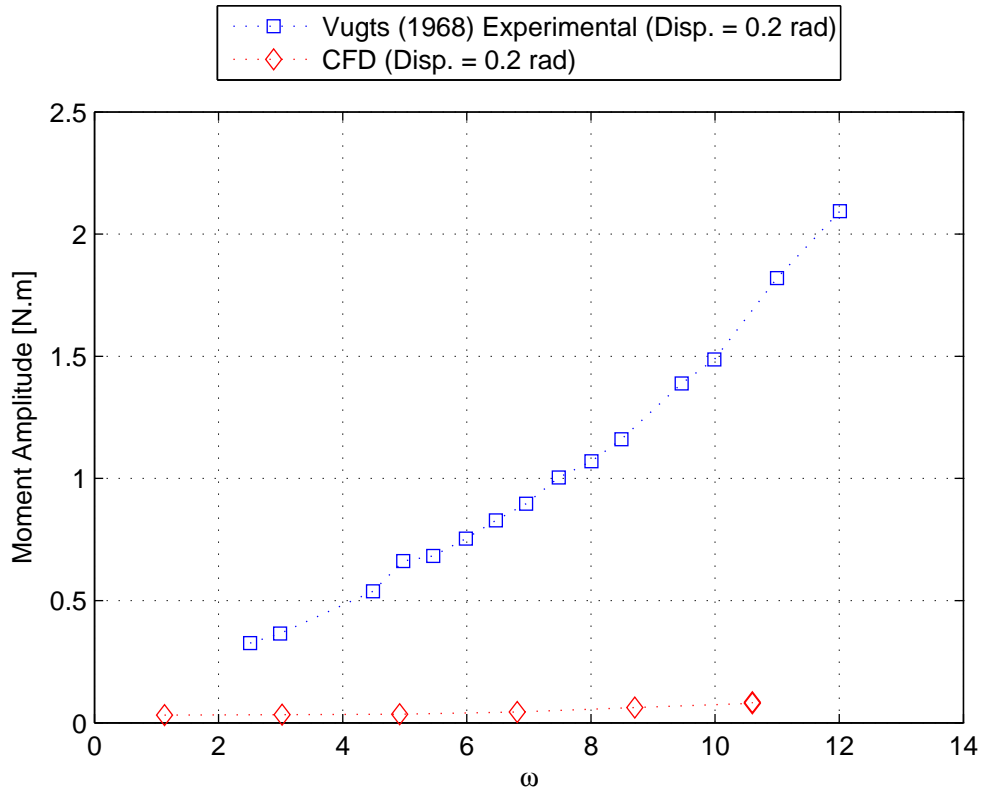


Figure B.14: Moment amplitude of a round-bottom hull in roll versus oscillation frequency presented by Vugts (1968) and moment amplitude obtained with CFD (FLUENT, 2009)

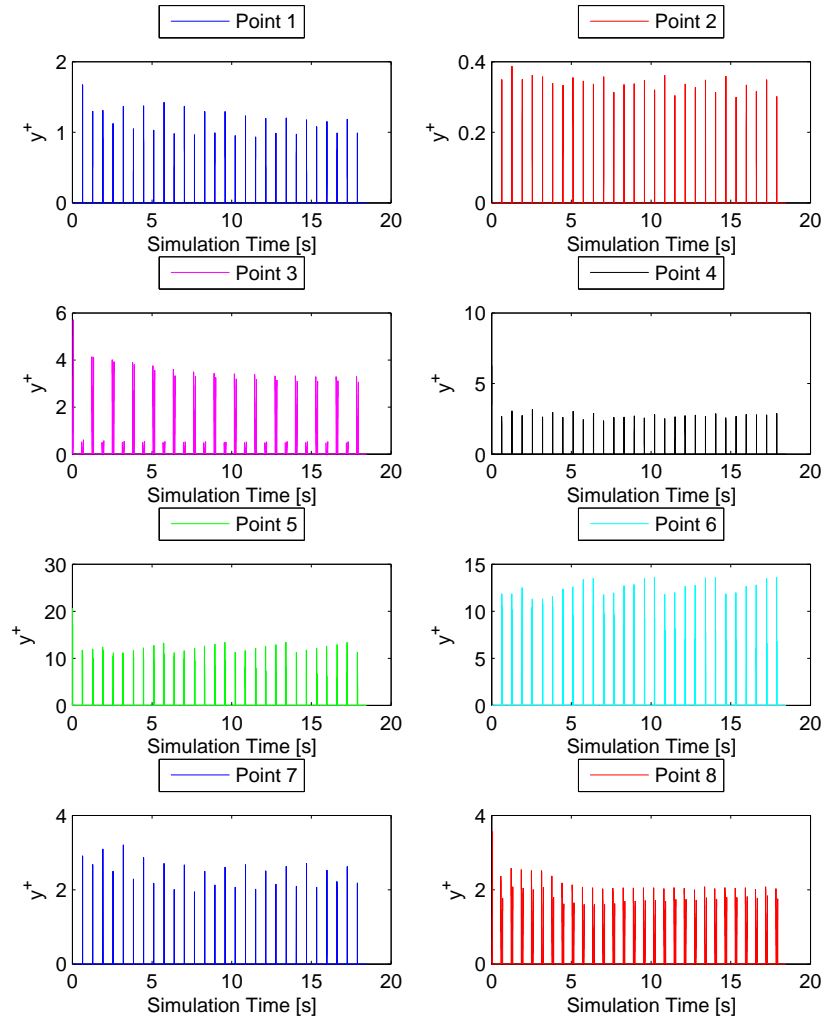


Figure B.15: y^+ values at 8 different points 0.03 mm from the hull surface

Appendix C

Additional Tables

C.1 Transition SST constants

Table C.1: Transition SST model constants

Constant name	Description	Value
Alpha*_inf	NA	1
Alpha_inf	NA	0.52
Beta*_inf	Turbulent kinetic energy constant	0.09
a1	Constant for modelling the effective diffusivity	0.31
Beta_i(Inner)	Turbulent kinetic energy constant	0.075
Beta_i(Outer)	Turbulent kinetic energy constant	0.0828
Ca1	Turbulence viscosity constant	2
Ca2	Turbulence viscosity constant	0.06
Ce1	Intermittency equation constant	1
Ce2	Intermittency equation constant	50
C_thetat	Transition momentum thickness Re constant	0.03
C_s1	Transition momentum thickness Re constant	2
TKE (Inner) Prandtl #	NA	1.176
TKE (Outer) Prandtl #	NA	1
SDR (Inner) Prandtl #	NA	2
SDR (Outer) Prandtl #	NA	1.168
Intermit. Prandtl #	NA	1
Re_theta. Prandtl #	NA	2

C.2 y^+ Monitor Values for Hull Surfaces

Table C.2: y^+ monitor values for hull sides in heave

Hull shape	Mesh	Osc. frequency	Hull region	y_{avg}^+	y_{max}^+
V-bottom	Coarse	10.599	Starboard	12	23
			Top	18	23
	Medium	10.599	Starboard	8	16
			Top	14.5	25
	Fine	1.129	Starboard	0.7	3.5
			Top	1.8	4
		3.023	Starboard	1.4	4.5
			Top	3.3	6.5
		4.917	Starboard	2.4	6
			Top	5	11
		6.811	Starboard	3.5	7.5
			Top	6.7	16
		8.705	Starboard	4.5	7.5
			Top	6.7	16
	10.599	Starboard	6	11	
		Top	9	22	
Flat-bottom	Coarse	10.599	Starboard	8.2	29
			Bottom	12	33
	Medium	10.599	Starboard	5.8	21.4
			Bottom	10	26.1
	Fine	1.129	Starboard	0.7	3.4
			Bottom	1.3	3.9
		3.023	Starboard	1.4	6.6
			Bottom	2.6	7.3
		4.917	Starboard	2.4	10.2
			Bottom	5	11
		6.811	Starboard	3.3	13
			Bottom	5.4	15.6
		8.705	Starboard	4	15.2
			Bottom	6.5	18.7
	10.599	Starboard	4.6	17.4	
		Bottom	7.5	21.7	
Round-bottom	Coarse	10.599	Starboard	5.3	15.3
			Bottom	15.3	18.9
	Medium	10.599	Starboard	3.6	11.3
			Bottom	11.7	15
	Fine	1.129	Starboard	0.4	2.6
			Bottom	1.5	2.8
		3.023	Starboard	0.7	3.8
			Bottom	2.9	4.2
		4.917	Starboard	1.1	5.6
			Bottom	4.7	6.7
		6.811	Starboard	1.7	7.1
			Bottom	6.5	8.7
		8.705	Starboard	2.3	8
			Bottom	8	10.4
	10.599	Starboard	2.9	8.6	
		Bottom	9.3	11.8	

Table C.3: y^+ monitor values for hull sides in sway

Hull shape	Mesh	Osc. frequency	Hull region	y_{avg}^+	y_{max}^+		
V-bottom	Coarse	10.599	Starboard	9	37		
			Port	9	37		
	Medium	1.129	3.023	Starboard	1.2	7	
				Port	1.2	8	
		4.917	Starboard	3	12		
			Port	2.7	13		
		6.811	Starboard	4	16		
			Port	4	16		
		8.705	Starboard	4	22		
			Port	4	20		
		10.599	Starboard	5.5	23		
			Port	5.5	23		
		Fine	10.599	Starboard	4.5	21	
				Port	4.5	21	
					Starboard	6.5	27
					Port	6.5	26.5
Flat-bottom	Coarse	10.599	Port	6.5	11.9		
			Bottom	14.4	18.9		
	Medium	10.599	Port	4.5	11.3		
			Bottom	8.7	14.8		
	Fine	1.129	3.023	Port	0.4	3.3	
				Bottom	1.2	3.7	
		4.917	Port	1.1	6.9		
			Bottom	2.8	7.8		
		6.811	Port	2	8.4		
			Bottom	4.1	10.4		
		8.705	Port	2	6.8		
			Bottom	4.5	10.2		
		10.599	Port	2.8	7.9		
			Bottom	5.7	11.1		
					Port	3.4	9.6
					Bottom	6.7	12.5
Round-bottom		Coarse	10.599	Port	14	32.5	
				Bottom	28.7	42.6	
	Medium	10.599	Port	9.9	22.8		
			Bottom	19	28.2		
	Fine	1.129	3.023	Port	0.3	1.1	
				Bottom	2.9	3.9	
		4.917	Port	0.8	3		
			Bottom	7	9.1		
		6.811	Port	1.9	7.9		
			Bottom	10	12.4		
		8.705	Port	3.6	12.4		
			Bottom	10.8	14.6		
		10.599	Port	5.14	15.1		
			Bottom	11.1	16.9		
					Port	6.7	15.9
					Bottom	12.8	19.5

Table C.4: y^+ monitor values for hull sides in roll

Hull shape	Mesh	Osc. frequency	Hull region	y_{avg}^+	y_{max}^+	
V-bottom	Coarse	10.599	Total	8	44	
		10.599	Total	5.9	40.7	
	Fine	1.129	Total	0.9	6.1	
		3.023	Total	1.6	13.3	
		4.917	Total	2.3	16.2	
		6.811	Total	2.8	20.3	
		8.705	Total	3.6	25	
		10.599	Total	4.5	27.8	
Flat-bottom	Coarse	10.599	Port	5.6	36	
			Bottom	13.5	40.5	
	Medium	1.129	Port	0.9	5.4	
			Bottom	1.6	5.8	
		3.023	Port	2	11.5	
			Bottom	3.8	12.9	
		4.917	Port	2.8	14.9	
			Bottom	5.11	16.9	
		6.811	Port	3.1	18.2	
			Bottom	6.5	20.9	
		8.705	Port	3.6	22.4	
			Bottom	8.1	26	
		10.599	Port	3.2	20.8	
			Bottom	7	25	
		Fine	10.599	Port	4	26.5
				Bottom	9.5	30.9
Round-bottom	Medium	10.599	Port	4.8	22.4	
			Bottom	20	21.7	
	Fine	1.129	Port	1	5.7	
			Bottom	3.9	5.6	
		3.023	Port	2.1	9	
			Bottom	8	9.2	
		4.917	Port	2.7	12.2	
			Bottom	10.8	12.4	
		6.811	Port	3.3	15.4	
			Bottom	13.6	15	
		8.705	Port	4.2	18.9	
			Bottom	17.25	19.5	
		10.599	Port	3.2	15.2	
			Bottom	13.6	15.7	

Table C.5: y^+ monitor values for hull sides with medium displacement in sway

Hull shape	Mesh	Osc. frequency	Hull region	y_{avg}^+	y_{max}^+
Flat-bottom	Coarse	10.599	Port	5.1	11.7
			Bottom	9.5	14.5
	Medium	10.599	Port	3.5	8.9
			Bottom	6.9	11.5
	Fine	1.129	Port	0.3	2.4
			Bottom	1.1	3.3
		3.023	Port	0.9	5.4
			Bottom	2.2	6
		4.917	Port	1.5	6.2
			Bottom	3.1	7.8
		6.811	Port	1.9	5.7
			Bottom	3.7	7.9
		8.705	Port	2.3	6.4
			Bottom	4.2	8.5
10.599	Port	2.7	7.4		
	Bottom	5	9.9		
Round-bottom	Coarse	10.599	Port	10.3	29.3
			Bottom	23.6	33.7
	Fine	1.129	Port	0.2	1
			Bottom	2.9	3.8
		6.811	Port	2.5	10
			Bottom	9	11.3
10.599	Port	4.7	14.8		
	Bottom	10.4	14.9		

C.3 Amplitude and Phase Angle Errors

Table C.6: Errors determined for each computational mesh fineness for the heave cases

Heave		
V-bottom hull		
Amplitude error ($p = 1$)		
Coarse	Medium	Fine
4.75%	3.17%	
Phase angle difference ($p = 1$)		
Coarse	Medium	Fine
-2.848	-1.900	
Flat-bottom hull		
Amplitude error ($p = 1.07$)		
Coarse	Medium	Fine
1.02%	0.66%	0.43%
Phase angle difference ($p = 1.76$)		
Coarse	Medium	Fine
0.658	0.322	0.157
Round-bottom hull		
Amplitude error ($p = 1.98$)		
Coarse	Medium	Fine
5.29%	2.37%	1.06%
Phase angle difference ($p = 12.89$)		
Coarse	Medium	Fine
2.995	0.0162	0.000

Table C.7: Errors determined for each computational mesh fineness for the sway cases

Sway		
V-bottom hull ($p = 8.07$)		
Amplitude error		
Coarse	Medium	Fine
6.57%	0.25%	0.01%
Phase angle difference ($p = 11.09$)		
Coarse	Medium	Fine
2.281	0.026	0.000
Flat-bottom hull ($p = 1.25$)		
Amplitude error		
Coarse	Medium	Fine
2.98%	1.80%	1.09%
Phase angle difference ($p = 4.17$)		
Coarse	Medium	Fine
-1.181	-0.219	0.040
Round-bottom hull		
Amplitude error ($p = 2.42$)		
Coarse	Medium	Fine
4.46%	1.67%	0.63%
Phase angle difference ($p = 2.71$)		
Coarse	Medium	Fine
-1.151	-0.384	-0.128

Table C.8: Errors determined for each computational mesh fineness for the roll cases

Roll		
V-bottom hull		
Amplitude error ($p = 1$)		
Coarse	Medium	Fine
5.19%	3.46%	
Phase angle difference ($p = 1$)		
Coarse	Medium	Fine
-1.316	-0.878	
Flat-bottom hull		
Amplitude error ($p = 1$)		
Coarse	Medium	Fine
	20.79%	13.87%
Phase angle difference ($p = 1$)		
Coarse	Medium	Fine
	6.230	4.155
Round-bottom hull		
Amplitude error ($p = 1$)		
Coarse	Medium	Fine
15.83%	10.56%	
Phase angle difference ($p = 1$)		
Coarse	Medium	Fine
5.451	3.639	

Appendix D

Additional Grid Seeding Figures and Tables

D.1 Seeding of Domain Edges

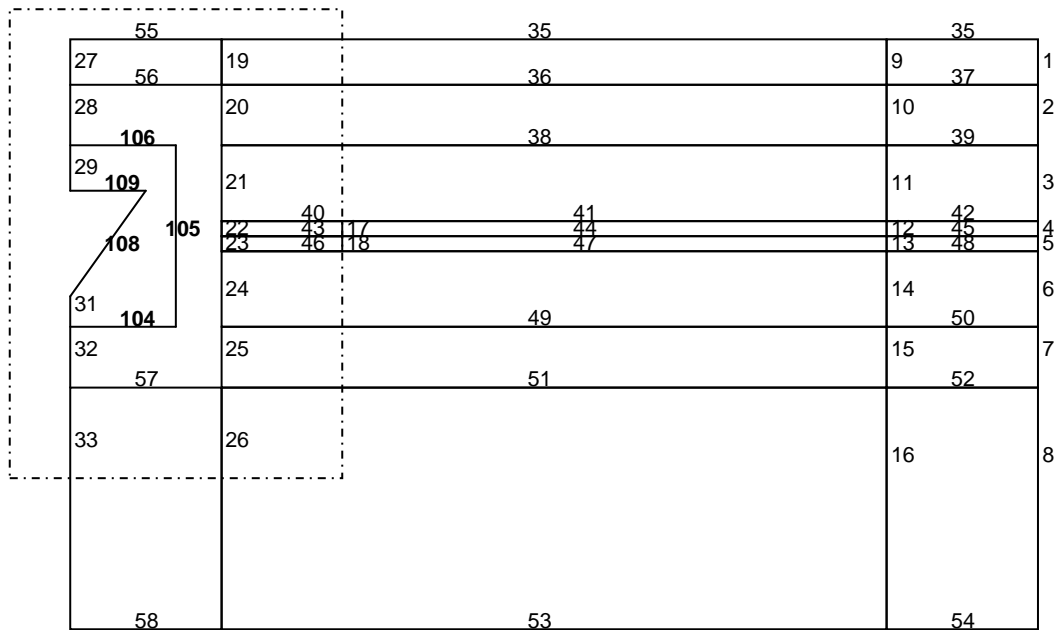


Figure D.1: Schematic (not to scale) of the computational domain v-bottom heave case numbered edges used for grid seeding (table D.1)

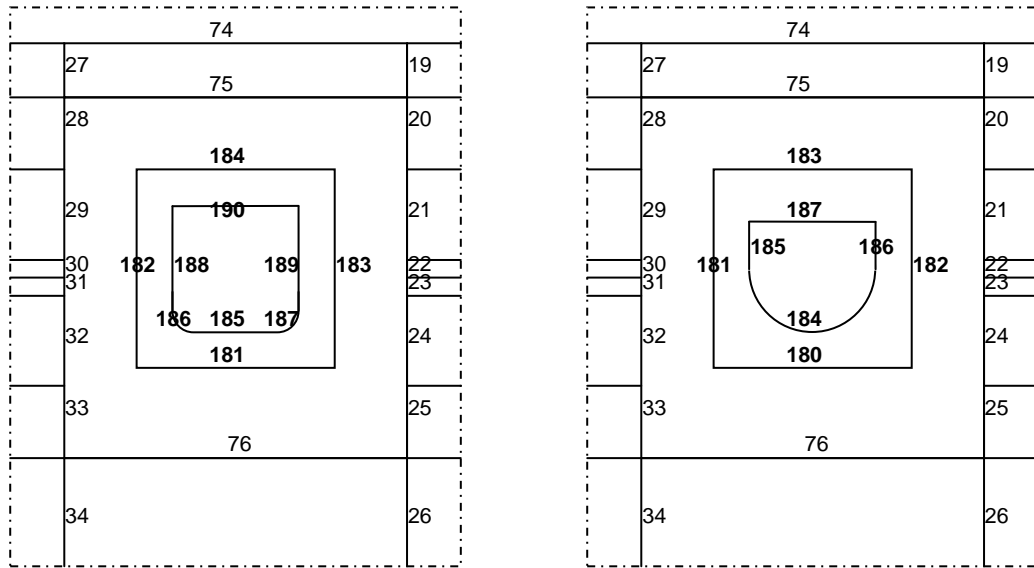


Figure D.2: Schematic(not to scale) of the computational domain flat- and round-bottom heave case regions adapted from figure D.1, with numbered edges used for grid seeding (tables D.2 and D.3)

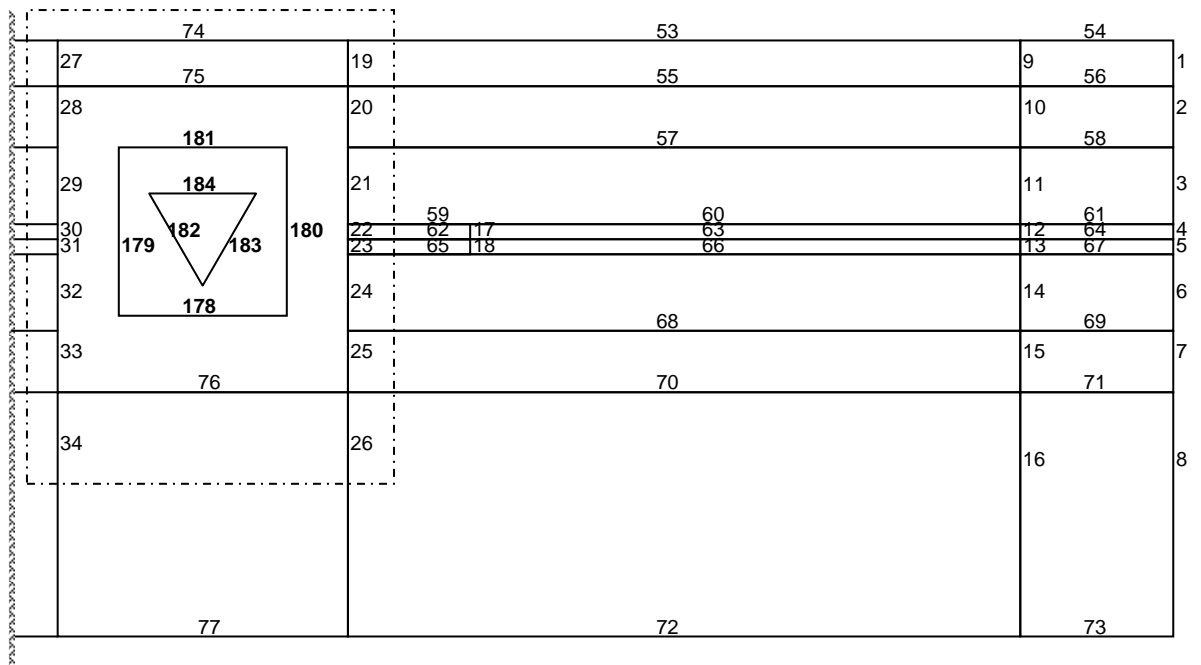


Figure D.3: Schematic (not to scale) of the computational domain v-bottom sway case numbered edges used for grid seeding (table D.4)

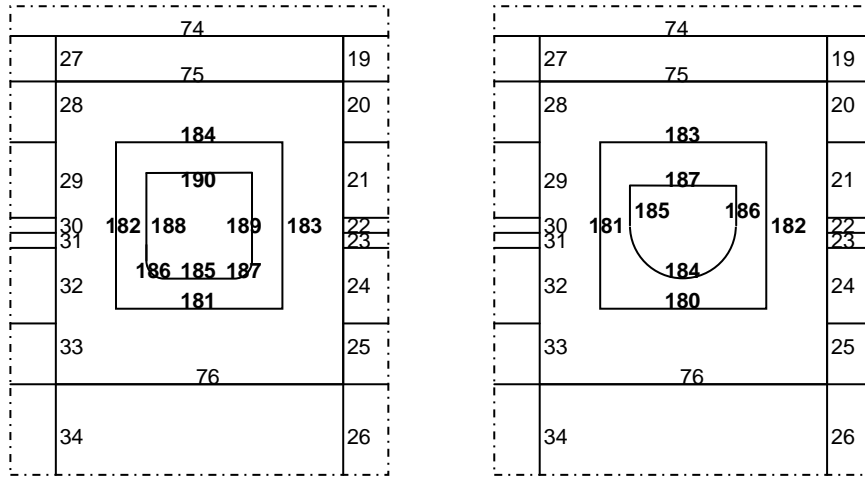


Figure D.4: Schematic (not to scale) of the computational domain flat- and round-bottom sway case regions adapted from figure D.3, with numbered edges used for grid seeding (tables D.5 and D.6)

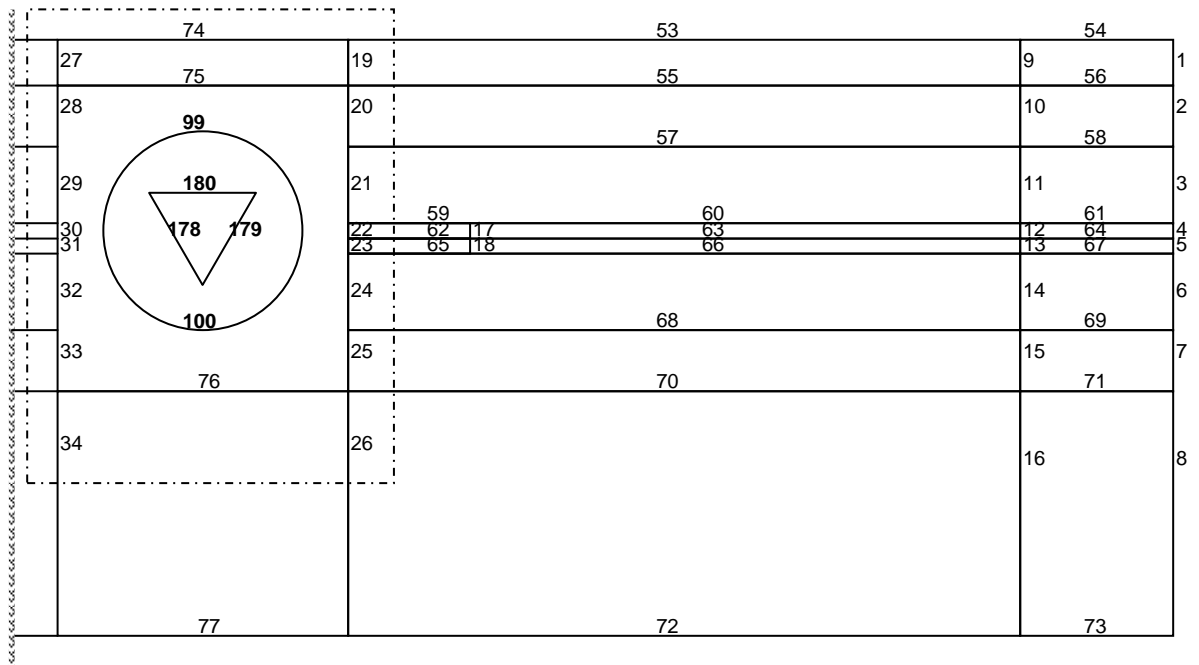


Figure D.5: Schematic (not to scale) of the computational domain v-bottom roll case numbered edges used for grid seeding (table D.7)

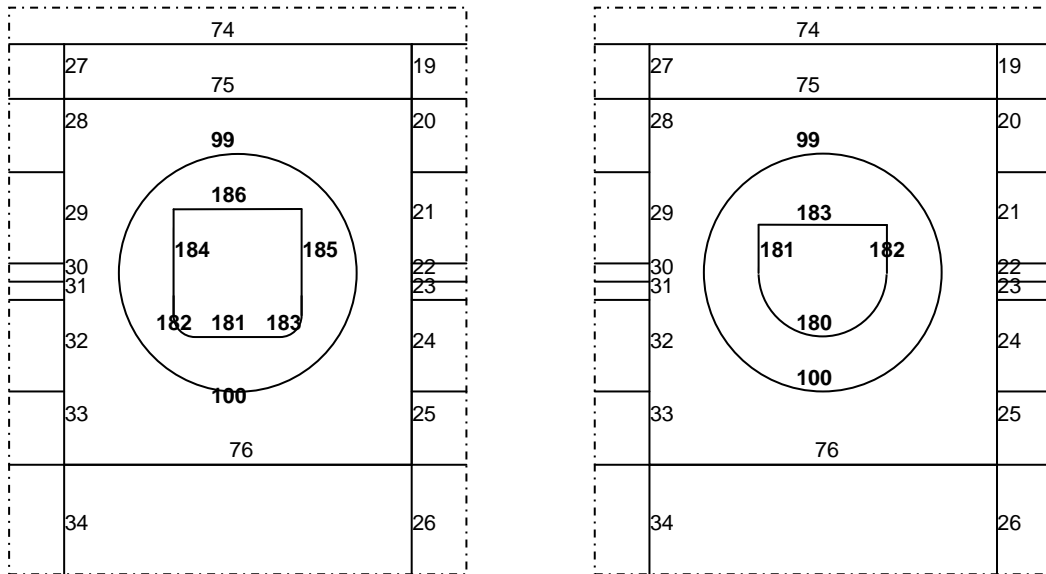


Figure D.6: Schematic (not to scale) of the computational domain flat- and round-bottom roll case regions adapted from figure D.5, with numbered edges used for grid seeding (tables D.8 and D.9)

D.2 Domain Edge Seeding Details

Table D.1: V-bottom heave mesh seeding summary

Edge	Ratio			Intervals		
	Coarse	Medium	Fine	Coarse	Medium	Fine
1, 9, 19, 27	1	1	1	3	3	3
2, 10, 20, 7, 15, 25	1	1	1	5	8	8
8, 16, 26, 33	1	1	1	20	20	20
24, 21, 11, 14	1	1	1	10	16	24
3, 6	0.95	0.95	0.95	14	22	34
5, 4, 23, 22	1	1	1	4	6	10
13, 12, 18, 17	1	1	1	2	4	6
28, 32	1	1	1	7	11	17
55, 56, 57, 58	1	1	1	12	18	26
34, 36, 38, 49, 51, 53	1	1	1	100	100	100
41, 44, 47	1	1	1	86	130	196
35, 37, 39, 50, 52, 54	1	1	1	14	22	22
40, 43, 46	1.0526	1.03	1.01	24	40	60
42, 45, 48	0.95	0.97	0.99	24	40	60
105	0.95-0.95	0.95-0.95	0.95-0.95	27	40	60
106	1	1	1	10	14	22
104	1.1	1.05	1.05	15	22	34
29	0.9	0.9	0.9	14	20	30
31	1.2	1.13	1.08	15	22	34
108	0.999-0.999	0.999-0.999	0.999-0.999	300	450	680
109	1	1	1	21	32	48

Table D.2: Flat-bottom heave mesh seeding summary

Edge	Ratio			Intervals		
	Coarse	Medium	Fine	Coarse	Medium	Fine
1, 9, 19, 27	1	1	1	3	3	3
2, 10, 20, 7, 15, 25	1	1	1	5	8	8
8, 16, 26, 33	1	1	1	20	20	20
24, 21, 11, 14	1	1	1	10	16	24
3,6	0.95	0.95	0.95	14	22	34
5, 4, 23, 22	1	1	1	4	6	10
13, 12, 18, 17	1	1	1	2	4	6
28, 32	1	1	1	7	11	17
55, 56, 57, 58	1	1	1	12	18	26
34, 36, 38, 49, 51, 53	1	1	1	100	100	100
41, 44, 47	1	1	1	86	130	196
35, 37, 39, 50, 52, 54	1	1	1	14	22	22
40, 43, 46	1.0526	1.03	1.01	24	40	60
42, 45, 48	0.95	0.97	0.99	24	40	60
106	1.1	1.05	1.05	15	20	33
107	0.95-0.95	0.95-0.95	0.95-0.95	27	40	60
108	1	1	1	10	14	22
29	0.9	0.9	0.9	14	20	30
31	1.14	1.06	1.04	20	30	45
113	1	1	1	25	35	50
112	1	1	1	250	375	560
110	1	1	1	100	150	225
111	1	1	1	5	7	10

Table D.3: Round-bottom heave mesh seeding summary

Edge	Ratio			Intervals		
	Coarse	Medium	Fine	Coarse	Medium	Fine
1, 9, 19, 27	1	1	1	3	3	3
2, 10, 20, 7, 15, 25	1	1	1	5	8	8
8, 16, 26, 33	1	1	1	20	20	20
24, 21, 11, 14	1	1	1	10	16	24
3,6	0.95	0.95	0.95	14	22	34
5, 4, 23, 22	1	1	1	4	6	10
13, 12, 18, 17	1	1	1	2	4	6
28, 32	1	1	1	7	11	17
55, 56, 57, 58	1	1	1	12	18	26
34, 36, 38, 49, 51, 53	1	1	1	100	100	100
41, 44, 47	1	1	1	86	130	196
35, 37, 39, 50, 52, 54	1	1	1	14	22	22
40, 43, 46	1.0526	1.03	1.01	24	40	60
42, 45, 48	0.95	0.97	0.99	24	40	60
105	1.1	1.05	1.05	15	22	34
106	0.95-0.95	0.95-0.95	0.95-0.95	24	40	60
107	1	1		10	14	22
29	0.9	0.9	0.9	14	20	30
31	1.1	1.07	1.035	30	40	67
109	1	1	1	125	185	275
110	1	1	1	50	75	115
111	1	1	1	20	30	45

Table D.4: V-bottom sway mesh seeding summary

Edge	Ratio			Intervals		
	Coarse	Medium	Fine	Coarse	Medium	Fine
74, 75, 76, 77	1	1	1	25	36	54
179, 180	0.95-0.95	0.95-0.95	0.95-0.95	27	40	60
178, 181	1	1	1	20	28	44
182, 183	0.999-0.999	0.999-0.999	0.999-0.999	300	450	680
184	1	1	1	48	64	96

Table D.5: Flat-bottom sway mesh seeding summary

Edge	Ratio			Intervals		
	Coarse	Medium	Fine	Coarse	Medium	Fine
74, 75, 76, 77	1	1	1	25	36	54
182, 183	0.95-0.95	0.95-0.95	0.95-0.95	27	41	62
181, 184	1	1	1	20	30	45
190	1	1	1	40	60	90
188, 189	1	1	1	99	150	225
185	1	1	1	84	120	180
186, 187	1	1	1	5	8	8

Table D.6: Round-bottom sway mesh seeding summary

Edge	Ratio			Intervals		
	Coarse	Medium	Fine	Coarse	Medium	Fine
74, 75, 76, 77	1	1	1	25	36	54
181, 182	0.95-0.95	0.95-0.95	0.95-0.95	27	41	62
180, 183	1	1	1	20	30	45
185, 186	1	1	1	21	30	45
184	1	1	1	99	150	225
187	1	1	1	27	42	60

Table D.7: V-bottom roll mesh seeding summary

Edge	Ratio			Intervals		
	Coarse	Medium	Fine	Coarse	Medium	Fine
74, 75, 76, 77	1	1	1	25	36	54
99, 100	10.52-1.052	1.04-1.04	1.04	60	60	90
178, 179	0.999-0.999	0.999-0.999	0.999-0.999	300	450	680
180	1	1	1	48	64	96

Table D.8: Flat-bottom roll mesh seeding summary

Edge	Ratio			Intervals		
	Coarse	Medium	Fine	Coarse	Medium	Fine
74, 75, 76, 77	1	1	1	25	36	54
99, 100	10.52-1.052	1.04-1.04	1.04-1.04	60	60	90
186	1	1	1	40	60	90
184, 185	1	1	1	99	150	225
181	1	1	1	84	120	180
182, 183	1	1	1	5	8	8

Table D.9: Round-bottom roll mesh seeding summary

Edge	Ratio			Intervals		
	Coarse	Medium	Fine	Coarse	Medium	Fine
74, 75, 76, 77	1	1	1	25	36	54
99, 100	10.52-1.052	1.04-1.04	1.04-1.04	60	60	90
181, 182	1	1	1	21	30	45
180	1	1	1	99	150	225
183	1	1	1	27	42	60

Appendix E

FLUENT (2009) Dynamic Mesh Definitions

E.1 Dynamic Mesh Definitions

Remeshing and smoothing methods were employed for these dynamic mesh regions. Remeshing is usually used in conjunction with spring-based smoothing, explained below (FLUENT, 2009*a*).

An edge that connects two mesh nodes may be regarded as an interconnecting spring (figure E.1). It may be assumed that the initial position of these nodes presents a spring-node system in equilibrium. Displacement of the nodes will exert a force on the spring connections. Consider Hook's Law:

$$\vec{F}_i = \sum_j^{n_i} k_{ij}(\delta\vec{x}_j - \delta\vec{x}_i) \quad (\text{E.1.1})$$

Where $\delta\vec{x}_j$ and $\delta\vec{x}_i$ are the displacements of node i and a node next to it j . The spring stiffness is a function of the distance between two nodes. This stiffness is described by:

$$k_{ij} = \frac{1}{\sqrt{|\vec{x}_i - \vec{x}_j|}} \quad (\text{E.1.2})$$

At equilibrium the resultant force acting on a node must be zero. To determine the new position of the nodes after the boundary node position has been updated an iterative equation is implemented:

$$\delta\vec{x}_i^{m+1} = \frac{\sum_j^{n_i} k_{ij}\delta\vec{x}_j^m}{\sum_j^{n_i} k_{ij}} \quad (\text{E.1.3})$$

Finally the new position of node i can be updated:

$$\vec{x}_i^{m+1} = \vec{x}_i^m + \delta\vec{x}_i^{m,converged} \quad (\text{E.1.4})$$

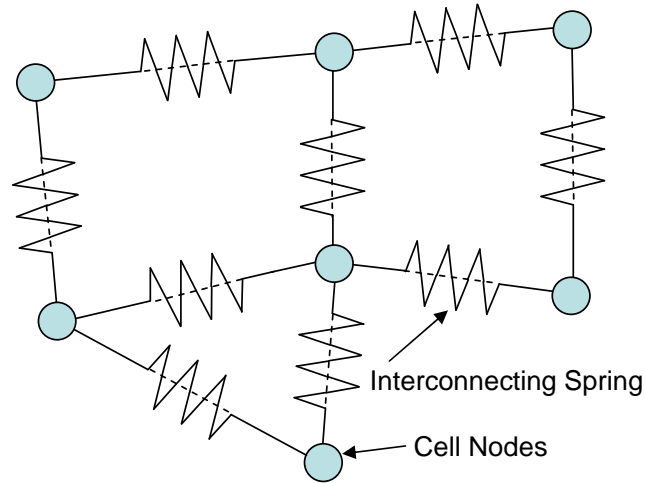


Figure E.1: Schematic of the concept of interconnecting springs between cell nodes

If the spring constant factor is 0 the moving boundary zone has a large effect on the motion of the interior nodes. This setting must be used for rigid wall boundaries. Setting a spring constant factor of 1 allows equation (E.1.3) to be solved as normal. The larger the spring constant factor the more cells are deformed which typically gives a smoother transition. A factor of 1 was set for this case.

Boundary node relaxation is used to manipulate equation (E.1.4). Consider:

$$\vec{x}_i^{n+1} = \vec{x}_i^n + \beta \delta \vec{x}_{spring}^{m,converged} \quad (\text{E.1.5})$$

A boundary node relaxation (β) can be set. A value of 0 restricts any deformation of the boundary nodes and 1 results in no node-relaxation. Because the dynamic mesh region surrounds an inner boundary, no node relaxation is required. A value of 0 is applicable for this case.

Equation (E.1.4) is solved iteratively and the convergence tolerance and number of iterations can be used as controls. The solution is converged for a time step if the value of that time step is less than the tolerance value. The convergence value is calculated with:

$$\left(\frac{\delta \vec{x}_{rms}^m}{\delta \vec{x}_{rms}^1} \right) \quad (\text{E.1.6})$$

$\delta \vec{x}_{rms}^m$ is the interior deforming nodes root-mean squared (RMS) displacement and $\delta \vec{x}_{rms}^1$ is the RMS at the first iteration.:

$$\delta \vec{x}_{rms}^m = \sqrt{\frac{\delta \vec{x}_1^m + \delta \vec{x}_2^m + \delta \vec{x}_3^m + \dots}{\# \text{ of nodes}}} \quad (\text{E.1.7})$$

A tolerance factor of 0.001 provides appropriate accuracy and keeps the number of iterations satisfactorily low. The number of iterations is limited to 20. It is

expected that this limit will not be reached. If more iterations are required, the process becomes too computationally intensive.

Triangular inner cells were required for spring-based smoothing since non-triangular cells become highly skewed.

If boundary displacements are large compared to the local cell size, a remeshing function in FLUENT (2009) may be employed. This method prevents the degeneration of the computational grid. If a certain skewness or size limit is reached as the cells deform, the local region is remeshed. Several remeshing methods are available in FLUENT (2009). Local cell remeshing is employed for this two-dimensional grid. The minimum length scale was set according to the minimum cell size in the computational domain. It was taken into consideration that the cell size near the hull wall is two orders of magnitude smaller than the larger cells in the outer region of the computational domain. Even though the remeshing zone is relatively far from the hull, the lower length scale (length of a cell face) limit chosen is 0.0004 m and the upper limit 0.002 m. The cell skewness limit was set to 0.6. The above mentioned settings were sufficient to maintain mesh integrity.

Sliding meshes were investigated to determine the possibility of implementing this method to reduce computational time and to maintain mesh integrity. The method may not be applicable for the heave (which was simulated as a symmetrical problem) nor for the sway cases and was not used. Sliding meshes are useful in rolling about a fixed axis. Sliding also has the advantage of avoiding remeshing.

References

- Anderson, J.D. (Jr.) (1995). *Computational Fluid Dynamics, The Basics with Application*. McGraw-Hill.
- Bangun, E., Wang, C. and Utsunomiya, T. (2010 April). Hydrodynamic forces on a rolling barge with bilge keels. *Applied Ocean Research*, vol. 32, no. 2, pp. 219–232.
- Benek, J.A., Buning, P.G. and Steger, J.L. (1985 July). A 3-D Chimera grid embedding technique. In: *The Proceedings of AIAA 7th Computational Fluid Dynamics Conference, Cincinnati, OH*, 85-1523.
- Bishop, R., Price, W. and Temarel, P. (1980). Hydrodynamic coefficients of some swaying and rolling cylinders of arbitrary shape. *International Shipbuilding Progress*, vol. 27, pp. 54–65.
- Blagoveshchensky, S. (1962). *Theory of Ship Motions*, vol. 1. Dover Publications.
- Brian, A. (2003). *Ship Hydrostatics and Stability*. Butterworth Heinemann.
- Chadwick, A., Morfett, J. and M., B. (2004). *Hydraulics in Civil and Environmental Engineering, Fourth Edition*. Spon.
- Chen, H. and Liu, T. (2002). Time-domain simulations of large-amplitude ship roll motions by Chimera RANS method. *International Journal of Offshore and Polar Engineering*, vol. 12, no. 3, pp. 206–212.
- Chen, H. and Patel, V. (1988). Near-wall turbulence models for complex flows including separation. *AIAA Journal*, vol. 26, no. 6, pp. 641–648.
- Chen, H.C. and Chen, M. (1998). Chimera RANS simulation of a berthing DDG-51 ship in transitional and rotational motions. *International Journal of Offshore and Polar Engineering*, vol. 8, no. 3, pp. 182–191.
- Chen, H.C., Liu, T., Huang, E.T. and Davis, D.A. (2000). Chimera RANS simulation of of ship and fender coupling for berthing operations. *International Journal of Offshore and Polar Engineering*, vol. 10, no. 2, pp. 112–122.
- Falkner, V.M. and Skan, S.W. (1930). *Aeronautical Research Council Reports and Memoranda*, vol. 1314.
- Ferziger, J.H. and Peric', M. (2002). *Computational Methods for Fluid Dynamics*. 3rd edn. Springer, Berlin.

- FLUENT (2006). Fluent user services centre, tutorial: Solving a 2d box falling into water.
- FLUENT (2007). Fluent user services centre, advanced fluent training, multiphase. Available at: www.fluentusers.com
- FLUENT (2009a). *Ansys Fluent 12.0 Theory Guide*. Ansys Inc.
- FLUENT (2009b). *Ansys Fluent 12.0 User's Guide*. Ansys Inc.
- FLUENT (2009). *Fluent, Revision: 12.0.16 for the Ansys Release Version 12.0.1*. Ansys, Inc.
- GAMBIT (2004). *Gambit 2.4.6*, Fluent Inc.
- Gupta, R., Fletcher, D. and Haynes, B. (2009). On the CFD modelling of Taylor flow in microchannels. *Chemical Engineering Science*, vol. 64, pp. 2941–2950.
- Himento, Y. (1981). Prediction of ship roll damping-state of the art. Tech. Rep., The University of Michigan, Collage of Engineering.
- Ibrahim, R. and Grace, I. (2009 November). Modelling of ship roll dynamics and its coupling with heave and pitch. *Mathematical Problems in Engineering*, vol. 2010, no. 1, pp. 1–32.
- Ikeda, Y. (2004). Prediction methods of roll damping of ships and their application to determine optimum stabilization devices. *Journal of Marine Technology*, vol. 41, no. 2, pp. 89–93.
- Issa, R. (1986). Solution of the implicitly discretized fluid flow equations by operator-splitting. *Journal of Computational Physics*, vol. 62, pp. 40–65.
- Jong, B.D. (1967). Berekening van de hydrodynamische coëfficiënten van oscillerende cilindres. Tech. Rep., Ship Building Laboratory, Technical University Delft.
- Kim, K.-H. (2003). Simulations of surface ship dynamics using unsteady RANS codes. In: *The Proceedings of RTO AVT Symposium "Reduction of Military Vehicle Acquisition Time and Cost through Advanced Modelling and Virtual Simulation"*, 35, pp. 1–13.
- Kinnas, S., Yu, Y.-H. and Vinayan, V. (2006 May 28-June 2). Prediction of flows around FPSO hull sections in roll using an unsteady Navier-Stokes solver. In: *The Proceedings of the Sixteenth International Offshore and Polar Engineering Conference*, pp. 384–393. The International Offshore Society of Offshore and Polar Engineers.
- Korpus, R. (2004). Reynolds-Averaged Navier-Stokes in an integrated design environment. In: *The Proceedings of the 1st International Symposium on Design and Production of Motor and Sail Yachts*, pp. 1–15.

- Korpus, R. and Falzarano, J. (1997). Prediction of viscous ship roll damping by unsteady navier-stokes techniques. *Journal of Offshore Mechanics and Arctic Engineering*, vol. 119, pp. 108–113.
- Korvin-Kroukovsky, B. (1961). *Theory of Seakeeping*. The Society of Naval Architects and Marine Engineers.
- Lauder, B. and Spalding, D. (1974). The numerical computation of turbulent flows. *Computer Methods in Applied Mechanics and Engineering*, vol. 3, pp. 269–289.
- Lauder, B.E., Reece, G.J. and Rodi, W. (1975). Progress in the development of a Reynolds-stress turbulence closure. *Journal of Fluid Mechanics*, vol. 68, pp. 537–566.
- Lewis, F. (1929). The inertia of the water surrounding a vibrating ship. In: *The Transactions of SNAME*, vol. 27, pp. 1–20.
- Lin, R.-Q. and Kuang, W. (2008). Modelling nonlinear roll damping with a self-consistent, strongly nonlinear ship motion model. *Journal of Marine Science and Technology*, vol. 13, pp. 127–137.
- MATLAB (2005). *MATLAB, Version 7.1.0.246(R14) Service Pack 3, The MathWorks, Inc.*
- Menter, F. (1994). Two-equation eddy-viscosity turbulence models for engineering applications. *AIAA Journal*, vol. 32, no. 8, pp. 1598–1605.
- Menter, F., Langtry, R., Likki, S., Suzen, Y., Huang, P. and Volker, S. (2006). A correlation based transition model using local variables part 1 - model formulation. *Journal of Turbomachinery*, vol. 128, pp. 413–422.
- Menter, F.R. (1992a). Performance of popular turbulence models for attached and separated adverse pressure gradient flow. *AIAA Journal*, vol. 30, pp. 2066–2072.
- Mitra, S.K. (2006). *Digital Signal Preocessing, A Computer-Bassed Approach*. 3rd edn. McGraw-Hill.
- Mulk, M.T.U. and Falzarano, J. (1994). Complete six-degrees-of-freedom nonlinear ship rolling motion. *Journal of Offshore Mechanics and Arctic Engineering*, vol. 116, pp. 191–201.
- Muzaferija, S. and Peric, M. (1998). Computation of free-surface flows using interface tracking and interface capturing methods. In: Mahrenholtz, O. and Markiewicz, M. (eds.), *Nonlinear water wave interaction*, chap. 3, pp. 59–110. Computational Mechanics Pulications, Southampton.
- Paterson, E., Wilson, R. and Stern, F. (2003). General purpose parallel unsteady RANS ship hydrodynamics code: CFDSHIP-IOWA. Tech. Rep., Hydrosience and engineering report no. 432.

- Pesman, E., Bayraktar, D. and Taylan, M. (2007). Influence of damping on the roll motions of ships. In: *The 2nd International Conference on Marine Research and Transportation*, pp. 127–133.
- Quérad, A., Yermarel, P.T. and Turnock, S. (2009). The hydrodynamics of ship-like sections in heave, sway, and roll motions predicted using an unsteady Reynolds-averaged Navier-Stokes method. *Journal of Engineering for the Maritime Environment*, vol. 223, no. 2, pp. 227–238.
- Rodi, W. (1980). Turbulence models and their application in hydraulics - a state of the art review. Tech. Rep., IAHR, Delft, The Netherlands.
- Sarkar, T. and Vassalos, D. (2000). A RANS-based technique for simulation of the flow near a rolling cylinder at the free-surface. *Journal of Marine Science and Technology*, vol. 5, pp. 66–77.
- Spalart, P. and Allmaras, S. (1992). On-equation turbulence model for aerodynamic flows. *AIAA Journal*, p. 92.
- Thiart, G. (2010). *Verbal discussion an meetings with Prof. G. D. Thiart*.
- Ursell, F. (1949). On the heaving motion of a circular cylinder in the surface of a fluid. *Quarterly Journal of Mechanics and Applied Mathematics*, vol. 2, pp. 218–231.
- Versteeg, H. and Malalasekera, M. (2007). *An Introduction to Computational Fluid Dynamics, the Finite Volume Method*. 2nd edn. Prentice Hall.
- Vugts, J. (1968). The hydrodynamic coefficients for swaying, heaving and rolling cylinders in a free surface. *International Shipbuilding Progress*, vol. 15, pp. 251–276.
- Walters, D. and Cokljat, D. (2008). A three-equation eddy-viscosity model for Reynolds-averaged Navier-Stokes simulations of transitional flows. *Journal of Fluids Engineering*, vol. 130, pp. 1–14.
- Wilcox, D.C. (1988). Reassessment of the scale-determining equation for advanced turbulence models. *AIAA Journal*, vol. 26, no. 11, pp. 1299–1310.
- Wilson, R., Carrica, P. and Stern, F. (2006). Unsteady RANS method for ship motions with application to roll for a surface combatant. *Journal of Computers and Fluids*, vol. 35, pp. 501–524.
- Yakhot, V., Orszag, S.A., Thangam, S., Gotski, T.B. and Speziale, C.G. (1992). Development of turbulence models for shear flows by a double expansion technique. *Physics of Fluids*, vol. 4, no. 7, pp. 1510–1520.
- Yeung, R. and Ananthakrishnan, P. (1992). Oscillation of a floating body in a viscous fluid. *Journal of Engineering Mathematics*, vol. 26, pp. 211–230.
- Yeung, R., Liao, S.-W. and Roddier, D. (1998). Hydrodynamic coefficients of rolling rectangular cylinders. *International Journal of Offshore and Polar Engineering*, vol. 8, no. 4, pp. 241–250.

REFERENCES

132

- Yeung, R. and Vaidhyanathan, M. (1994). Highly separated flows near a free surface.
In: *The Proceedings of the Conference on Hydrodynamics*, pp. 118–129. Wuxi, China.